Delft University of Technology

Norwegian University of Science and Technology

Delft University of Technology

Norwegian University of Science and Technology

OE54030 Master Thesis

TMR5950 Wind Turbine Energy - Offshore Engineering, Master Thesis

---

Parametric Instability of the Pitch Motion of the STC Concept

---

Author:

Sevyllen Kistnen Appiah

Supervisors:

Prof. Andrei Metrikine

Prof. Zhen Gao

Dr. Zhiyu Jiang

July 17, 2017

Abstract

Resonant motions of a combined wind and wave concept (STC) in waves may induce significant loads in the structural components (such as wind turbine blades, nacelle or the interface between the spar and the torus). One type of resonant motions is related to the so-called Mathieu instability. For the STC under the survival mode where the torus is locked to the spar at the mean water level (MWL mode), the large heave motion in severe waves induces a significant change in the buoyancy center and therefore leads to a periodic change in the restoring term for the pitch motion. When the wave period reaches the half of the natural period, the Mathieu instability (a dynamic instability in pitch for this case) occurs and leads to significant pitch motions.

The purpose of this study is to numerically predict such unstable motions for regular and irregular wave conditions and to compare the results with the experimental observations. First, a literature study on Mathieu instability is carried out to understand the mechanism behind this phenomenon. Then the results of the STC concept from the experiments carried out by Dr. Ling Wan are investigated in order to study the developments of the Mathieu unstable pitch motions and the corresponding wave conditions in which they occur. Finally, a numerical model of Mathieu instability for analysis of the STC pitch motions is established to get insight into the phenomenon.

The numerical model is compared with the experimental results of Dr. Ling Wan. A sensitivity study using the numerical model is then carried out to investigate the conditions where the Mathieu instability may occur.

Acknowledgements

I would like to give my sincere thanks to my main supervisor, Professor Zhen Gao, who has been invaluable during my thesis work. He contributed great time and efforts and helped shape my work all along the way. His deep insights, knowledge and kindness helped me progress and always pointed me in the right directions. I would also like to thank Dr. Zhiyu Jiang, with whom I had many productive discussions over my work. He was always available and provided great insights in all areas of my work.

I appreciate the assistance of Dr.Yuna Zhao who helped me acquire a better understanding of how the software works. It was a great pleasure to have discussions with her. I would like to thank my TU Delft supervisor, Professor Andrei Metrikine, who has been very straightforward despite being busy.I would also like to thank Dr. Ling Wan, whose work this thesis is largely based on. He has been very accessible and helpful in examining the data.

Finally, I would like to express my gratitude to all those with whom I shared great memories of my time in Norway. The good times with you made my stay in Norway very enjoyable.

Contents

Chapter 1

Introduction

1.1 Background

The world human population first reached one billion in 1804, two billion in 1927, and three billion in 1960 (UN, 1999). After the 1960s, the world population has been increasing by one billion approximately every 13 years and the United Nations estimate that it will increase to 11.2 billion by 2100. Such a drastic increase in population leads to a depletion in natural resources and a degradation of the environment. The burning of fossil fuels to accommodate the growing needs of energy releases billions of tonnes of carbon dioxide in the atmosphere which results in global climate change.

Severe environmental phenomena such as global warming, the ongoing extinction of plant and animal species, ocean acidification, and increased storm activity have motivated people to invest into renewable and non-polluting sources of energy. There are many types of renewable energy such as solar energy, wind energy, wave energy, hydropower, geothermal energy and bio energy. This report centers around wind power and wave energy.

1.2 Wind Energy

Wind energy is a free and renewable resource, consumes virtually no water, and emits no air pollutants and greenhouse gases. Most modern wind turbines consist of usually three rotating blades connected to a horizontal shaft, hence called horizontal-axis wind turbines (HAWTs). Despite some environmental concerns such as the noise produced

and birds killed by the rotor blades, and visual aesthetics, the advantages of wind energy heavily outweighs its downsides.

The construction of wind farms in offshore areas is favoured due to stronger and more constant wind speeds, and much weaker Not In My Back Yard (NIMBY) opposition. Despite the technological advances in wind energy, its levelized cost still remains relatively high (www.eia.gov, 2016). Currently, there is 142 GW of installed wind power capacity in the EU, which includes 11 GW offshore (EWEA, 2015). The trends show an increase in wind power installations while conventional power sources such as oil and coal continue to decommission more capacity than they install.

Most wind turbines in offshore environments are installed in regions where the water depth is less than 50 m (EWEA, 2013) and these turbines have fixed foundations. For locations with water depths greater than 50 m, floating wind turbine concepts are more feasible and cost-effective. Fig. 1.1 shows some commonly used substructures and the water depths at which they are generally installed.

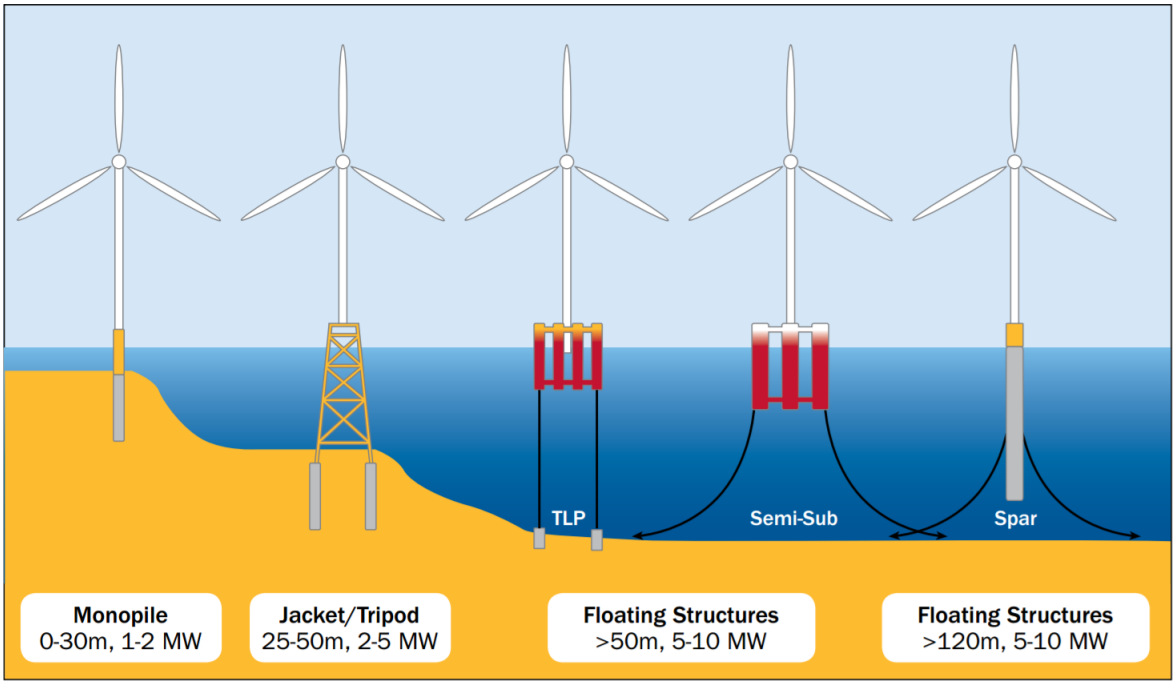

Figure 1.1: *Offshore wind foundations (EWEA, 2013).*

The three types of floating foundations symbolizes different approaches to achieve static stability of the floating body. The tension-leg platform (TLP) is stabilized by mooring lines, the semi-submersible is stabilized by buoyancy and the spar is stabilized

by ballast (Butterfield et al., 2007). It should be noted that these denote the principles that the floaters rely on and all the floaters achieve stability using hybrid principles among the three.

Spars exhibit good performance in heave motion due to the deep draft and small water plane area but show poor performance in pitch and roll motions (Wan, 2016). TLPs have good performance due to the high restoring stiffness in heave, pitch and roll but installing the mooring lines is expensive. The convenience of installation and commissioning favours semi-submersibles but at the expense of higher wave forces due to the large water plane area. Despite the difference in dimensions, characteristics and performance of the floating wind turbines depending on the different concepts, the wind turbine performances are similar.

1.3 Wave Energy

Water has a much higher density than air, which results in wave energy containing significantly more kinetic energy than wind energy. This enables smaller, quieter and less visually obstructive devices to generate the same amount of power at a fraction of the space. Unlike wind and solar energies, wave energy can be constantly extracted. Wind velocity is highly reduced in the morning and at night and solar energy is only available during the day. Hence, the production of wave power is more consistent and results in higher overall capacity factors.

(Cruz, 2008) estimates that the total potential wave power worldwide is 2 TW, in the same order of magnitude as the current world's electricity consumption. Wave energy is of high density and is proportional to the wave period and is proportional to the square of the wave amplitude. A wave energy converter is a device that harnesses energy from the sea waves by itself generating waves, which negatively interferes with the sea waves (Budal and Falnes, 1975).

Many concepts for offshore wave energy converters have been built or proposed so far. They can be classified as oscillating water columns, oscillating bodies, and overtopping devices on the basis of how they absorb wave energy (Falcao, 2010). Oscillating bodies absorb wave energy by the oscillation of the structure relative to a point through a power take off (PTO) system, a device that converts wave energy into mechanical or electrical energy. Oscillating water columns absorbs wave energy by driving air through

a turbine at the top of the structure. Overtopping devices absorb wave energy by capturing and storing water in a reservoir and releasing the water through hydraulic turbines. Fig. 1.2 provides some illustrations of different wave energy concepts.

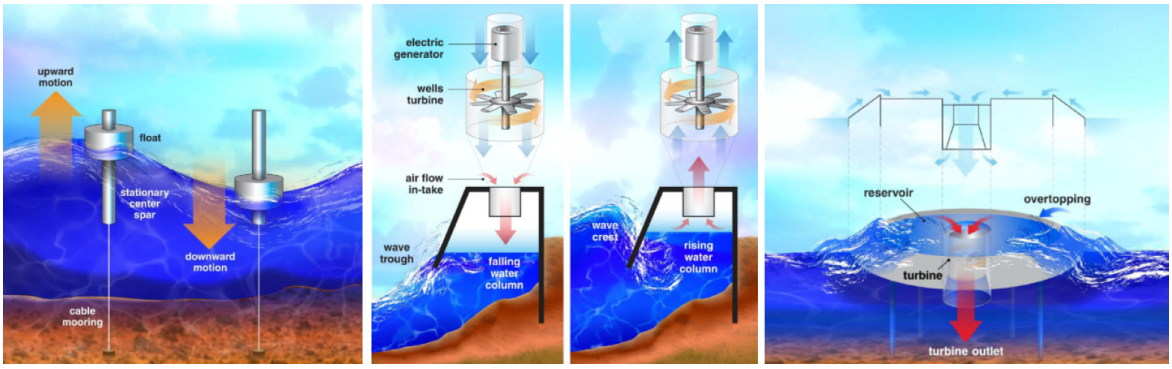

Figure 1.2: *Different principles of harnessing wave energy. Left: point absorber. Centre: oscillating water column. Right: overtopping device (Li and Yu, 2012).*

1.4 Combined Wind and Wave Energy Converter Concepts

To make the most of the marine environment, concepts that capture both wind and wave energy have been proposed. (ISSC, 2015) suggests that offshore platforms that incorporate multiple functions within the same framework can present considerable economic and environmental benefits. Therefore combining wind and wave energy converters into one device, especially in a wind farm configuration can offer many advantages.

One of the wind and wave energy converters is the spar-torus combination (STC) concept, which integrates a spar floating wind turbine and a coaxial heaving body wave energy converter (Wan, 2016). This combined wind and wave energy converter concept was developed in the EU FP7 MARINA Platform Project. Numerical analysis and lab tests were performed to study the power performance in operational conditions and the survivability in extreme conditions. The wind turbine is the NREL 5 MW (Jonkman et al., 2009) and the torus-shaped wave energy converter has been motivated by the WaveBob concept, developed between 1999 and 2013 (Mouwen, 2008). The wave energy converter can oscillate along the vertical axis of the spar to absorb wave energy through

a hydraulic system.

1.5 Cost of Energy

The cost of energy is a driving factor that governs which type of energy technology will be chosen. The levelized cost of electricity (LCOE) is a measure of comparison between different methods of electricity generation on a comparable basis, that is, on a fair basis where aspects such as the risks and carbon price volatility are included. The LCOE can also be viewed as the minimum cost at which electricity must be sold so as to break-even over the design lifetime of the project. One of the prominent levelized cost studies, conducted by Lazard (see Fig. 1.3), found that onshore wind has the lowest average LCOE. Some renewable energy generation technologies have the potential have the potential to be cost-competitive with conventional technologies under some scenarios. Green energy technologies may incur higher capital costs but have no fuel costs once operational and have lower O&M costs than conventional technologies.

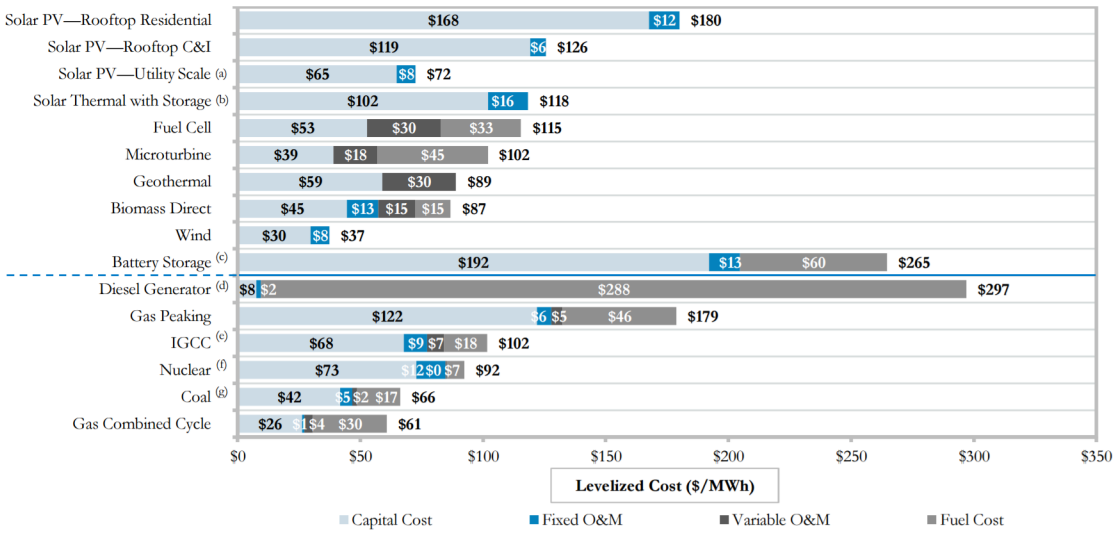

Figure 1.3: *Levelized cost of energy of various technologies (LAZARD, 2014).*

1.5.1 Wind Energy

Wind energy, both onshore and offshore, is becoming more preferable not only as a renewable energy technology but also as an investment which does not suffer from

unpredictable and volatile costs (Arapogianni, 2011). The total investments for the construction an refinancing of offshore wind farms and transmission assets hit a record level of €18 billion in 2015 and there are several transactions that are already under appraisal or that are expected to undergo final investment decision in 2016 (EWEA, 2015).

In 2015, wind energy overtook hydropower as the third largest source of power generation in the EU with a total power capacity share of 15.6%. Moreover, wind energy accounts for one third of all the new power installations in the EU since 2000. The trend is that conventional power sources such as fuel oil and coal keep on decommissioning more capacity than they install, as shown in Fig. 1.4.

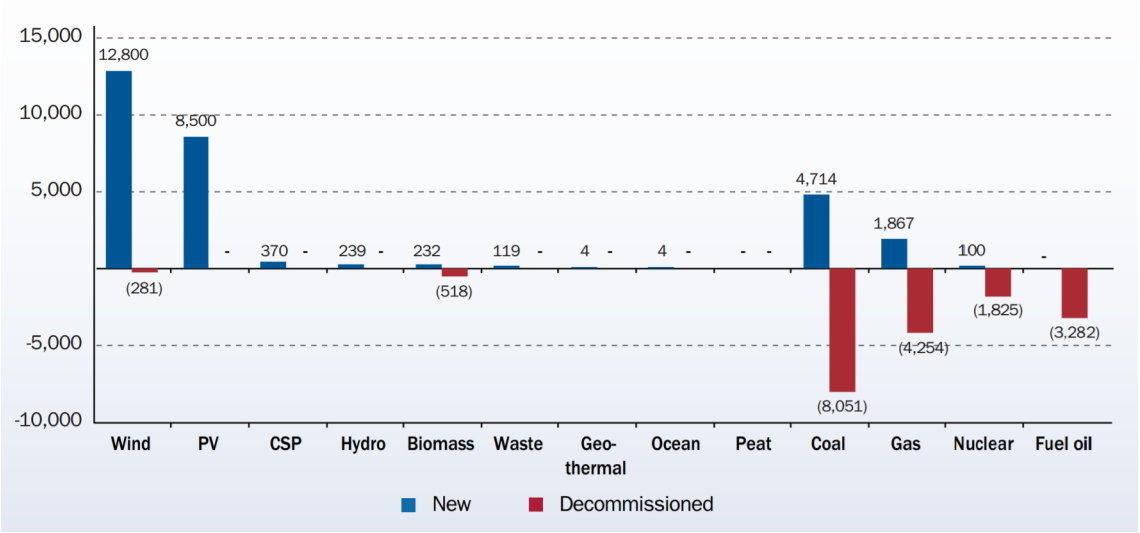

Figure 1.4: *New installed and and decommissioned power capacity in the EU (MW) in 2015 (EWEA, 2016).*

1.5.2 Wave Energy

Europe remains the leading market for wave technologies, even though other countries and regions are rapidly progressing. Although the market is still monopolized by start-up companies, large engineering firms and utilities, such as Lockheed Martin, Alstom and Mitsubishi Heavy Industries, have also come into the market IRENA (2014).

Wave energy is not currently competitive with other renewable energy sources when viewed from an economic perspective. The levelized cost for wave energy farms (10 MW) are in the range 330-630 €/MWh (Europe, 2013), which are significantly higher

than other forms of renewable energy technologies. However, wave energy is at an early stage of technological development and the potential for wave energy is considerably higher than tidal resources across the same geographic area and is less dependent on site (IRENA, 2014). Fig. 1.5 shows the LCOE predictions for 10 MW arrays, after 10 MW has already been installed. Commercial arrays will not be marketable without considerable cost reductions through innovation, increased performance, experience and reliability of future prototypes.

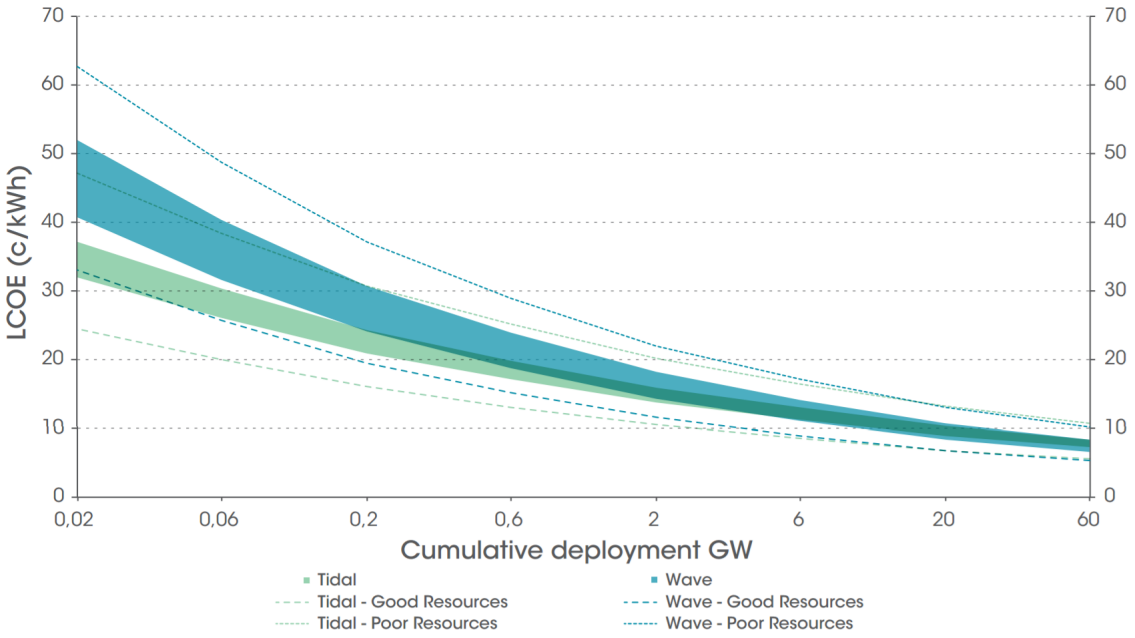

Figure 1.5: *LCOE predictions for 10 MW arrays (Europe, 2013).*

1.5.3 Combined Wind and Wave Energy

The development of technology and innovation can best be delivered when there is a strong collaboration between industry, research institutions, Member State governments and European Commission organizations (Europe, 2014). This type of coordination will help to ensure that the Research and Development programmes can be customized to the needs of the industry.

Recent research by JRC, a consortium partner of SI Ocean, found that offshore wind and wave and tidal projects could have component and project synergies of up to 40% (Europe, 2014). This represents another area for future cost reduction and shows

the benefits of examining opportunities for shared Research and Development into key components and processes with potential for application in both sectors (see Fig. 1.6).

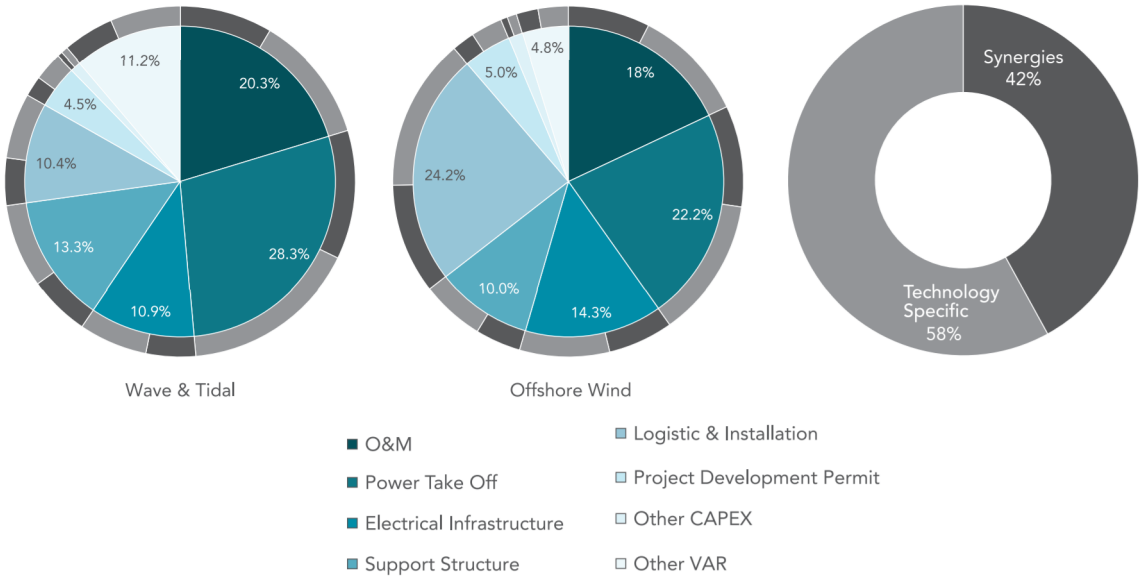

Figure 1.6: *Synergies between wave and tidal energy and offshore wind (Europe, 2014).*

Combined wind and wave energy concepts are an option that have been considered recently. These combined energy concepts enable the efficient use of offshore resources which can result is potential cost reductions due to synergies such as increased energy yield, shared logistics and maintenance activities or common substructure (Castro-Santos et al., 2016).

Research conducted by (Castro-Santos et al., 2016) found that wave energy has a relatively small contribution to the total electrical power output of most combine wind and WEC concepts. These concepts have more energy produced than traditional floating wind energy devices, which would decrease or benefit their LCOE. However, the LCOE of these concepts are much higher than the floating offshore wind turbines. The increased in quantity of steel to combine wave and offshore wind do not compensate for the additional energy output and hence values of manufacturing, installation, exploitation and decommissioning are higher than traditional offshore wind (Castro-Santos et al., 2016).

Chapter 2

Mathieu Instability

2.1 Introduction

Mathieu instability occurs when the time period of the wave excitation is equal to half of the natural period of the pitch motion and thus, pitch resonance develops. This occurs because the heave motion influences the restoring term of the pitch motion which then varies in time. In the occurrence of Mathieu instability, the period of the pitch motion progressively changes from the period of the wave to twice the wave period. The pitch amplitude also increases until it reaches a steady-state value (Wan et al., 2015).

2.2 Mathieu Instability in Heave

There are different types of Mathieu instability (Wan et al., 2014). The simplest case can be described by a non-linear restoring term. For instance, when a spar experiences an abrupt change in the water plane area, there will be a change in the restoring force of the heave motion, that is, the heave restoring force is dependent on time. The frequency of the heave motion, as well as he heave restoring due to the sudden change in the water plane area, will correspond to the wave frequency. The undamped equation of motion can be expressed as:

$$[M + A_{33}]\,\ddot{\eta}_3 + [k_3 + \Delta k_3 f(t)]\,\eta_3 = 0 \tag{2.1}$$

where

M is the mass of the structure.

A_{33} is the heave added mass.

η_3 is the heave motion.

$\ddot{\eta}_3$ is the heave acceleration.

k_3 is the heave restoring.

$\Delta k_3 f(t)$ is the time dependent heave restoring coefficient.

Eq. 2.1 is in the form of the Mathieu equation but is not exactly the same because the change in the restoring force, $f(t)$, is a periodic step function instead of a harmonic function. Nevertheless, the behaviour is still very similar (Haslum and Faltinsen, 1999). When the change in the restoring force, $f(t)$, corresponds with $\frac{1}{2}T_N, T_N, \frac{3}{2}T_N, 2T_N, ...$ where T_N is the natural period of the structure, the equation of motion may develop some instability, depending on the degree of damping.

In experiments carried out by (Haslum and Faltinsen, 1999), two methods were used to investigate the effects of Mathieu instability of a spar platform. The first case was the linear frequency domain where the hydrodynamic excitation forces are computed at the mean position, which conforms to linear theory. The restoring coefficient, k_3, is computed using the waterplane area at the mean position of the structure. The second case was the time domain analysis where the hydrodynamic excitation forces are calculated at the displaced position and the effects that the changing waterplane area has on the amplitude is also considered. The amplitude of the incoming waves are taken as 10 metres to calculate the response in heave motion for the second case. Finally, a 2% linear critical heave damping is used in both cases.

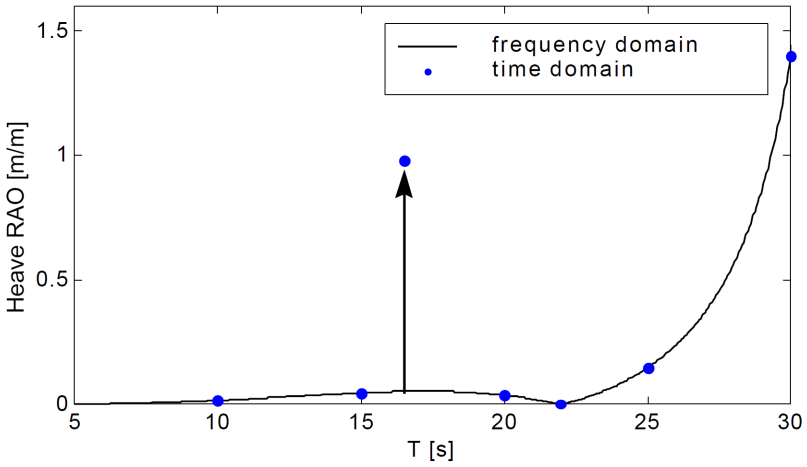

Figure 2.1: *Comparison between the frequency and time domain analyses of the Heave RAO (Haslum and Faltinsen, 1999).*

The steady state heave amplitude is divided by the wave amplitude and is shown together with the RAO, see Fig. 2.1 and the two methods can then be compared. Both methods agree with each other except for waves with a period of 16.5 seconds. At this wave period, the heave response amplitude is large with an RAO of 0.98 whereas linear theory predicts an RAO of 0.05. In other words, due to Mathieu instability, the heave motion is about 20 times larger that that wave period. The Mathieu instability would be even more pronounced if a lower damping in heave had been used.

2.3 Mathieu Instability in Heave/Pitch

Another type of Mathieu instability is coupled instability in the heave/pitch motions. This occurs because the heave influences the pitch restoring term. Neglecting the damping term, the uncoupled equation of motion for pitch can be expressed as:

$$[I_{55} + A_{55}]\,\ddot{\eta}_5 + \rho g \nabla \overline{GM} \eta_5 = 0 \tag{2.2}$$

where

I_{55} is the moment of inertia around the pitching axis.

A_{55} is the pitch added moment.

ρ is the water density.

g is the gravitational acceleration.

∇ is the buoyancy volume.

$\ddot{\eta}_5$ is the pitch acceleration and η_5 is the pitch motion.

It should be noted that some simplifications have been made to exemplify the situation more easily. For a more accurate numerical analysis, damping effects, wave excitation forces and coupling with other degrees of freedom should be considered.

The pitch restoring term is a function of the submerged volume and the metacentric height, $\overline{GM}$. Hydrostatic theory defines the initial metacentric height at neutral draft as (Haslum and Faltinsen, 1999):

$$\overline{GM}_0 = \overline{KB} + \overline{BM} - \overline{KG} \tag{2.3}$$

where

$\overline{KB}$ is the distance from the keel to the buoyancy centre.

$\overline{BM}$ is the distance from the buoyancy centre to the metacentre.

$\overline{KG}$ is the distance from the keel to the centre of gravity.

Unlike linear theory, the pitch restoring term is evaluated at the displaced heave position instead of using the mean position. Thus, both the submerged volume and the metacentric height become a function of the heave motion, as shown in Fig. 2.2.

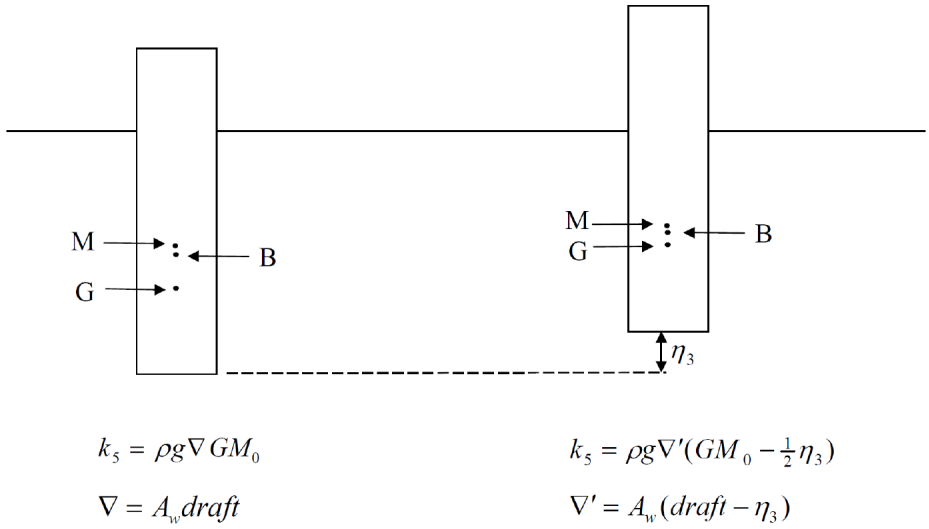

Figure 2.2: *Pitch restoring force for mean position (left) and for displaced position (right) (Haslum and Faltinsen, 1999).*

The heave motion can be expressed in the following form:

$$\eta_3(t) = \eta_{3m} \cos(\omega t) \tag{2.4}$$

where

ω is the frequency of the heave motion.

η_{3m} is the heave amplitude.

Then, Eq. 2.2 can be expressed as the classical Mathieu equation as follows:

$$[I_{55} + A_{55}]\,\ddot{\eta}_5 + \rho g \nabla \left(\overline{GM}_m - \frac{1}{2}\eta_{3m} \cos(\omega t)\right) \eta_5 = 0 \tag{2.5}$$

with

$$\overline{GM} = \overline{GM}_m - \frac{1}{2}\left(\eta_3(t) - \zeta(x_c, y_c, t)\right) \tag{2.6}$$

$$\nabla = \nabla_m - A_w\left(\eta_3(t) - \zeta(x_c, y_c, t)\right) \tag{2.7}$$

where

$\overline{GM}_m$ is the pitch metacentric height corresponding to the restoring at still water.

∇_m is the displaced volume of still water.

A_w is the water plane area.

$\zeta\left(x_c, y_c, t\right)$ is the wave elevation at the flotation center.

If the damping is taken into account, the stability diagram can be generated, which shows the unstable region. When damping is included in the system, the unstable region is decreased. Given the pitch natural period to be ω_5, it can be found from the stability diagram that when the ratio ω_5/ω is about 0.5, 1, 1.5, 2 and so on, instability could occur, as shown in the stability diagram in Fig. 2.3.

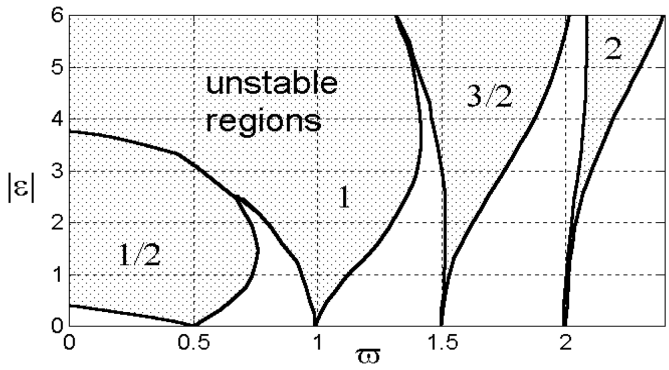

Figure 2.3: *Stability diagram for Mathieu's equation (Haslum and Faltinsen, 1999).*

Physically, the linear damping assumption does not offer a good representation when large response amplitudes occur (Haslum and Faltinsen, 1999). Viscous drag effects dominate the damping, which results in the damping being quadratic. Therefore, a damping model can be enhanced by using a linearization technique, that is, the damping is dependent on the motion response. Alternatively, the nonlinear drag forces can be incorporated without any alteration.

One of the ways to reduce the wave frequency heave resonant response is to increase the damping of the system. This can be achieved by using helical strakes over the length of the spar or by a disc at the keel. Increasing the length of the strakes results in higher magnitudes of environmental forces which are exerted onto the mooring system. The advantage of the disc at the keel is that the viscous excitation from waves is limited due to the exponential decay with depth. (Haslum and Faltinsen, 1999) also found that

the most effective way of decreasing the unstable heave/pitch motion is by adding more damping in pitch.

(Koo et al., 2004) found that the heave damping from mooring lines is important for the spar platform. The heave damping from Coulomb friction is rather small but it cannot be neglected. Mooring lines play an important role in the Mathieu instability analysis of a spar platform by increasing damping/shifting the pitch natural period. Thus, if mooring lines are not properly modeled in the simulation and experiment, incorrect results, such as the possibility of Mathieu instability being overestimated, may be obtained under certain conditions.

It should be noted that in this section, it is assumed that damping effects, wave excitation forces and couplings between other modes of motion are not considered. If these are taken into account, the stability diagram would be influenced. The curves that separated the various unstable regions in the stability diagram would be less distinct but unstable solutions to Mathieu's equation would still occur for periods close to the critical periods.

2.4 Mathieu Instability in Irregular Waves

Most studies that examine Mathieu instability are limited to regular waves (Haslum and Faltinsen, 1999; Rho et al., 2002). However, real-life sea conditions consist of irregular waves, which are more complicated than regular waves. Fortunately, attention has been recently given to the study of parametric instability in irregular waves. (Lu et al., 2011) and (Maki et al., 2011) investigated parametric roll of ships in irregular waves while (Yang and Xu, 2015) examined the parametric pitch instability of spar platforms in irregular waves. Their studies revealed that parametric instability does occur in irregular waves and this is why it is essential to examine parametric instability in irregular waves.

Linear theory can be used to represent irregular waves. Linear theory asserts that irregular waves can be assumed to be a superposition of different regular wave elements as follows:

$$\eta(t) = \sum_{i=1}^{n} \eta_i \cos(\omega_i t + \varepsilon_i) \tag{2.8}$$

where

η_i is the amplitude of each wave component.

ω_i is the circular frequency of each wave component.

ε_i is the stochastic initial phase.

The amplitude of each wave element η_i can be expressed as:

$$\eta_i = \sqrt{2S\left(\omega_i\right) \cdot \Delta\omega} \tag{2.9}$$

where

$S\left(\omega_i\right)$ is the wave spectrum which defines the wave energy spectrum density for each frequency.

$\Delta\omega$ is an interval of frequency.

The response amplitude operator (RAO) gives the ratio of the amplitude in response of the body to an incident wave of unit amplitude. The amplitude of the heave motion of a floating body in response to a unit simple harmonic wave can be represented by the heave RAO as follows:

$$H\left(\omega_0\right) = \frac{\xi_{heave}}{\xi}|_{\omega=\omega_0} \tag{2.10}$$

If the heave RAO is applied to the wave spectrum, the heave motion in irregular waves can be expressed as (Mao and Yang, 2015):

$$\xi_3\left(t\right) = \sum_{i=1}^{n} \xi_i \cos\left(\omega_i t + \varepsilon_i\right) \tag{2.11}$$

where

$\omega_i = i\omega_0$

$\xi_i = H\left(\omega_i\right) \cdot \eta_i = H\left(\omega_i\right) \cdot \sqrt{2S\left(\omega_i\right) \cdot \Delta\omega}$

By comparison, the heave motion in regular waves can be denoted as:

$$\xi_3(t) = \xi_3 \cos(\omega_3 t) \tag{2.12}$$

where

ξ_3 is the amplitude of the heave motion.

ω_3 is the frequency of the heave motion.

Thus, the pitch motion in regular waves can be expressed in the form of the classical Mathieu equation as follows (Mao and Yang, 2015):

$$\ddot{\xi}_5(\tau) + c\dot{\xi}_5(\tau) + (\alpha + q\cos(\tau))\,\xi_5(\tau) = 0 \tag{2.13}$$

where

$$\tau = \omega_3 t \tag{2.14}$$

$$c = \frac{C_{55}}{(I_{55} + A_{55})\,\omega_3} \tag{2.15}$$

$$\alpha = \frac{\rho g \nabla \overline{GM}}{(I_{55} + A_{55})\,\omega_3^2} = \frac{\omega_5^2}{\omega_3^2} \tag{2.16}$$

$$q = \frac{\rho g \nabla \alpha \xi_3}{(I_{55} + A_{55})\,\omega_3^2} \tag{2.17}$$

Similarly, the pitch motion in irregular waves can be written in the form of Hill equation as follows (Mao and Yang, 2015):

$$\ddot{\xi}_5(\tau) + 2c\dot{\xi}_5(\tau) + (\alpha + 2q\phi(\tau))\,\xi_5(\tau) = 0 \tag{2.18}$$

where

$$\tau = \frac{\omega_0}{2} t \tag{2.19}$$

$$c = \frac{C_{55}}{(I_{55} + A_{55})\,\omega_3} \tag{2.20}$$

$$q = \frac{2\rho g \nabla \alpha}{(I_{55} + A_{55})\,\omega_0^2} \tag{2.21}$$

$$\alpha = \frac{4\rho g \nabla \overline{GM}}{(I_{55} + A_{55})\,\omega_0^2} = \left(\frac{2\omega_5}{\omega_3}\right)^2 \tag{2.22}$$

$$\phi(\tau) = -\xi_3(\tau) = \sum_{i=1}^{n} \xi_i \cos(\omega_i t + \varepsilon_i) \tag{2.23}$$

The stability diagram can be used to examine the characteristics of Mathieu instability. In the stability diagram, the region below the curves denote stability while the region above the curve denotes instability. Therefore, the stability diagram can be used to assess the degree of stability of an offshore floating structure based upon which region the parameters of the structure falls into.

The Hill infinite determinant approach can be used to solve the Mathieu equation and generate the stability diagram for regular waves excitation. The Bubnov-Galerkin approach can be used to solve the Hill equation and generate the stability diagram for irregular waves. Fig. 2.4 illustrates the stability diagrams under both regular and irregular waves excitation for ease of comparison.

It can be seen from Fig. 2.4 that under irregular waves excitation, the unstable regions are much wider and are more random than under regular waves excitation. Moreover, there are regions under regular waves excitation that are stable but these regions may become unstable under irregular waves excitation. Thus, it is crucial to analyze the Mathieu instability in irregular waves, more so since real life sea conditions comprise of irregular waves.

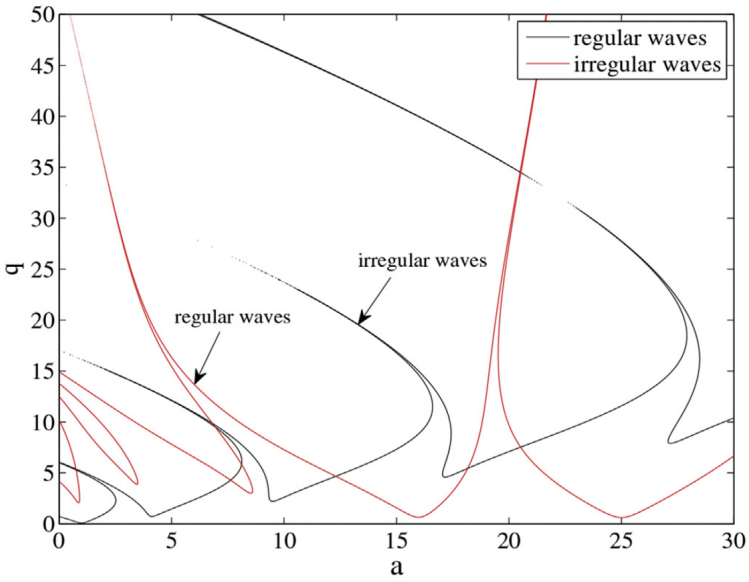

Figure 2.4: *Stability diagram under regular and irregular waves excitation (Mao and Yang, 2015).*

Some other observations can be made from Fig. 2.4. The first three unstable regions are much smaller for irregular waves than for regular waves which implies that it is conservative to predict parametric pitch instability from regular waves excitation. Many stable regions of higher order under regular waves excitation fall under into unstable irregular waves region and so, it can be risky to estimate Mathieu instability solely on regular waves.

It was also found that the parametric pitch instability is largely influenced by the wave parameters or irregular waves (Mao and Yang, 2015). The low-order unstable regions are influenced by the wave phase but the high order unstable regions are not. The stability diagram is greatly influenced by the significant wave height and the wave peak period.

Chapter 3

Examples of Mathieu Instability

3.1 Mathieu Instability of a Spar Platform

Mathieu instability for a spar platform occurs when large heave motions causes a harmonic variation in the pitch restoring coefficients and the heave period is equal to half of the pitch natural period (Koo et al., 2004). The pitch restoring coefficient can be expressed as a function of the displaced volume of water and the metacentric height of the spar. The displaced water volume and the metacentric height change over time due to the heave motion of the spar and the coupling between heave and pitch can be expressed by the Mathieu equation. When the heave period is equal to the pitch natural period, Mathieu instability occurs and the pitch motion increases significantly.

One of the advantages of the spar platform is that its pitch natural frequency is not close to the dominant wave energy frequency. On the other hand, large amplitude resonant motions that vary slowly in time can be excited by second-order wave effects and wind loads and these play a large role in the design of the spar.

Spar platforms have a deep draft of about 200 metres (Koo et al., 2004) and a comparatively smaller waterplane area, which makes them rather insensitive to wave disturbances. They generally exhibit desirable motion behaviour in waves unless they are subjected to long swells, which can be up to 30 seconds. In this situation the heave motion of spars can be severely amplified (Rho et al., 2005). It was found from scaled model tests that the heave motion at resonance can have an amplitude of up to 8 to 10 times greater than the wave amplitude (Rho et al., 2002).

(Ran et al., 1995) investigated the regular wave environment and the usual swell

conditions in West Africa and the North Sea and found that swell waves typically have a peak period of 25 seconds in these regions. A spar platform has a heave natural period of 27 to 30 seconds and a pitch natural period of 45 to 60 seconds. Since the heave natural period is close to the swell waves peak period and the pitch natural period is twice the peak period of swell waves, Mathieu instability occurs because the ratio between the wave period and the pitch natural period is in its main unstable region.

(Haslum and Faltinsen, 1999) used a model test and simplified calculations to examine the Mathieu instability in pitch motion with severe amplitude heave resonance and presented a stability diagram without considering pitch damping effects. (Rho et al., 2002) carried out model tests for a spar platform with a moon-pool, helical strakes, and damping plates and showed that the added damping from the heave plates and helical strakes decrease the heave motion. They also proved in experiments the coupled nonlinear motion in heave-pitch for spar platforms. (Zhang et al., 2002) included pitch damping effects and established a damped Mathieu stability diagram from the Mathieu equation. However, these studies did not study the effects of time varying displacements.

3.1.1 Heave and pitch coupling of a spar platform

The spar platform is a simplified version of the Spar and Torus concept. However, the excitation forces in heave and the damping effects are larger due to the torus being placed at the mean water line. This section, however, describes the Mathieu instability of a conventional spar platform. The pitch restoring stiffness K_{55} is a function of the displaced water volume and the metacentric height $\overline{GM}$, given by $\rho g \nabla \overline{GM}$ in still water. When the spar experiences heave motion with heave amplitude η_3, the metacentric height and displaced water volume are changed and these can be found as:

$$\overline{GM}_{new} = \overline{GM} - \frac{1}{2}\left(\eta_3(t) - \zeta(x_c, y_c, t)\right) \tag{3.1}$$

$$\nabla_{new} = \nabla - A_w\left(\eta_3(t) - \zeta(x_c, y_c, t)\right) \tag{3.2}$$

where

$\overline{GM}$ is the pitch metacentric height corresponding to the restoring at still water.

∇ is the displaced volume of still water.

A_w is the spar water plane area.

$\zeta(x_c, y_c, t)$ is the wave elevation at the flotation center.

The new pitch restoring stiffness can now be calculated as:

$$K_{55,new} = K_{55} - \frac{1}{2}\rho g\left(\nabla + 2A_w\overline{GM}\right)\left(\eta_3(t) - \zeta(x_c, y_c, t)\right) + \frac{1}{2}\rho g A_w\left(\eta_3(t) - \zeta(x_c, y_c, t)\right)^2 \tag{3.3}$$

It can be seen from Eq. 3.3 the coupling between heave-pitch and the pitch stiffness as a function of time. The heave motion can be expressed in the following form:

$$\eta_3(t) = \eta_{3m}\cos(\omega t) \tag{3.4}$$

where

ω is the frequency of the heave motion.

η_{3m} is the heave amplitude.

Then, the pitch motion can be expressed as the classical Mathieu equation as follows:

$$\left[I_{55} + A_{55}\right]\ddot{\eta}_5(t) + C_{55}\dot{\eta}_5(t) + \rho g\nabla\left(\overline{GM} - \frac{1}{2}\eta_{3m}\cos(\omega t)\right)\eta_5(t) = 0 \tag{3.5}$$

The parameters in the Mathieu equation, which are defined as follows, are used to produce the damped Mathieu instability diagram:

$$\alpha = \frac{\rho g\nabla\overline{GM}}{\left(I_{55} + A_{55}\right)\omega^2} = \frac{\omega_5^2}{\omega^2} \tag{3.6}$$

$$\beta = \frac{\rho g\nabla\eta_3}{2\left(I_{55} + A_{55}\right)\omega^2} \tag{3.7}$$

$$c = \frac{C_{55}}{\left(I_{55} + A_{55}\right)\omega} \tag{3.8}$$

where ω_5 is the pitch natural frequency. It should be noted that the heave-pitch coupling of a spar platform cannot be expressed by the Mathieu equation because of

wave elevation effects and the buoyancy changes with time. Therefore, the Mathieu equation has to be modified and the equation of motion for pitch in the time domain simulation can be written as:

$$\left[I_{55} + A_{55}\right] \ddot{\eta}_5(t) + C_{55}\dot{\eta}_5(t) + \rho g \nabla_{new} \left(\overline{GM} - \frac{1}{2} \left(\eta_3 \left(t \right) - \zeta \left(x_c, y_c, t \right) \right) \right) \eta_5(t) = 0 \quad (3.9)$$

The Mathieu equation is a particular case of Hill's equation which is a linear equation with a periodic coefficient (Koo et al., 2004). A damped Mathieu equation is of the form:

$$\ddot{x} + c\dot{x} + \left(\alpha + \beta \cos \left(t \right) \right) x = 0 \quad (3.10)$$

This equation can be solved using Hill's infinite determinant method in order to generate the Mathieu diagram (Koo et al., 2004). The damped Mathieu diagram is shown in Fig. 3.1 and it can be seen that the second unstable region is more affected by the damping effect than the primary unstable region. It can also be seen that including damping into the system results in the unstable regions separating from the α-axis, which implies that including damping into the system reduces the region of instability. However, the primary unstable region is less influenced by damping and so it should be analyzed prudently.

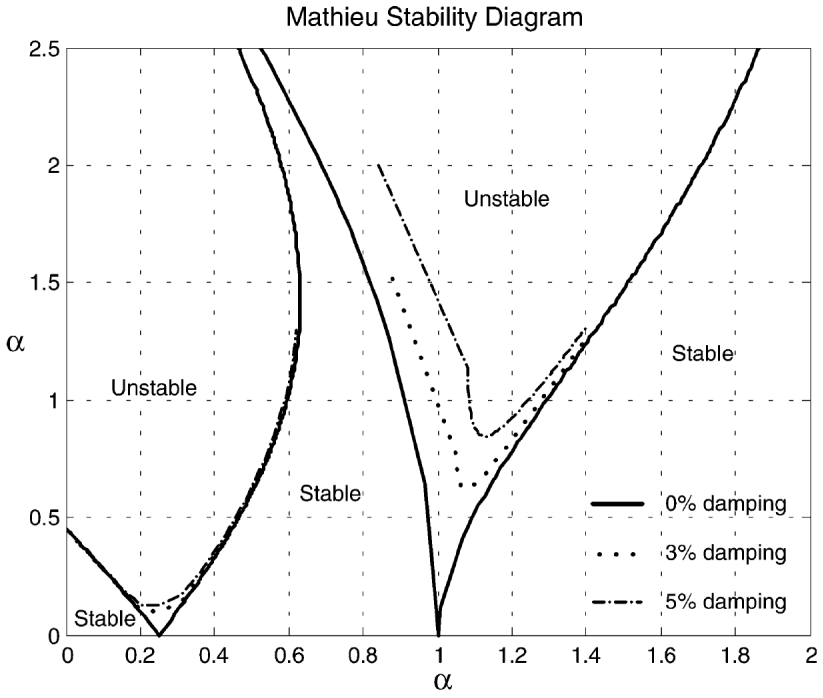

Figure 3.1: *Stability diagram for the damped Mathieu equation (Koo et al., 2004).*

The degree of available damping determines whether or not Mathieu instability can occur. (Koo et al., 2004) found that mooring lines can influence Mathieu instability of a spar platform by increasing the damping and changing the pitch natural period. Therefore, the mooring lines should be carefully modeled in the computer simulations and in the model experiments in basins so that Mathieu instability is not overestimated.

The wave elevation effect is not significant is the wave elevation is small. However, if the wave elevation is large and the there is a phase difference between the heave motion of the spar platform and the wave elevation, the submerged volume and the metacentric height of the spar can be severely influenced by the wave elevation. Thus, if the wave elevation is not taken into account, the Mathieu instability analysis can lead to inaccurate results.

3.2 Parametric Roll of Ships

The occurrence of parametric roll motion has been known for more than half a century (Paulling and R.M., 1959). It occurs because the transverse stability of the ship varies

in time, with an increase in stability when the ship is in the wave trough and a decrease in stability in the wave crest. Parametric roll is an important phenomenon and can lead to considerable loss of cargo and damage of the ship, which for instance, happened to a Post-Panamax container carrier on its journey from Taiwan to Seattle (France et al., 2003). The ship experienced a large roll motion with an amplitude of up to 35° and coupled with a severe pitch and yaw motion which as a result of the periodic change of the transverse stability in head seas.

3.2.1 Development of Parametric Roll Resonance

If a ship is on a wave trough, the average waterplane area is much greater than in calm water. The bow and stern are more deeply submerged than in still water and the part of the midship that is wall-sided is less deep. This results in a greater mean waterplane area and so the metacentric height is greater than its calm water value. On the other hand, when the midship is located on the wave crest, the submerged section of the bow and stern is smaller than in calm water. This results in a smaller mean waterplane area and hence, the metacentric height is smaller than its calm water value. Consequently, the roll restoring moment of the ship varies depending on the ship's longitudinal position with respect to the waves. Fig. 3.2 illustrates how the waterplane area changes with respect to the waves.

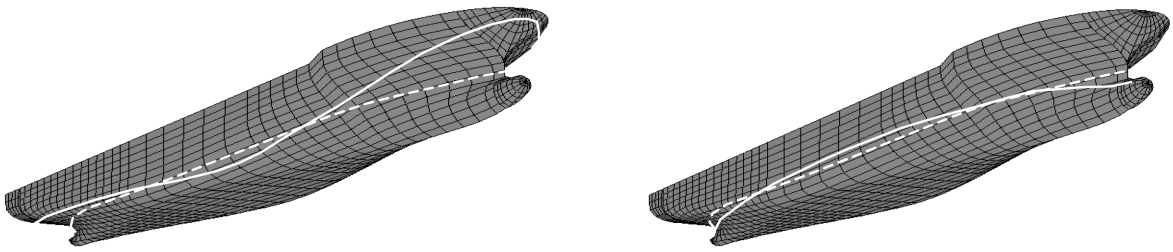

Figure 3.2: *Left: Form of waterline in wave trough. Right: Form of waterline in wave crest. Dotted-line: Form of waterline in calm water (Shin et al., 2004).*

When a ship experiences an excitation in roll motion or roll velocity, for instance one cause by a wind gust, an oscillatory roll motion can be initiated. The natural roll period of the ship in calm water is a function of the ship's stability or restoring moment characteristics and the mass properties. If the roll equilibrium is disturbed and there

is no wave excitation moment, the ship simply rolls at its natural roll frequency.

When the ship encounters head or following seas, that is, when the wavefronts are perpendicular to the ship's centreline, no wave-induced heeling moment occurs. The ship's stability increases when the wave trough is near amidships and decreases on the wave crest (Shin et al., 2004). The roll motions may increase significantly to rather large angles if the stability changes twice during one natural period of roll.

Parametric roll increases most considerably when the following two conditions occur (Shin et al., 2004):

1. The ship encounters waves at a frequency which is about twice the natural roll frequency.
2. The roll excitation occurs in the segment between the wave crest and wave trough amidships position or when the stability increases.

After a roll excitation, the ship rolls back to its initial attitude of zero degrees at the end of the first quarter of the period. Due to its inertia, the ship continues to roll to the other side during the second quarter of the period. If during that segment, the ship experiences a wave crest amidships, the roll restoring moment becomes lower than its calm water value. Therefore, the ship rolls to a bigger angle than it would in calm water despite encountering the same disturbance. This results in a larger roll angle at the end of the second quarter than at the end of the first quarter.

When the ship encounters a wave trough amidships during the third quarter, the roll restoring moment now becomes larger than its still water value and so the ship rolls back to its zero degree attitude with a greater momentum. The situations observed in the first quarter are similar to those observed in the third quarter and those in the second quarter are similar to the observations in the fourth quarter. The roll angle gradually increases with time and this is better illustrated in Fig. 3.3. An example of a time series showing the development of parametric roll in regular waves is shown in Fig. 3.4.

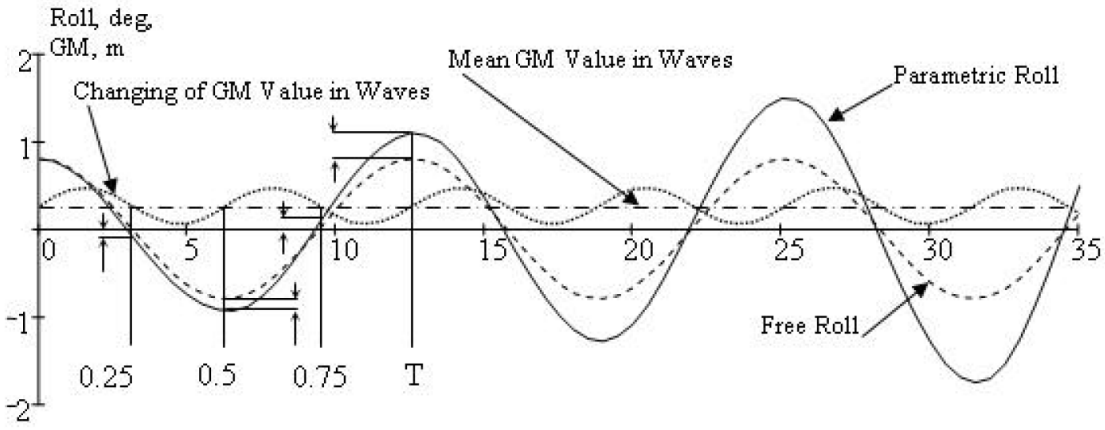

Figure 3.3: *Evolution of parametric roll (Shin et al., 2004).*

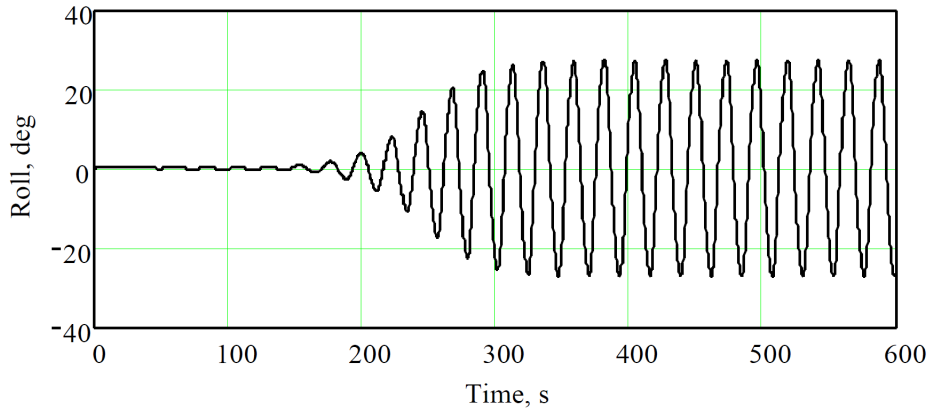

Figure 3.4: *Development of parametric roll in regular waves (wave amplitude 4.2 m, frequency 0.44 Hz, speed 10 knots) (Shin et al., 2004).*

3.2.2 Influence of Roll Damping

When a ship experiences a roll disturbance in calm water, it rolls but the roll amplitudes decrease over time due to the effects of roll damping, as shown in Fig. 3.5. As the ship rolls, it creates waves and eddies and endures viscous drag, all of which contribute to roll damping.

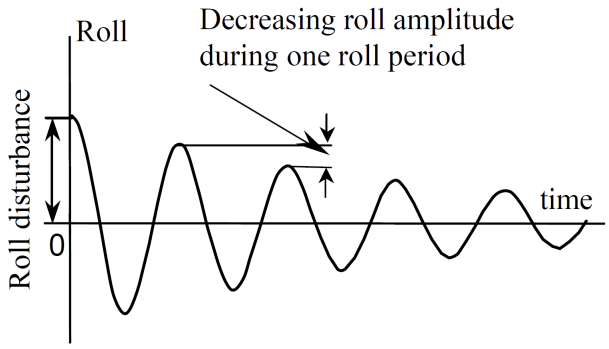

Figure 3.5: *Evolution of parametric roll (Shin et al., 2004).*

Roll damping is critical to the evolution of parametric roll damping resonance. If the decrease in roll amplitude per period due to damping is greater than the increase due to the varying stability in head seas, the roll angles will not increment with time and the phenomenon of parametric roll resonance will not occur. However, in the situation where the decrease in amplitude due to damping is less than the increase due to the changing stability, parametric roll amplitude will increase as resonance develops.

(Shin et al., 2004) found that there is a threshold value for roll damping for each pair of Mathieu parameters p and q. If the roll damping is lower than the threshold value, roll will be unbounded as the solution of the Mathieu equation. If the roll damping is higher than the threshold value, roll is still bounded, even if the Mathieu equation is unbounded. The increment of the Mathieu solution is not adequate to overcome the decrement of roll damping. Furthermore, it also implies that the instability zone is narrower and with the addition of linear damping.

Nonlinear damping has the tendency to increase with roll velocity and it will gradually grow above the damping threshold. This results in the system dissipating more energy than is input from the parametric excitations and hence, leads to the stabilization of the roll amplitude. Even though bilge keel damping is considered to provide considerable nonlinear damping, bilge keel drag coefficients decay substantially with roll amplitude. Thus, linearized damping can offer a very good approximation of actual roll damping behaviour (Shin et al., 2004). It should be emphasized that the occurrence of parametric roll is highly sensitive to the amount of roll damping.

3.2.3 Influence of Forward Speed and Wave Direction

The greatest parametric roll disturbance is caused by longitudinal waves, that is, head and following seas since these create the greatest changes in stability. Parametric roll resonance grows when the stability changes twice as fast as the natural roll frequency or when the ship meets the waves at a frequency which is twice the natural roll frequency.

The natural roll frequency depends mainly on the metacentric height even though it may be influenced by the transverse distributed by the transverse distribution of weight. This implies that the time-varying $\overline{GM}$ value significantly determines whether or not parametric roll resonance may develop in longitudinal seas. Another parameter of influence is the wave length since it refers to the rate of encounter of the waves. Even though the phenomenon of parametric resonance is virtually the same in head and following seas, the heave and pitch motion of the ship has a slightly greater effect on it in head seas than in following seas (Shin et al., 2004).

Chapter 4

Experimental Study of the STC Concept

4.1 Background

The spar-torus combination (STC) concept and its various components are shown in Fig. 4.1. The wind turbine used is the NREL 5 MW reference turbine (Jonkman et al., 2009) while the wave energy converter (WEC) has been motivated by WaveBob (Mouwen, 2008), a concept that was established between 1999 and 2013.

The STC concept harnesses wave energy through the heave motions of the torus with respect to the spar by a hydraulic power take off (PTO) system. The wave energy converter has a rated power of 0.5 MW (Wan, 2016). Rollers and a mechanical system, as shown in Fig. 4.1 act as an interface between the spar and the torus and they respectively prevent large frictional loss as the WEC heaves along the cylinder and restrict the relative horizontal motions. A mechanical brake is installed to stop the relative heave motions in cases of emergency or extreme conditions. An end stop system restrains any excessive relative heave motion under normal operational conditions. Fenders are incorporated on the extremities of the end stop system in order to thwart the considerable forces generated by the WEC.

The hydraulic PTO system transforms the motions of the WEC and the PTO forces using a hudraulic circuit into energy, which is collected in a high pressure accumulator and a low pressure reservoir (Wan, 2016). The accumulated energy can be used to run a hydraulic motor to generate electricity through an electrical generator which is

attached to the motor. A catenary mooring system is installed on the STC concept to supply added yaw stiffness and damping to avoid exaggerated yaw motion. It should be noted that the the STC concept has been designed for an offshore site which is situated 30 km from the west coast of Norway (Li et al., 2013).

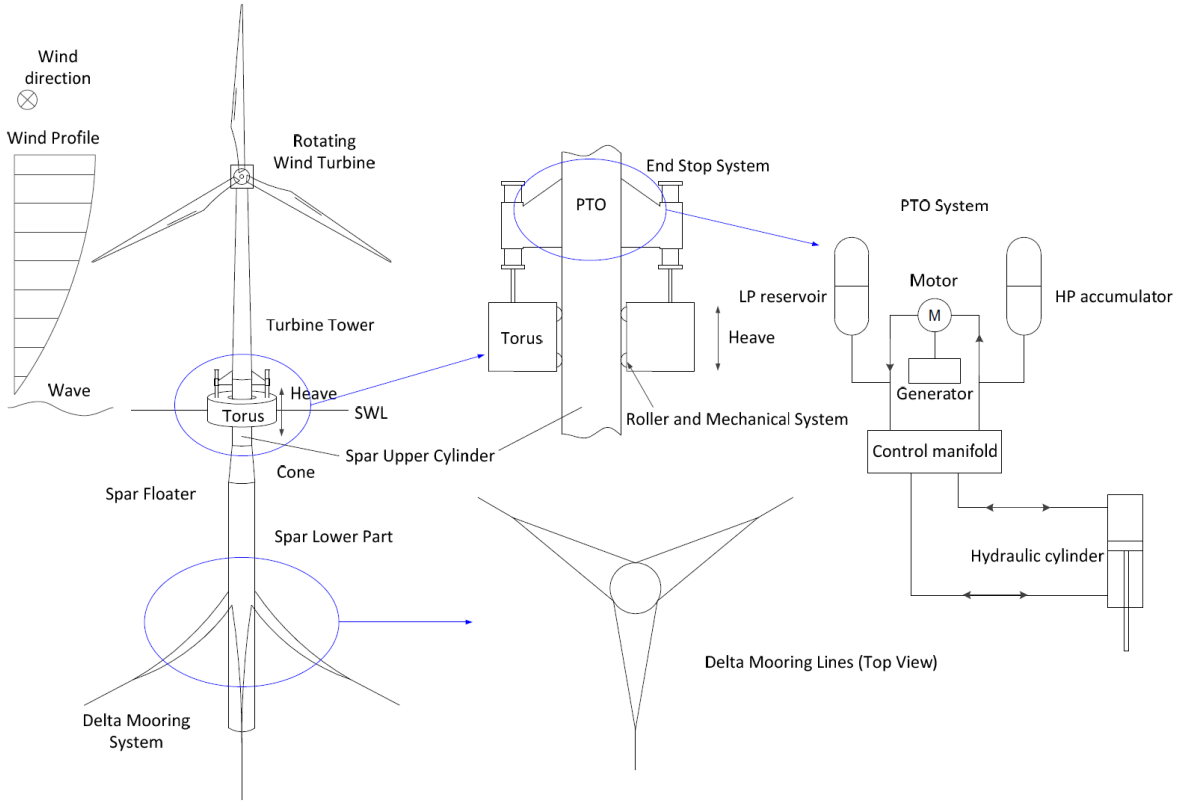

Figure 4.1: *The STC concept and components (Wan, 2016).*

The energy from the wind is converted into electricity with the NREL 5 MW wind turbine. The cut in, rated and cut out wind speeds are respectively 3 m/s, 11.4 m/s and 25 m/s. A conventional variable-speed, variable blade-pitch-to-feather configuration is used for the control system (Wan, 2016). The blade has a constant pitch and the power of the generator increases significantly as the wind speed increases from the cut-in value to the rated value. As the wind speed increases from the rated value to the cut-out value, the control system is triggered to pitch the blades in order to sustain a constant rotational speed and generator power. In extreme wind conditions, the wind turbine is shut down and parked and the blades are aligned to the wind to reduce the aerodynamic

loads. The rotor thrust and power curve for the NREL 5 MW wind turbine are shown in Fig. 4.2.

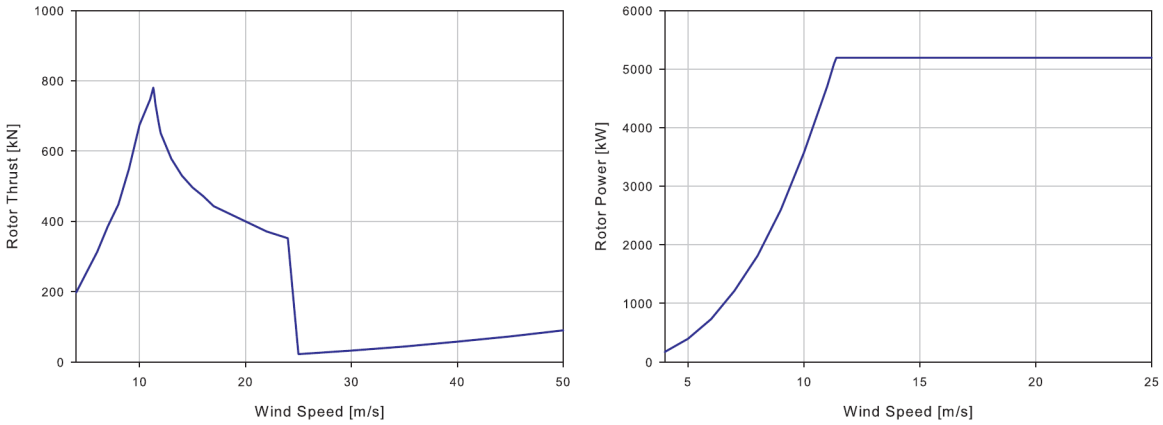

Figure 4.2: *Rotor thrust and power curves as a function of wind speed at full scale (Jonkman et al., 2009).*

4.2 Design and Dimensions

The STC concept comprises of various parts such as the wind turbine, the tower, the mooring system, the lower and upper parts of the spar including the cone structure. The design dimensions of the various components of the STC concept are shown in Table 4.1. It should be noted that the dimensions may not have been flawlessly reproduced in the model tests and some of the actual dimensions in the model tests are marginally different from the design values as shown in Table 4.1 (Wan, 2016). Moreover, the actual dimensions and mass properties in the model tests have been applied to the numerical model to avoid inconsistencies.

Table 4.1: *Full scale dimensions of the different components of the STC concept (Wan, 2016).*

Spar floater	**Design values**	**Model test values Functionality/Survivability**	**Units**
Total length	130	132/132	m
Draft	120	124/122	m
Lower part diameter	10	10/10	m
Lower part length (incl. cone)	110	108/108	m
Upper part diameter	6.5	6.45/6.45	m
Upper part length	20	24/24	m
Fairlead position for mooring	-70 (From SWL)	-70 (From SWL)	m
Tower			
Diameter	6.5	5.5/55	m
Length	77	77/77	m
Tower base postion	10 (From SWL)	10 (From SWL)	m
Wind Turbine			
Rated power	5	-	MW
Rotor diameter	126.3	-	m
Rotor mass	110“	-	ton
Nacelle mass	240	-	ton
Wave energy converter			
Rated power	0.5	-	MW
Height	8	8/8	m
Inner diameter	8	8/8	m
Outer diameter	20	20/20	m
Draft	4	4.5/4.5	m

4.3 Scaling of the STC concept

4.3.1 General Description

Model testing has been an essential component of the development of offshore structures, which began with structures in shallow water since the early fifties (Chakrabarti, 2005). The physical modeling includes the design and construction of a scale model, the reproduction of the environment in an applicable facility, the measuring of the model responses set in the scaled environment and the scaling up of the measured responses to the design values. Duplicating the environment in a small scale enables the replication of the responses that the structure would experience when operating in the offshore site. This is valuable for designers in order to verify their design methods and take necessary corrective measures for the final design of the structure before the manufacturing phase. Small scale model testing is necessary to gain a better understanding of the stability behaviour and survival characteristics of the offshore structure. Moreover, it helps to validate the numerical models, to evaluate higher order effects that might have been omitted or oversimplified in the numerical analysis, and to examine unexpected phenomena.

Testing of a prototype is generally performed on a small scale and scaling laws are employed to scale up the measured data to full scale (Chakrabarti, 2005). The main problem in scaling is to obtain the right scaling law that can represent the similarity accurately. The three major aspects to consider are the similitudes in the geometry of the structure, the fluid kinematics and the dynamics of the structure subjected to the fluid flow. Only when the three conditions are achieved can the model test data be scale up to full scale without any distortion.

A small scale model must be built such that it geometrically resembles the prototype, especially the submerged sections. The scaled model is kinematically similar to the full-scale prototype if the ratio of the fluid velocity and fluid acceleration are maintained. Using Newton's second law ($F = ma$), the excitation forces must be a constant ratio and similar direction such that the model can be considered dynamically similar to the prototype.

A particular scaling might include several ratios, with some being more predominant than others. In most cases, the model structure can only satisfy one of the scaling laws.

Hence, it is essential to have an understanding of the physical processes subjected to the structure and to select the critical scaling law which governs this process (Chakrabarti, 2005).

4.3.2 The STC concept model

The Reynolds number is a dimensionless quantity defined as the ratio of inertial forces to viscous forces and consequently quantifies the relative importance of these two types of forces for given flow conditions (Falkovich, 2011). Reynolds scaling is critical when viscous effects are dominating, especially for aerodynamic fores that act on the wind turbine rotor. However, Reynolds similarity is rather difficult to achieve in a small-scale model and simultaneous satisfaction of both the Reynolds number and the Froude number is even harder (Chakrabarti, 2005).

The Froude law is the accepted method of modelling in hydrodynamics (Chakrabarti, 2005). The Froude number (Fn) is a dimensionless number defined as the ratio of the flow inertia to the gravity forces and ensures similitude between the scaled model and the prototype. It is given by:

$$Fn = \frac{u}{\sqrt{gL}} \tag{4.1}$$

where

u is the flow velocity.

g is the gravitational acceleration.

L is a characteristic length.

To Froude model must satisfy the relationship:

$$Fr = \frac{u_m}{\sqrt{gL_m}} = \frac{u_f}{\sqrt{gL_f}} \tag{4.2}$$

where the subscripts 'm' and 'f' respectively denote the scaled model and the full scale values. The ratio of the two similar dimensions (e.g. length) remains constant and establishes the scale factor, λ, for the model where

$$\lambda = \frac{L_m}{L_f} \tag{4.3}$$

Table 4.2 shows the scale factor of the scale factor of common variables that the Froude model satisfies. The STC model was scaled down using Froude scaling with a ratio $\lambda = 1 : 50$. Hence, the last column in the table gives insight about the quantifying of the different parameters of the scaled model.

Table 4.2: *Scaling of variables using Froude law (Chakrabarti, 2005).*

Variable	**Symbol**	**Scale Factor**	$\lambda = 50$
All linear dimensions	L	λ	50
Fluid or structure velocity	u	$\sqrt{\lambda}$	7.07
Fluid or structure acceleration	$\dot{u}$	1	1
Time or period	t	$\sqrt{\lambda}$	7.07
Force	F	λ^3	1.25E3
Mass	m	λ^3	1.25E3
Structure moment of inertia	I	λ^5	3.125E8
Section moment of inertia	I	λ^4	6.25E4
Volume	V	λ^3	1.25E3
Moment	M	λ^4	6.25E4
Stress	σ	λ	50
Spring constant	K	λ^2	2500
Wave period	T	$\sqrt{\lambda}$	7.07
Wave length	L	λ	50
Pressure	p	λ	50
Gravity	g	1	1
Fluid density	ρ	1	1
Fluid kinematic viscosity	ν	1	1
Reynolds number	Re	$\lambda^{3/2}$	353.6
Keulan-Carpenter number	KC	1	1

Model tests were carried out by (Wan et al., 2014) to validate the numerical model, to examine the behaviour of the STC in the operational and survival conditions and to study the nonlinear phenomena under various wave conditions. The survivability model tests were executed in two different facilities, in the Italian national towing tank (CNR-INSEAN) in Rome, Italy and in the towing tank of MARINTEK in Trondheim,

Norway, to examine the repeatability of the model test (Wan, 2016). In the MWL mode, the two bodies (spar and torus) are locked and move together. In the SUB mode, the torus is completely submerged in the water.

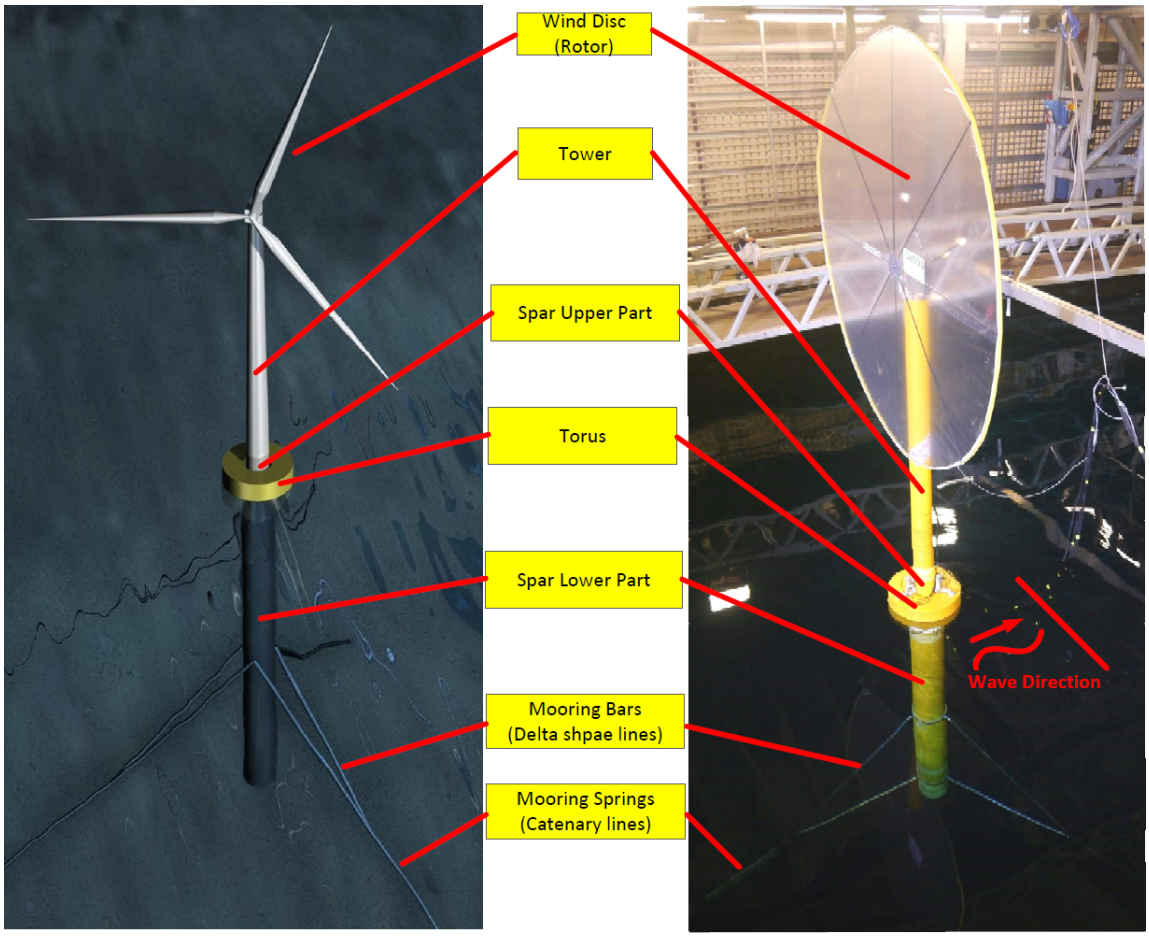

Figure 4.3: *The STC physical model description (Wan, 2016).*

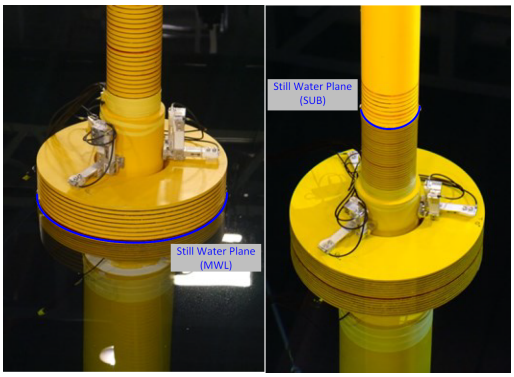

Figure 4.4: *The two survival modes considered (Wan, 2016).*

The physical model of the STC concept and its various components are shown in Fig. 4.3. Different methods, such as a wind drag disc shown in Fig. 4.3, were used to model the wind rotors in order to simulate the aerodynamic effects in the experiments. The most critical part is the connection between the two bodies, that is, the spar and the torus and this is shown in Fig. 4.4. The catenary shape and mass of the mooring lines yield nonlinear stiffness in the horizontal directions while the delta lines provide yaw stiffness and damping to the STC. The mooring system was modeled by three rigid bars, which provide a yaw restoring moment, attached to the spar and three linear springs, which provide horizontal stiffness. Information about the dimension and the weight of the STC model are shown in Table 4.3, Table 4.5 and Table 4.4.

Table 4.3: *Dimensions of STC model (Wan et al., 2014).*

Component	**Parameter**	**Model Scale [m]**	**Full Scale [m]**
Spar lower part	Diameter	0.2	10
	Length	2.16	108
Spar upper part	Diameter	0.129	6.45
	Length	0.48	24
Tower	Diameter	0.11	5.5
	Length	1.54	77
Torus	Height	0.16	8
	Outer diameter	0.4	20
	Inner diameter	0.16	8

Table 4.4: *Weight data for the single-body model and the two-body model (Wan et al., 2014).*

STC		**MWL mode**	**SUB mode**
Total weight (incl. ballast) [kg]		80.29	94.72
Ballast [kg]		34.21	48.64
C.O.G. from WL [m]		1.35	2.00
C.O.G. from geometric centre of torus [m]		1.35	1.48
Radius of gyration with respect to water line [m]	Rxx	1.77	2.28
	Ryy	1.77	2.28
	Rzz	0.09	0.09
Spar & Tower			
Total weight (incl. ballast) [kg]		71.13	85.56
Ballast [kg]		34.21	48.64
C.O.G. from WL [m]		1.53	2.16
Radius of gyration with respect to water line [m]	Rxx	1.89	2.40
	Ryy	1.89	2.40
	Rzz	0.08	0.08
Torus			
Total weight [kg]		9.16	9.16
Ballast [kg]		-	-
C.O.G. from WL [m]		0.00	0.52
Radius of gyration with respect to water line [m]	Rxx	0.14	0.53
	Ryy	0.14	0.53
	Rzz	0.14	0.14

Table 4.5: *Draft of the STC model in different survival modes (Wan et al., 2014).*

Component	**MWL mode [m]**	**SUB mode [m]**
Spar & Tower	2.44	2.96
Torus	0.08	Completely submerged

4.4 Test Procedure

The test setup layout in the MARINTEK and INSEAN towing tanks are shown in Fig. The towing tank in CNR-INSEAN has a length of 220 m, a width of 9 m and a water depth of 3.5 m while that in MARINTEK has a length of 260 m, a width of 10.5 m and a water depth of 10/5.6 m (the depth over an 85 m distance from the wave maker is 10 m and the depth in the other section of the tank is 5.6 m (MARINTEK, 2014)). For an in-depth description of the test facilities, see (Wan et al., 2014).

Various tests such as hammer tests, decay tests, regular and irregular wave tests and irregular wave/wind tests were performed in the model tests. It was necessary to perform calibrations before installing the model and the instrumentation of the devices to ascertain that the measured parameters are correct.

Structural tests were performed at several points on the spar and the torus both before and after immersing the model in the water. This was done to identify the governing dry and wet structural eigenfrequencies. Decay tests were executed for the 6 degrees of freedom so that the natural period and the damping level could be determined from the rigid body motion.

Regular wave tests, over a range of wave frequencies and amplitudes, were performed to find the response amplitude operator (RAO) of the structure. Two sets of regular wave heights were tested to examine the nonlinearity of the response. Tests with only irregular waves were also carried out. Three sea states, including one operational and two extreme, were chosen.

Finally, wind only tests and irregular wave plus wind tests were carried out. A large wind disc was used in operational wind condition whereas a small wind disc was used in the extreme wind condition. Froude scaling was used to downscale the wind velocities. It should be noted that the test procedures were similar for the MWL and SUB modes.

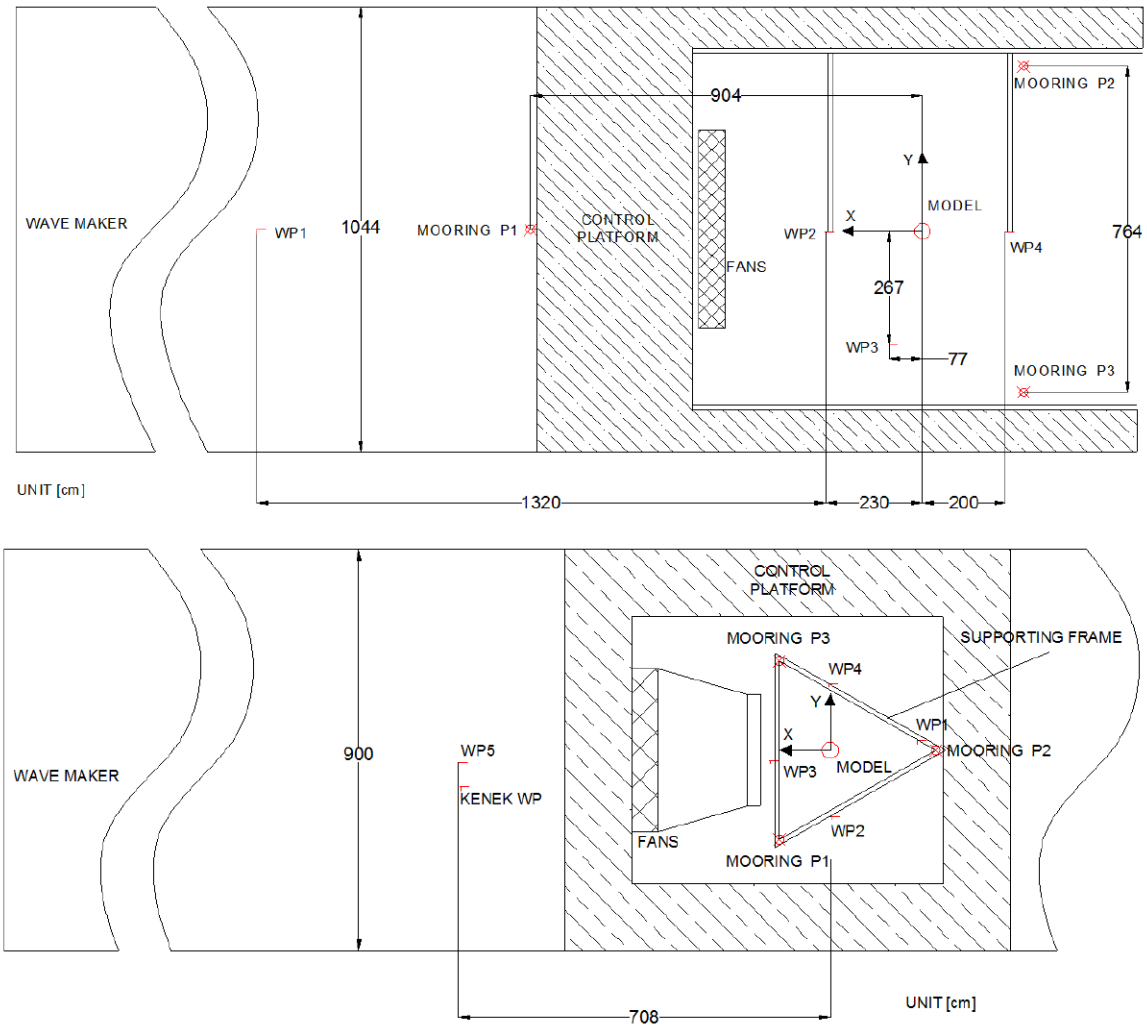

Figure 4.5: *Layout of the testing facility in the MARINTEK (top) and INSEAN (bottom) towing tanks (Wan, 2016).*

Chapter 5

Experimental Results of the STC Concept

5.1 General Overview

The natural periods for surge, heave and pitch motions as well as the damping coefficients were determined from the decay tests. The natural periods and damping ratios are shown in Table 5.1 based on the decay test data from all the model tests. It should be noted that the data has been extracted from the survivability test at MARINTEK.

Table 5.1: *Identified natural periods and damping ratios at full scale (Wan, 2016).*

Motion	**Natural Period** [s]	**Damping** [%]
Surge	98	4.4
Heave	12.8	6.5
Pitch	36.6	4

Regular wave tests were carried out to find the response amplitude operator (RAO) as well as to investigate nonlinear phenomena in large waves. The RAO is only specified when the response can be assumed to be linear and the output frequency is the same as the input frequency. When there is a strong nonlinear response, the amplitude ratio between the response and the wave is more accurate than the RAO because there might be a different frequency in response.

The regular wave test matrix and the occurrence of nonlinear phenomena are shown

in Table 5.2. Water exit and water entry are expected to occur due to the small draft of the torus. Slamming are impulse loads with high pressure peaks and occur during impact of the body with the surrounding fluid (Faltinsen, 1990). Whipping, defined as global elastic transient resonant oscillations, could also be excited with slamming. When the STC experiences large heave motion, the torus is completely out of the water and when the torus enters again, there will be an impact between its bottom and the water. This impact can induce large loads and can be critical for the WEC and the interface between the torus and the spar.

Table 5.2: *Regular wave test matrix and the occurrence of nonlinear phenomenon for MWL case (Wan et al., 2014).*

T	7	9	11	12	13	14	15	17	19	21	23	25
H = 2 m				Slamming								-
H = 9 m	-	Slamming and green water						Mathieu instability				-

The data corresponds to the MWL situation. It can be seen from Table 5.2 that for the case with the small wave height, H = 2m, water exit only occurred in the heave resonance period region, i.e. T = 12 s and T = 13 s. For the large wave height (H = 9 m) case, slamming and green water can be observed with most of the wave periods. For a long wave period of T = 17 s, Mathieu instability was observed. Mathieu instability also occurred but was not fully developed for T = 19 s.

5.2 Cases with Mathieu Instability

Mathieu instability was observed for regular wave tests where the wave height was 9 m and wave periods were 17 s and 19 s, which represent relatively long waves. However, Mathieu instability was not observed during the irregular wave tests.

In the regular wave test of the scale model, Mathieu instability occurred at a wave height $H = 0.18m$ and a wave period $T = 2.405s$. During this event, the pitch motion became unstable and began increasing from about 70 s until it reached a steady state value. This occurred when the period of the pitch motion (about 4.8 s) was twice the wave period (about 2.4 s). It should be noted that it was found from the decay tests that the pitch natural period is 5.1 s (Wan et al., 2014). Moreover, the amplitude of the

pitch motion can be much higher in cases of Mathieu instability than in other cases, as shown in Fig. 5.1. However, even at the steady state, the pitch motion was not purely sinusoidal which could be because the wave period was not exactly half of the pitch natural period.

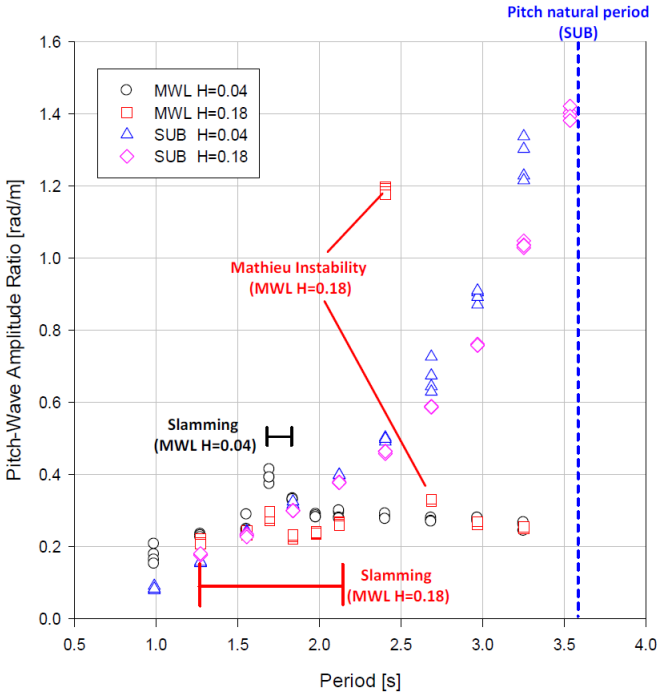

Figure 5.1: *Pitch-wave amplitude ratio in two survival modes (Wan et al., 2014).*

5.3 Mathieu Instability at H = 9 m, T = 17 s

This section describes the observations during the model test. All values in this section correspond to model scale. Fig. 5.2 shows snapshots taken from the videos of the tests performed by (Wan et al., 2014) that helps to see the occurrence of Mathieu instability in heave/pitch. The wave period is about 2.4 s and the wave height is 0.18 m. Each snapshot has been taken approximately 0.6 s after the previous one, that is, the snapshots differ by a quarter of a wave period. The snapshots are taken when the model is in the wave crest, the wave trough and when the wave elevation is zero. All the snapshots add up to two sinusoidal cycles for the wave. A notation used such that the positive pitch motion is clockwise about the zenith and positive heave motion is

towards the zenith.

The first snapshot, at $t = 209.61s$, is taken when the STC concept model is in the wave crest. At that instant, the torus has a positive heave and its centre-line is above the water-line. The spar is vertical the pitch is instantaneously zero but is gradually increasing. Maximum heave occurs about 0.2 s later and then heave decreases as the wave elevation decreases.

In the next snapshot, at $t = 210.24s$, the wave crest starts moving away from the STC model and the water is again at the still water level depth. From the previous snapshot, the heave motion reached its maximum and is now decreasing while the pitch keeps on increasing. The absolute heave is positive, which can be seen from the red centre-line being mostly visible despite the inclination of the STC model.

In the snapshot, at $t = 210.86$, the STC concept model is in the wave trough. The torus is submerged and its centre-line is not visible. Heave is almost at its minimum, which occurs about 0.2 s later, while the pitch motion is now starting to decrease from its maximum positive position.

In the snapshot, at $t = 211.44$, the wave elevation is zero and a new wave starts to approach. Heave is still negative at this point but starts to increase towards a positive value in the next snapshot. Pitch is positive but has been continuously decreasing from the previous snapshot.

The STC concept model experiences another wave crest at $t = 212.00s$. Just as in the first snapshot the torus has positive heave, its centre-line is above the water-line and maximum heave occurs about 0.2 seconds later and then starts to decrease as the wave elevation decreases. However, as opposed to the first snapshot, the pitch is now negative and keeps on decreasing, that is, the STC model now inclines in the opposite direction.

In the next snapshot, at $t = 212.64s$, the wave elevation is zero as the wave crest moves away from the STC model. The heave motion decreases from its maximum position until it becomes negative in the next snapshot. The pitch keeps on decreasing.

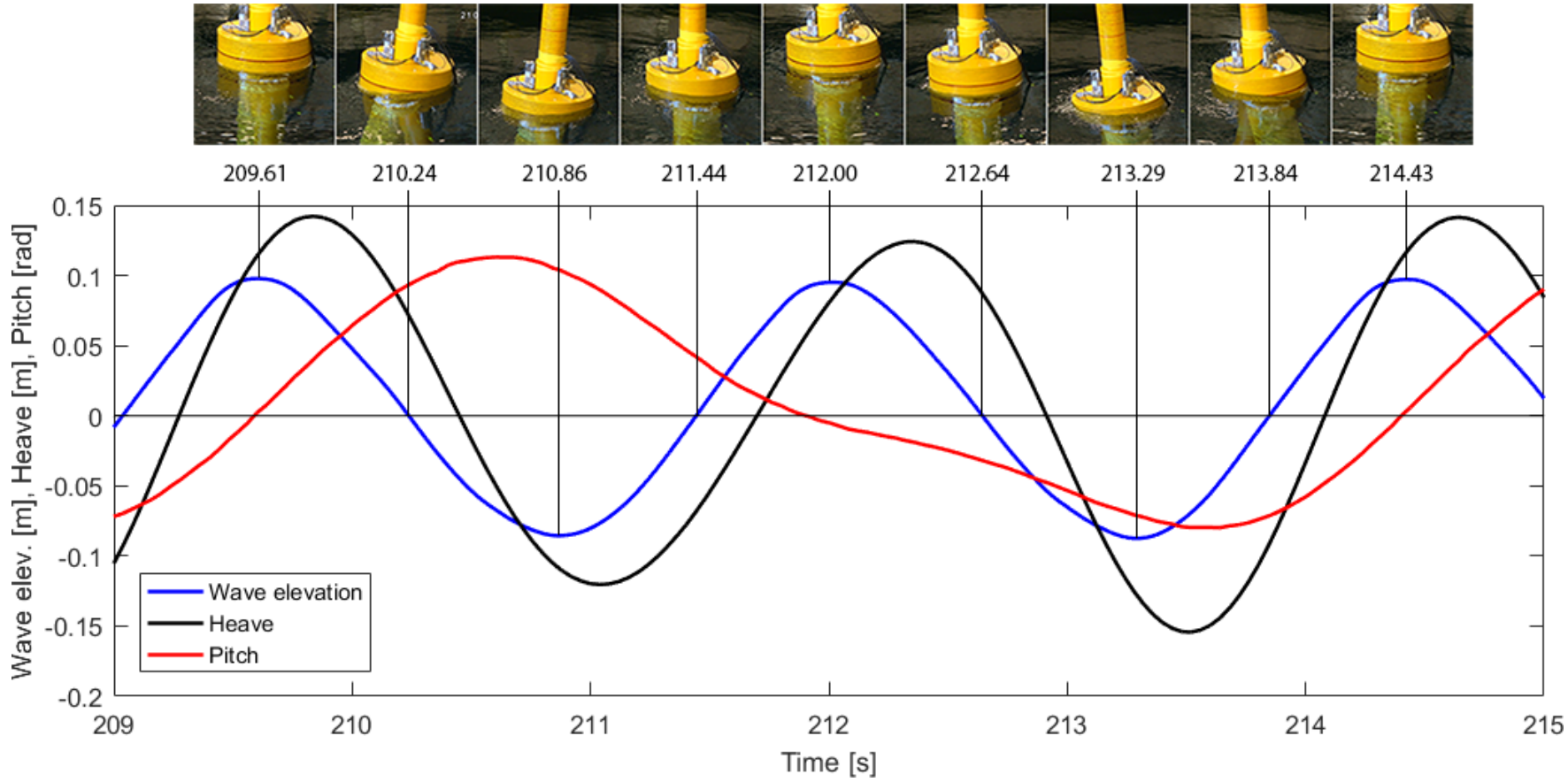

Figure 5.2: *Snapshots of the test video illustrating Mathieu instability (Wan et al., 2014).*

In the snapshot, at $t = 213.29$, the STC concept model is in the wave trough. The torus is submerged and its centre-line is not visible. Heave is almost at its minimum, which occurs about 0.2 s later, while the pitch motion keeps on decreasing.

In the snapshot, at $t = 213.84$, the wave elevation is zero and a new wave starts to approach. Heave is still negative at this point but starts to increase towards a positive value in the next snapshot. Pitch is still decreasing and reaches its minimum value about 0.3 s later and then starts to increase, that it, the STC model starts to incline in the other direction.

In the last snapshot, at $t = 214.43$, the model experiences a third wave crest. This represents two complete wave cycles, two complete heave cycles and one complete pitch cycle. The same phenomena that occurred in the first snapshot can be described here. The whole motion now repeats itself.

and finally a wave trough in the last snapshot at $t = 213.2s$. In the last 4 snapshots, a similar evolution occurs as observed from the second to the 5th snapshot. The notable difference is that the model pitches in the negative direction. There is no difference in the heave motion between the second-to-fifth snapshot and the sixth-to-last snapshot.

Fig. 5.2 shows the occurrence of Mathieu instability as have been described in this section. The period of the incoming waves ($T = 17s$) is about half of the pitch period ($T = 34s$) and this can be seen from the snapshots judging by the elevation and inclination of the STC concept model. Mathieu instability occurred because the wave period is about half of the pitch natural period which is 366 s.

When the model is in the wave trough, the centre-line of the torus is submerged and the model has a higher restoring stiffness which causes it to pitch with more momentum towards the opposite direction. However, at the wave crest, the restoring stiffness is lower because the torus's centre-line is above the water and this causes the pitch motion to overshoot in the direction it was progressing. When the pitch motion is now at the other extreme, the model is again in a wave trough where it is more submerged and this increases its restoring stiffness. Again the same phenomenon occurs, now in the opposite direction, and this characterizes the Mathieu instability in heave/pitch. The pitch motion gradually increases and finally reaches a steady state due to damping effects.

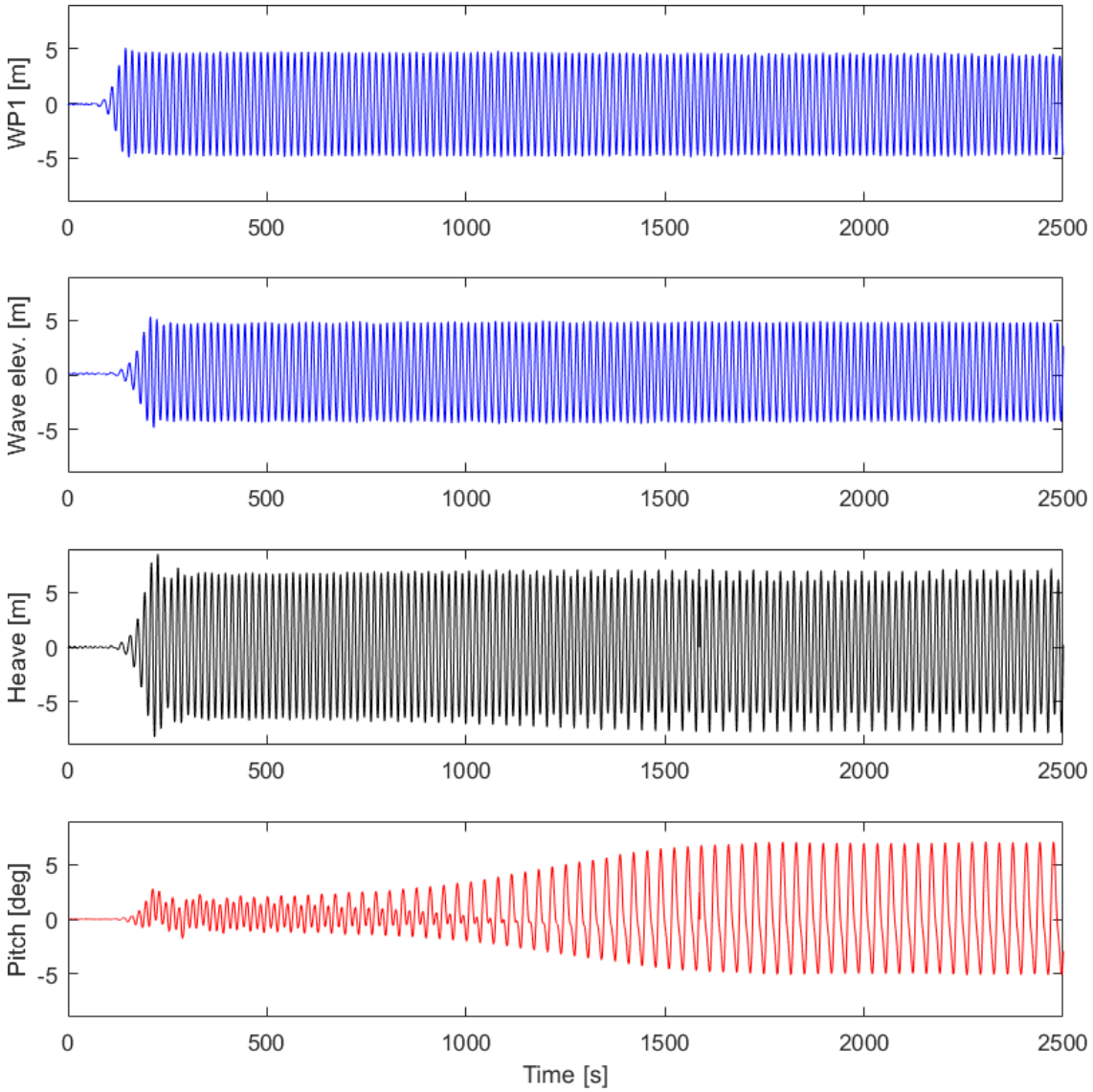

Figure 5.3: *Time series illustrating the development of Mathieu instability.*

The time series showing the development of Mathieu instability is shown in Fig. 5.3. The incoming waves have a wave height of 9 m and a period of 17 s. WP1 and WP2 represent the wave elevation as encountered by wave probe 1 and wave probe 3 respectively. The heave motion occurs mostly at the wave frequency. It can be seen that the pitch frequency slowly changes from the wave frequency to half the wave frequency, due to Mathieu instability. It was found that the mean offset in pitch was about 0.48° and the mean offset in heave about 0.12 m.

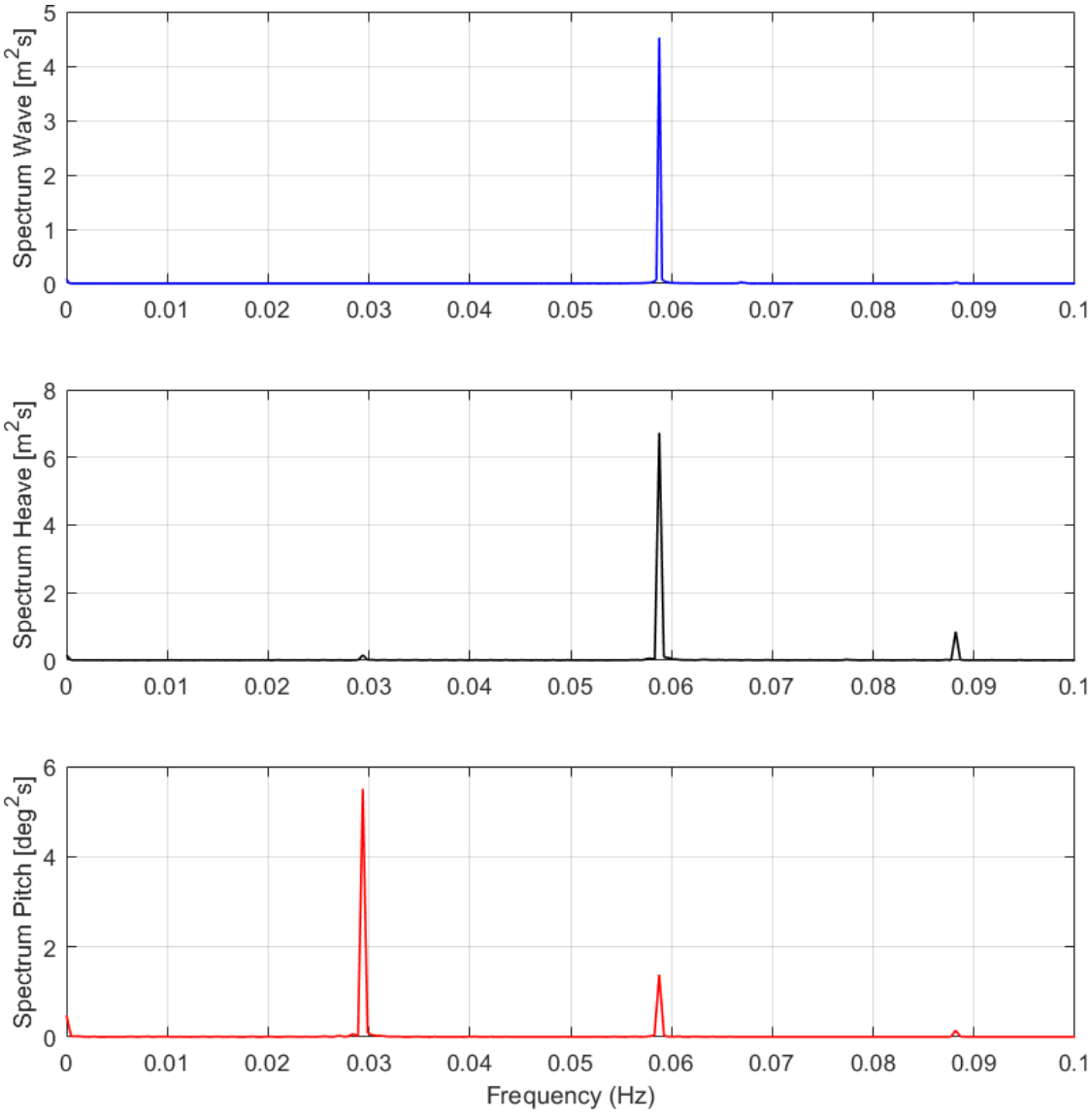

Figure 5.4: *Spectral analysis of the time series with $H = 9$ m and $T = 17$ s.*

Fig. 5.4 shows the spectral analysis of the time series with wave height 9 m and wave period 17 s. The peak for the wave spectrum occurs at 0.059 Hz which is equal to 17 s, which correctly describes the incoming waves. The main peak for the heave spectrum occurs at 0.059 (17 s) but there is also a small peak at 0.088 Hz (11.3 s) which is 1.5 times the wave frequency or about 3 times the pitch natural period. However for the pitch spectrum, the main peak occurs at 0.029 Hz (34 s) which is half the wave frequency and is also close to the pitch natural period of 36.6 s. There is also a small peak for the pitch spectrum at 0.059 Hz (17 s) which corresponds to the wave frequency.

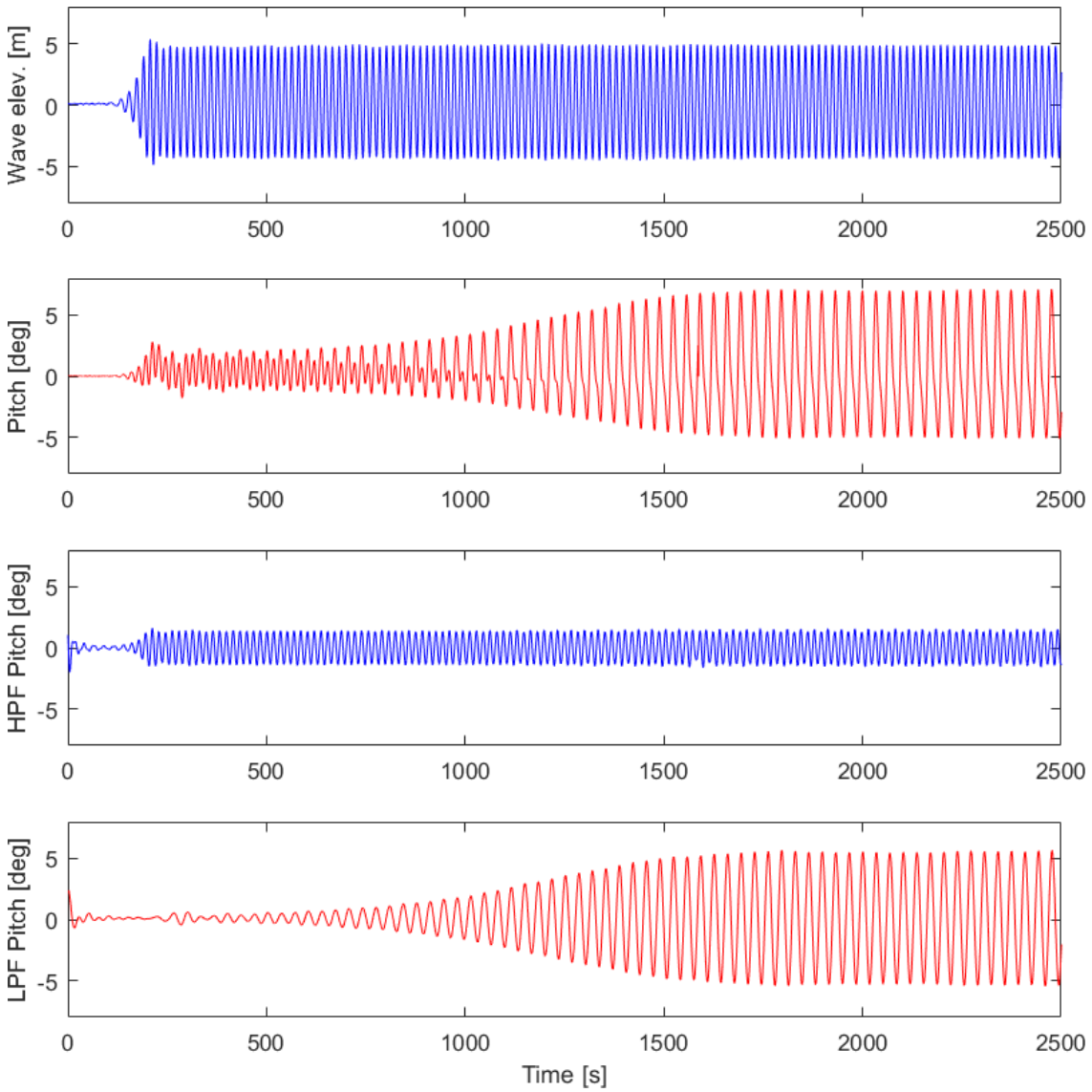

Figure 5.5: *Time series with $H = 9$ m, $T = 17$ s and with signal filtering.*

Fig. 5.5 shows the time series with wave height 9 m and wave period 17 s. A high pass filter and a low pass filter have been applied to the pitch signal to gain insight into the two frequencies that make up the pitch motion. Starting from the top, the first and second plots show the time series of the wave elevation and the pitch motion respectively. The third plot shows the time series of the pitch motion after a high pass filter was applied. It shows the high frequency component of pitch which is equal to the wave frequency. The fourth plot shows the time series of the pitch motion after a low pass filter has been applied. It can be seen that the amplitude of the low frequency

component of pitch, which is equal to half the wave frequency, slowly increases as the STC concept is subjected to the incoming waves which a frequency about half of the natural pitch frequency. It was also found that during the steady state phase, the amplitude of the low frequency component of pitch was about 2.2 times higher than that of the high frequency component.

The maximum pitch that occurred for sea state with regular wave height 9 m and wave period 17 s was 7.3°. An important parameter is the time taken for Mathieu instability to fully develop. The amplitude of the pitch motion varies slightly after Mathieu instability has been fully developed and so, an arbitrary value of 95% was used to in the calculation. It was found that it took about 1500 s from the the first incoming waves to the point where the amplitude of the pitch motion is 95% of its maximum value. In other words, it took 90 such wave cycles for Mathieu instability to progress to its final stage.

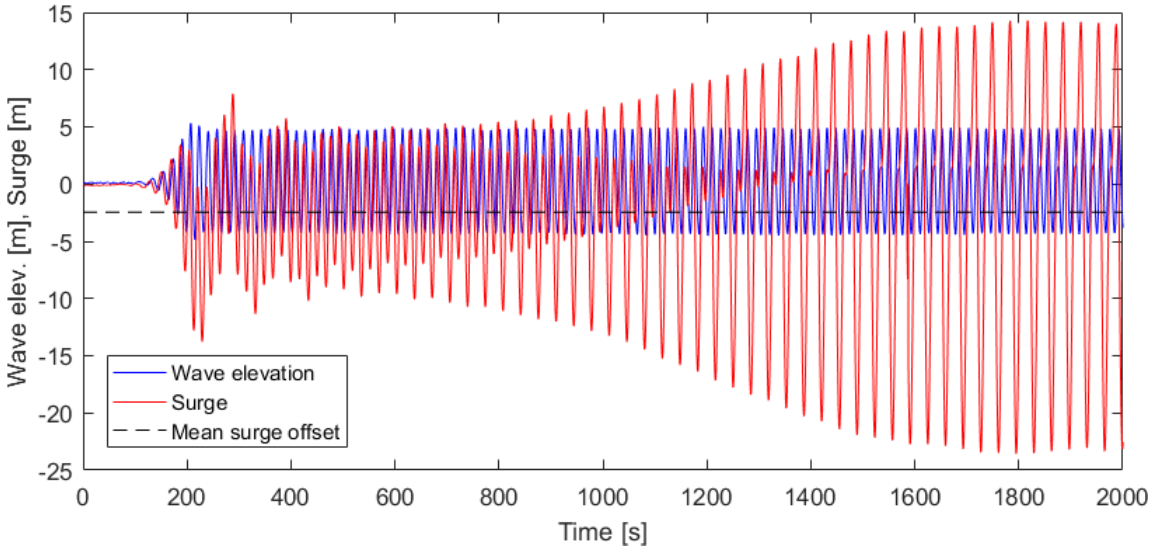

Figure 5.6: *Time series of the surge motion with $H = 9$ m, $T = 17$ s.*

The STC concept also experienced fluctuations in its surge motion due to the incoming waves. As shown in Fig. 5.6 there was a mean offset in surge of -2.45 m (the negative sign implies in the direction of wave propagation, as per Dr. Ling Wan's sign convention) from the original position, that is, the condition without waves. After Mathieu instability fully developed, the surge motion oscillated about its mean offset with an amplitude of about 19.4 m. The furthest point the floating body reached was

24 m away from its original position.

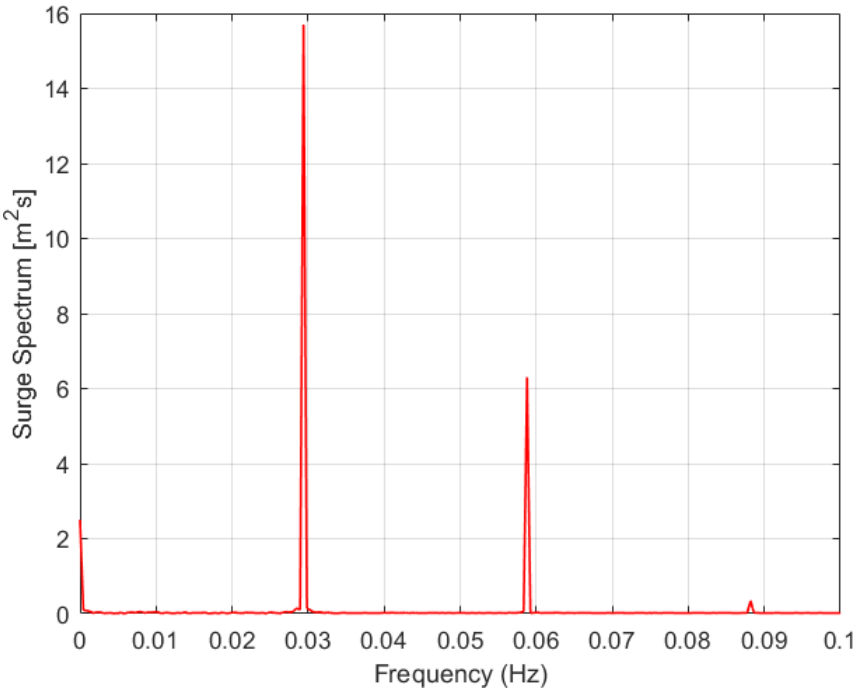

Figure 5.7: *Spectral analysis of the surge motion with $H = 9$ m, $T = 17$ s.*

It can be seen from the spectral analysis of the surge motion in Fig. 5.7 that there were mainly 2 peaks. The highest peak occurs at half the wave frequency and the other peak occurs at the wave frequency. It should be noted that just as the case for the pitch motion, the surge period changed from a value equal to the wave period to a value equal to twice the wave period.

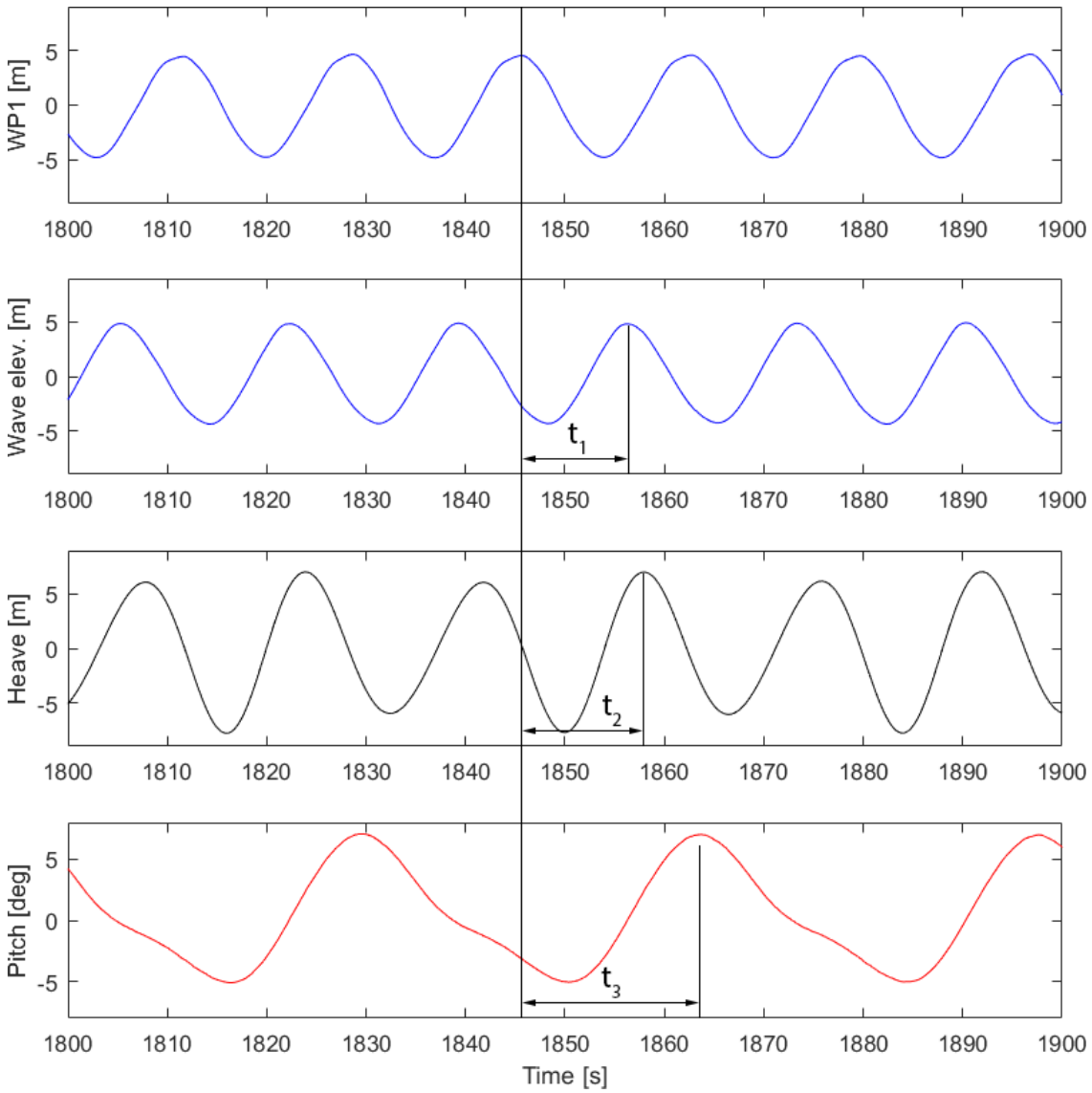

Figure 5.8: *Time series with $H = 9$ m, $T = 17$ s showing the phase differences.*

As can be seen from Fig. 5.8, there were phase differences amongst the wave and the motions. It should be noted that the heave motion repeated itself every two periods and the pitch motion was not sinusoidal. The incoming waves can be described using the following equation:

$$\zeta = \zeta_a \cos(\omega t - kx + \varphi) \tag{5.1}$$

where

ζ is the description of the wave.

ζ_a is the amplitude of the wave.

ω is the cyclic wave frequency.

t is the time.

k is the wave number.

x is the distance of a point from the wave.

φ is the phase shift.

The wave number in deep water is given by:

$$k = \frac{\omega^2}{g} \tag{5.2}$$

From Fig. 5.8, it was found that:

$t_1 = 10.65$ s

$t_2 = 12.41$ s

$t_3 = 18.07$ s

It can be calculated that a wave with period 17 s has a cyclic frequency, ω, of 0.37 rad/s and a wave number, k, equal to 0.014. Since the distance between the wave probes and the STC concept are known, the phase shifts can be calculated. It should be specified that the phase shifts were computed when the STC concept was at a position defined by its mean offset in surge.

It was found that there is a phase shift, φ_{heave}, of -37.2° (time delay of 1.76 s) between the wave profile and the heave motion. There is a phase shift, φ_{pitch}, of -157° (time delay of 7.42 s) between the wave profile and the pitch motion. It should be noted that the wave profile is taken at the mean offset in surge and the negative sign in the phase shifts of the motions represent a time lag of the motions with respect to the wave profile.

5.4 Mathieu Instability at H = 9 m, T = 19 s

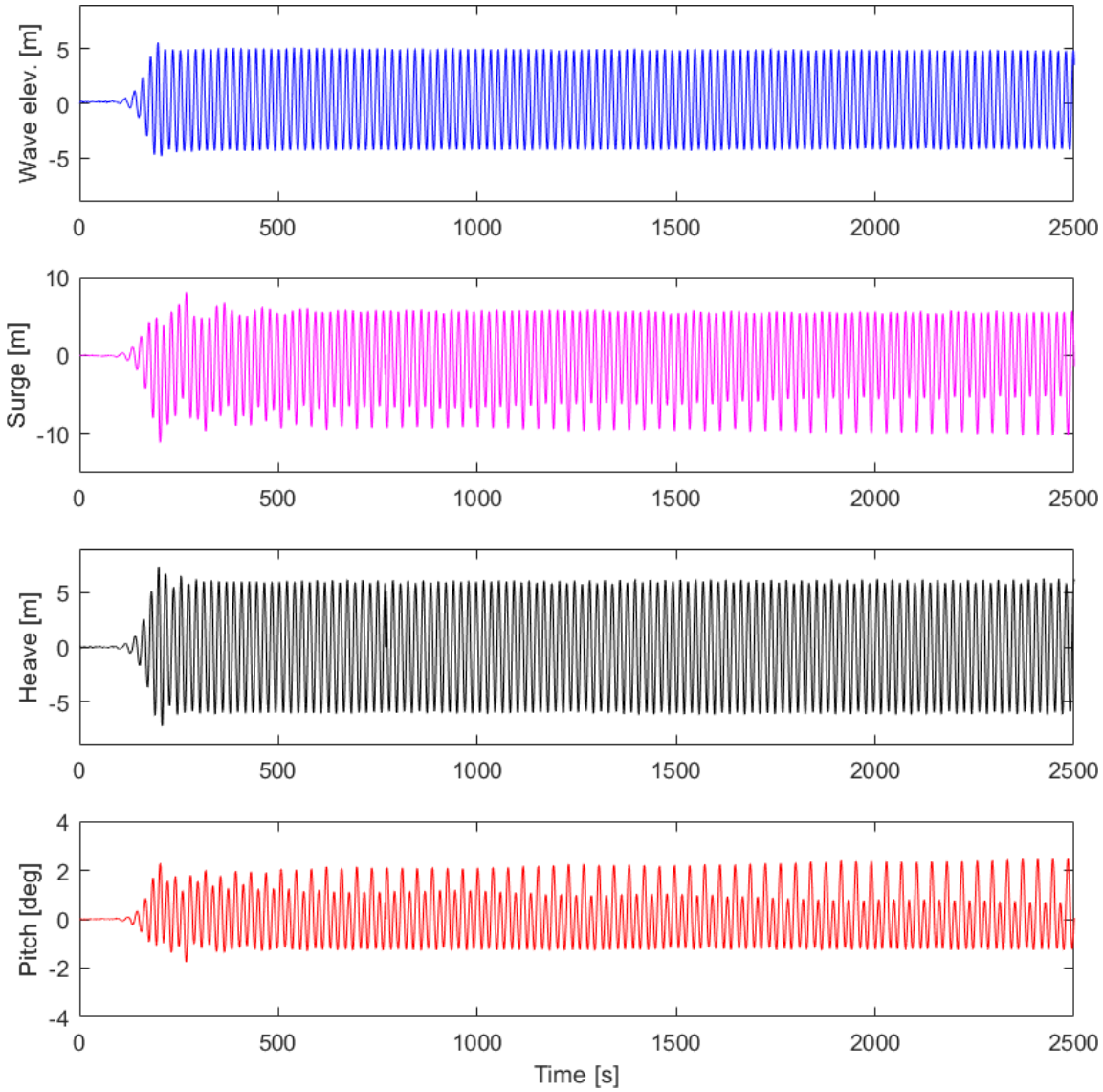

Figure 5.9: *Time series with H = 9 m and T = 19 s.*

Mathieu instability was also observed in conditions where the wave height and wave period were respectively 9 m and 19 s. However, the phenomenon was less pronounced than in the case where the wave period was 17 s. Fig. 5.9 shows the time series of the wave profile and the motions in surge, heave and pitch. The pitch motion does show a progression whereby it gradually evolves from having a frequency equal to the wave

frequency to having a frequency equal to half the wave frequency but does not fully reach the state where it is dominated by the lower frequency component, as compared to the 17 s wave period case.

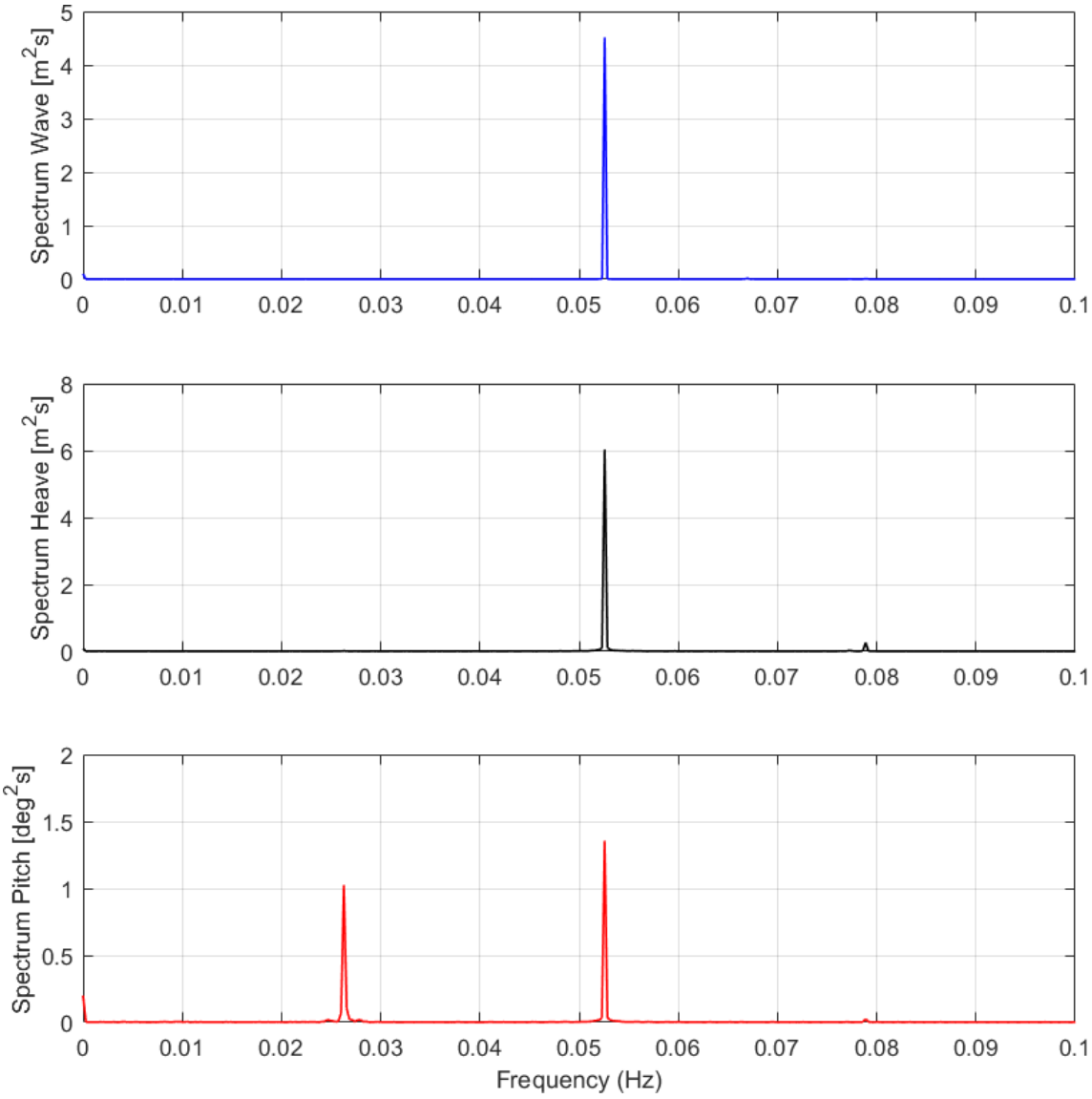

Figure 5.10: *Spectral analysis of the time series with $H = 9$ m and $T = 19$ s.*

Fig. 5.10 shows the spectral analysis of the time series with wave height of 9 m and wave period of 19 s. The main peak for the spectra of the wave profile, the heave motion and the pitch motion all occur at a frequency of 0.0525 Hz which corresponds to a period of 19 s, equal to the wave period. It can be seen from the pitch spectrum that

the main peak occurs at the wave frequency instead of at half of the wave frequency (as in the case with T = 17 s), thus indicating that Mathieu instability is not as developed.

5.5 No Mathieu Instability at H = 2 m, T = 17 s

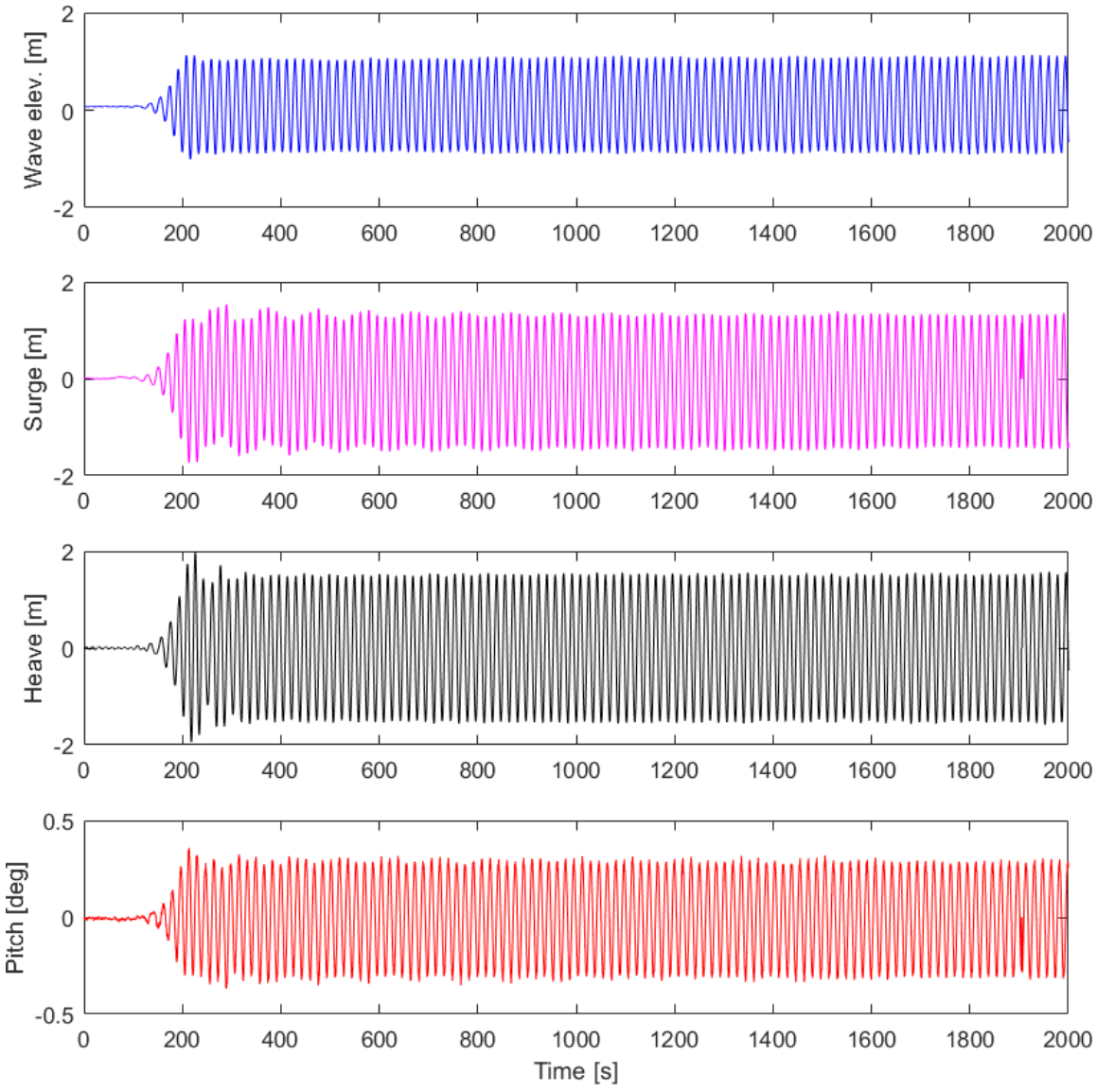

Figure 5.11: *Time series with H = 2 m and T = 17 s.*

Fig. 5.11 shows the time series for a wave height of 2 m and a wave period of 17 s. As previously described, Mathieu instability occurred for H = 9 m and T = 17 s. When

the wave height is changed to a smaller one of 2 m, Mathieu instability does not occur, as shown in the time series in Fig. 5.11. For the whole duration of the motion, the pitch oscillates at the wave frequency and this is the case for the heave motions as well, as seen in Fig. 5.12. The frequency of pitch motion does not evolve towards half the wave frequency as typically found in cases of Mathieu instability. Therefore, it can be concluded that the wave height is a critical parameter that can determine whether or not Mathieu instability occurs.

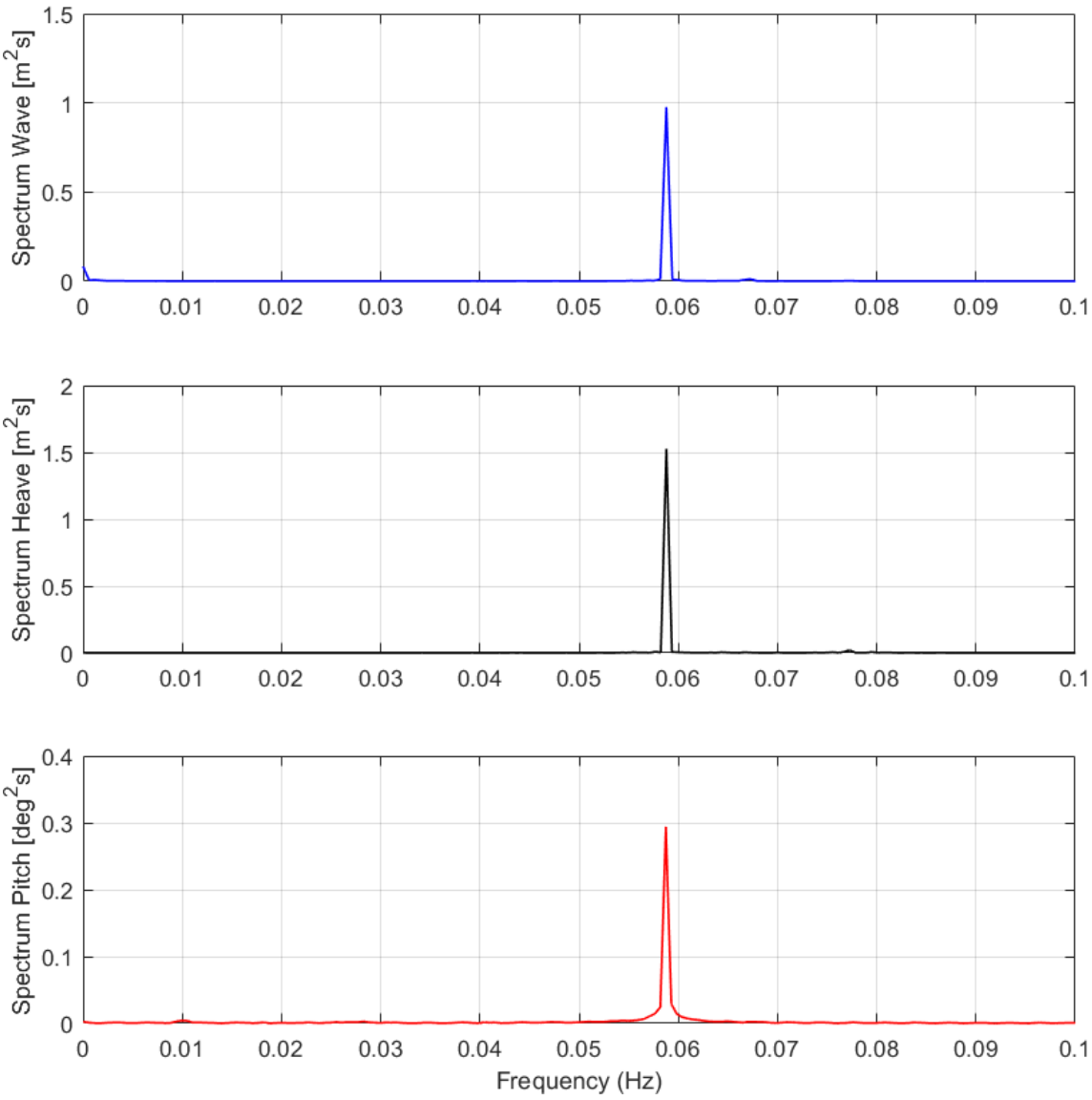

Figure 5.12: *Spectral analysis of the time series with $H = 2$ m and $T = 17$ s.*

Chapter 6

Numerical Modelling

Two SIMO models of the STC concept have been provided by Dr. Ling Wan. One is a 2-body system, that is, the spar and torus are modeled separately and for the survivability modes, there is a very high stiffness in the coupling between the spar and the torus so that the torus remains fixed to the spar. The other model is a 1-body system where the spar and torus are modeled as one body only. It should be noted that some of the components, such as the mooring lines, were added into the 1-body model from the 2-body model and that in the thesis work, all the tests were run only on the 1-body model.

In order to get an understanding of how those models behave in SIMO, simplified models are created in MATLAB. The first model is a 1-DOF (degree of freedom) model that accounts for pitch only and the second model is a 2-DOF which accounts for the coupling between surge and pitch. The results of the MATLAB code are then compared with the SIMO models.

SIMO, short for Simulated Workbench for Marine Operations, is a robust tool used in the modelling and analysis of marine structures (Marintek, 2016). It is being developed as a Joint Industry Project by Marintek and Statoil. SIMO is the software that is used throughout the thesis work to analyze the STC concept in the time domain with all its degrees of freedom.

6.1 Governing Equations

The equation of motion for a rigid floating system with zero forward speed in sea waves can be expressed in the frequency domain as (Newman, 1977):

$$-\omega^2 \left(\mathbf{M} + \mathbf{A}\left(\omega\right)\right) \mathbf{x}\left(\omega\right) + i\omega \mathbf{B}\left(\omega\right) \mathbf{x}\left(\omega\right) + \mathbf{R}\mathbf{x}\left(\omega\right) = \mathbf{F}\left(\omega\right) \tag{6.1}$$

where

ω is the wave frequency.

$\mathbf{M}$ is the structural mass matrix.

$\mathbf{A}\left(\omega\right)$ is the frequency dependent added mass matrix.

$\mathbf{B}\left(\omega\right)$ is the radiation damping matrix.

$\mathbf{R}$ is the restoring matrix.

$\mathbf{F}\left(\omega\right)$ is the external force vector.

The linear problem can be efficiently solved in the frequency domain but in the analysis of the STC concept, nonlinear phenomena such as Mathieu instability can only be considered in the time domain. The equation of motion in the time domain can be expressed as (Wan, 2016):

$$\left(\mathbf{M} + \mathbf{A}\left(\infty\right)\right) \ddot{\mathbf{x}}\left(t\right) + \mathbf{C}\dot{\mathbf{x}}\left(t\right) \left|\dot{\mathbf{x}}\left(t\right)\right| + \int_0^t \mathbf{k}\left(t-\tau\right) \dot{\mathbf{x}}\left(\tau\right) \mathrm{d}\tau + \mathbf{R}\mathbf{x}\left(t\right) = \mathbf{F}\left(t, x, \dot{x}\right) \tag{6.2}$$

where

$\mathbf{A}\left(\infty\right)$ is the added mass matrix at infinite frequency.

$\mathbf{x}, \dot{\mathbf{x}}$ and $\ddot{\mathbf{x}}$ are the displacement, velocity and acceleration vectors in the time domain respectively.

$\mathbf{C}$ is the quadratic viscous damping coefficients matrix.

$\mathbf{F}\left(t, x, \dot{x}\right)$ is the summation of the external forces in the time domain.

$\mathbf{k}\left(t-\tau\right)$ is the retardation function matrix due to the wave memory effects.

The retardation function can be expressed as (Wan, 2016):

$$\boldsymbol{k}(\tau) = \frac{2}{\pi}\int_0^\infty [\mathbf{B}(\omega) - \mathbf{B}(\infty)]\cos(\omega t)\,\mathrm{d}\omega = -\frac{2}{\pi}\int_0^\infty \omega\,[\mathbf{A}(\omega) - \mathbf{A}(\infty)]\sin(\omega t)\,\mathrm{d}\omega \tag{6.3}$$

where

$\mathbf{B}(\infty)$ is the radiation damping matrix at infinite frequency.

$\mathbf{B}(\omega) = 0$ for floating structures with zero forward speed.

A simple 1-DOF model of the STC model from Dr. Ling Wan is established in MATLAB. The only degree of freedom is pitch and the heave motion can be enforced to see how the pitch response changes with different wave heights and wave periods.

Before deriving the governing equations, the coordinate system needs to be defined. Fig. 6.1 shows the axis system used and the rigid body motion modes. The direction of the arrows represent positive motion. It should be noted that incoming waves come from the negative x-axis towards positive x-axis. The axis system is referred to as the global axis system and it stays fixed, that is, it is the body that moves with respect to the global axis. The vertical centre-line of the spar and torus lies along the z-axis and the centre of the torus lies at the global axis origin.

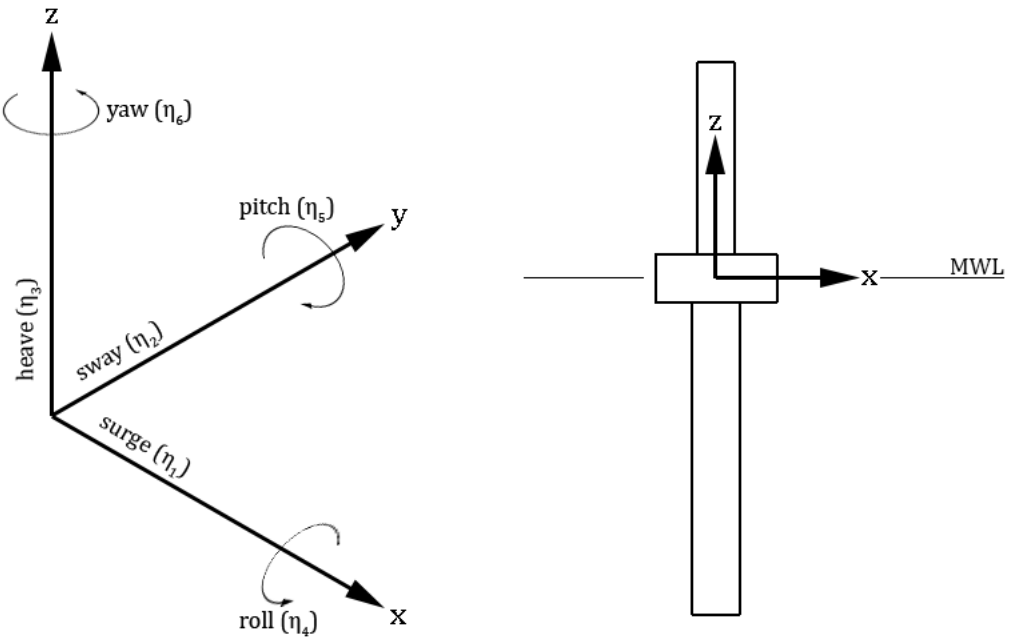

Figure 6.1: *Definition of axis system and schematic of the STC concept (not to scale).*

The equation of motion of pitch of the 1-DOF model can be expressed as:

$$[I_{55} + A_{55}]\,\ddot{\eta}_5 + B_{55}\dot{\eta} + K_{55}\eta_5 = F \tag{6.4}$$

where

I_{55} is the moment of inertia around the pitching axis.

A_{55} is the pitch added moment.

B_{55} is the potential damping in pitch.

K_{55} is the stiffness of the system.

F is the wave force excitation.

For the following equations, the subscript-s refers to the spar and the subscript-t refers to the torus:

$$K_{55} = K_{55s} + K_{55t} \tag{6.5}$$

$$K_{55s} = \rho g \nabla_s KB_s + \rho g I_s - m_s g KG_s \tag{6.6}$$

$$K_{55t} = \rho g \nabla_t KB_t + \rho g I_t - m_t g KG_t \tag{6.7}$$

where KB is the centre of buoyancy and KG is the distance from the keel to the metacentre. I denotes the second moment of area.

$$\nabla_s = \frac{\pi}{4} D_s^2 \left(draft_s + \zeta - \eta_3 \right) \tag{6.8}$$

$$\nabla_t = \frac{\pi}{4} \left(D_{t,outer}^2 - D_{t,inner}^2 \right) \cdot \left(draft_t + \zeta - \eta_3 \right) \tag{6.9}$$

$$KB_s = \frac{\left(draft_s + \zeta - \eta_3 \right)}{2} \tag{6.10}$$

$$KB_t = \frac{\left(draft_t + \zeta - \eta_3 \right)}{2} \tag{6.11}$$

The second moment of area are:

$$I_s = \frac{\pi}{64} D_s^4 \tag{6.12}$$

$$I_t = \frac{\pi}{64} \left(D_{t,outer}^4 - D_{t,inner}^4 \right) \tag{6.13}$$

The mass of water displaced are:

$$m_s = \rho \nabla_s \tag{6.14}$$

$$m_t = \rho \nabla_t \tag{6.15}$$

Using H as the wave height and ω as the wave frequency, the wave elevation can be taken as:

$$\zeta_3(t) = \frac{H}{2} \cos\left(\omega t \right) \tag{6.16}$$

The heave motion is taken as:

$$\eta_3(t) = \eta_{3a} \cos(\omega t + \varphi) \tag{6.17}$$

The wave excitation force is given as:

$$F = F_0 \cos(\omega t + \varphi) \tag{6.18}$$

It should be noted that the pitch stiffness K_{55} is a function of displaced volume ∇ and metacentric height $\overline{GM}$, represented by $\rho g \nabla \overline{GM}$ in still water (Rho et al., 2002). The metacentric height and displaced volume can be obtained by:

$$\overline{GM}_{new} = \overline{GM} - \frac{1}{2}(\eta_3(t) - \zeta(x_c, y_c, t)) \tag{6.19}$$

$$\nabla_{new} = \nabla - A_w(\eta_3(t) - \zeta(x_c, y_c, t)) \tag{6.20}$$

Neglecting the wave elevation effect and based on a new metacentric height and displaced volume, the new pitch restoring stiffness, $K_{55,new}$, can be calculated:

$$K_{55,new} = K_{55} - \frac{1}{2}\rho g\left(\nabla + 2A_w\overline{GM}\right)(\eta_3(t)) + \frac{1}{2}\rho g A_w(\eta_3(t))^2 \tag{6.21}$$

Thus, to account for the change in hydrostatic stiffness due to the heave motion, Eq. 6.4 can be written as:

$$[I_{55} + A_{55}]\ddot{\eta}_5 + B_{55}\dot{\eta} + K_{55,new}\eta_5 = F \tag{6.22}$$

Viscous drag varies as the derivative of the pitch motion and can be represented by the term $B_{55}|\dot{\eta}_5|\dot{\eta}_5$.

The equation of motion of pitch can then be expressed as:

$$[I_{55} + A_{55}]\ddot{\eta}_5 + B_{55}\dot{\eta} + B_{55}|\dot{\eta}_5|\dot{\eta}_5 + K_{55,new}\eta_5 = F \tag{6.23}$$

The mooring lines contribute to the stiffness of the model and this can be represented by a term $K_{55,moor}$. The total stiffness is thus comprised of the sum of the hydrostatic stiffness and the mooring lines stiffness, which are both functions of the heave motion:

$$K_{55}(\eta_3) = K_{hydro}(\eta_3) + K_{moor}(\eta_3) \tag{6.24}$$

This can be further simplified into:

$$K_{55}(\eta_3) = K_{hydro,0} + \Delta K_{hydro}(\eta_3) + K_{moor,0} + \Delta K_{moor}(\eta_3) \tag{6.25}$$

where the constant terms with subscripts-0, refer to the case where there is no heave motion. Both the hydrostatic stiffness and the stiffness provided by the mooring lines are influenced by the heave motion and this is denoted by the Δ-terms.

Using the above substitutions, the equation of motion that is solved in MATLAB can be expressed as:

$$[I_{55} + A_{55}]\ddot{\eta}_5 + B_{55}\dot{\eta} + B_{55}|\dot{\eta}_5|\dot{\eta}_5 + [K_{55}(\eta_3)]\eta_5 = F \tag{6.26}$$

Eq. 6.26 is solved using the fourth-order Runge-Kutta (ode4) method. This involves computing the model state at the next time step as an explicit function of the current value of the state and state derivatives (Mathworks, 2016).

6.2 Entending to a 2-DOF System

The 6-DOF mass matrix can be set up as (Faltinsen, 1990):

$$\mathbf{M} = \begin{bmatrix} M & 0 & 0 & 0 & Mz_G & 0 \\ 0 & M & 0 & -Mz_G & 0 & 0 \\ 0 & 0 & M & 0 & 0 & 0 \\ 0 & -Mz_G & 0 & I_{44} & 0 & -I_{46} \\ Mz_G & 0 & 0 & 0 & I_{55} & 0 \\ 0 & 0 & 0 & -I_{46} & 0 & I_{66} \end{bmatrix} \tag{6.27}$$

where I_{jj} is the moment of inertia in the j-th mode and I_{jk} is the product of inertia with respect to the coordinate system (x, y, z).

For a structure with lateral symmetry, the six coupled equations of motions can be reduced to two sets of equations, one set of three equations for surge, heave and pitch and another set of three coupled equations for sway, roll and yaw. (Faltinsen, 1990). Therefore, surge, heave and pitch are not coupled with sway, roll and yaw for a structure that possesses lateral symmetry.

For simplicity, it is assumed that the STC model possesses lateral symmetry so that the equations of motions can be simplified. Thus, the degree of freedom that concern the STC model in the study of Mathieu instability is surge, heave and pitch.

To see the effect on the heave motion on the development of Mathieu instability, the heave motion is enforced onto the structure. This means that the MATLAB code does not solve for heave as this is given as input. The code only solves for the surge and pitch motions.

For the 2-DOF system of surge and pitch, the mass matrix can be simplified to:

$$\mathbf{M} = \begin{bmatrix} M & Mz_G \\ Mz_G & I_{55} \end{bmatrix} \tag{6.28}$$

where M is the mass of the structure. Mz_G is the product of the mass of the structure and the centre of gravity and represents the coupling term between surge and pitch.

The equation of motion for the 2-DOF system is given as:

$$(\mathbf{M} + \mathbf{A}) \begin{bmatrix} \ddot{\eta}_1 \\ \ddot{\eta}_5 \end{bmatrix} + \mathbf{B} \begin{bmatrix} \dot{\eta}_1 \\ \dot{\eta}_5 \end{bmatrix} + \mathbf{K} \begin{bmatrix} \eta_1 \\ \eta_5 \end{bmatrix} = \mathbf{F} \tag{6.29}$$

where

M is the mass matrix.

A is the added mass matrix.

B is the potential damping matrix.

K is the stiffness matrix.

F is the excitation force matrix. The first line gives the force in surge and the second line gives the moment in pitch.

In order to solve the second order differential equation numerically, it is convenient to convert Eq. 6.29 into a first order differential equation. This is performed by introducing the state vector:

$$\underline{q} = \begin{bmatrix} q_1 \\ q_2 \\ q_3 \\ q_4 \end{bmatrix} = \begin{bmatrix} \eta_1 \\ \eta_5 \\ \dot{\eta}_1 \\ \dot{\eta}_5 \end{bmatrix} \tag{6.30}$$

which will result in a first order system in the form:

$$\frac{\mathrm{d}\bar{q}}{\mathrm{d}x} = \bar{f}\left(t, \bar{q}\right) \tag{6.31}$$

The derivatives of the elements in the state vector are:

$$\dot{q}_1 = q_3 = \dot{\eta}_1; \qquad \dot{q}_2 = q_4 = \dot{\eta}_5; \qquad \dot{q}_3 = \ddot{\eta}_1; \qquad \dot{q}_4 = \ddot{\eta}_5 \tag{6.32}$$

Substituting these elements in the equation of motion results in:

$$\left(\mathbf{M} + \mathbf{A}\right) \begin{bmatrix} \dot{q}_3 \\ \dot{q}_4 \end{bmatrix} + \mathbf{B} \begin{bmatrix} q_3 \\ q_4 \end{bmatrix} + \mathbf{K} \begin{bmatrix} q_1 \\ q_2 \end{bmatrix} = \mathbf{F} \tag{6.33}$$

Finally, the first order differential equation can be written as:

$$\frac{\mathrm{d}\bar{q}}{\mathrm{d}t} = \frac{\mathrm{d}}{\mathrm{d}t} \begin{bmatrix} q_1 \\ q_2 \\ q_3 \\ q_4 \end{bmatrix} = \begin{bmatrix} q_3 \\ q_4 \\ \dot{q}_3 \\ \dot{q}_4 \end{bmatrix} = \begin{bmatrix} q_3 \\ q_4 \\ \left(\mathbf{M} + \mathbf{A}\right)^{-1} \left(\mathbf{F} - \mathbf{B} \begin{bmatrix} q_3 \\ q_4 \end{bmatrix} - \mathbf{K} \begin{bmatrix} q_1 \\ q_2 \end{bmatrix} \right) \end{bmatrix} \tag{6.34}$$

It should be noted that viscous damping is then added to the system similarly as in the case of the 1-DOF system.

The stiffness matrix is made up of the hydrostatic stiffness and the stiffness contribution by the mooring lines. This is given explicitly as:

$$\mathbf{K} = \mathbf{K}_{hydro} + \mathbf{K}_{moor} \tag{6.35}$$

where

$$\mathbf{K}_{hydro} = \begin{bmatrix} 0 & 0 \\ 0 & 161.71 + \Delta K_{hydro}\left(\eta_3\right) \end{bmatrix} \tag{6.36}$$

and

$$\mathbf{K}_{moor} = \begin{bmatrix} 54.5 & -92.5 \\ -92.5 & 199.5 + \Delta K_{moor}\left(\eta_3\right) \end{bmatrix} \tag{6.37}$$

The K_{hydro} matrix has been obtained from SIMO.

For the K_{moor} matrix, K_{11} = 54.5 N/m has been calculated by finding the restoring force when an arbitrary surge is applied, without any pitch motion. $K_{15} = K_{51}$ = -92.5 N has been calculated by pitching the structure and noting how much restoring force in surge is generated. This has been verified by applying a pure surge motion and noting how much restoring moment in pitch is generated.

6.3 Modelling Viscous Drag on the STC

The viscous drag is modeled in MATLAB by discretizing the length of the spar and torus into sections, as shown in Fig. 6.2. The dots represents the middle of each section and it is through those dots that the force on each segment acts. The tower is not modeled because from the model tests, it was found that the torus is never submerged in cases where Mathieu instability is observed. The axis shown is the global axis origin which stays fixed at coordinates (0,0,0).

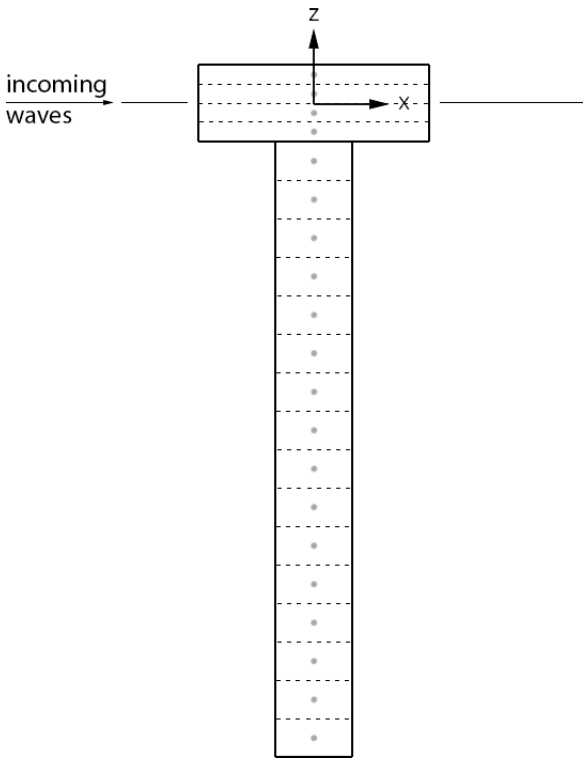

Figure 6.2: *Discretization of the STC model [Not to scale].*

It is assumed that the STC model is in deep water conditions, just like in the small scale physical model test at MARINTEK. The horizontal velocity, u_i, of the incoming waves in deep water on each segment is given by (Faltinsen, 1990):

$$u_i = \omega \zeta_a e^{kz_i} \cos(\omega t - \varphi) \tag{6.38}$$

The phase shift φ is found from the first order wave force transfer function of the 2-body SIMO model based on the hydrodynamic calculation in WADAM (Wan, 2016).

Using the Morison's equation, the drag force on each segment can be expressed as:

$$\mathrm{d}F_i = \frac{1}{2}\rho C_D D \left|(u_i - v_i)\right| (u_i - v_i)\, \mathrm{d}z_i \tag{6.39}$$

where $\mathrm{d}z_i$ is the length of each segment along the z-axis. v_i is the horizontal velocity of the segment itself. This is given as:

$$v_i = z_i \dot{\eta}_5 \tag{6.40}$$

where z_i is the vertical distance from the global axis to the centre, represented by the dots, of the segments.

The drag force induced onto the segments of the spar and torus can then be expressed as:

$$\mathrm{d}F_{spar,i} = \frac{1}{2}\rho C_D D_{spar} \left|(u_i - z_i\dot{\eta}_5)\right| (u_i - z_i\dot{\eta}_5)\, \mathrm{d}z_i \tag{6.41}$$

$$\mathrm{d}F_{torus,i} = \frac{1}{2}\rho C_D D_{torus} \left|(u_i - z_i\dot{\eta}_5)\right| (u_i - z_i\dot{\eta}_5)\, \mathrm{d}z_i \tag{6.42}$$

The value of C_D is taken as 1.2, as was used in (Wan, 2016) and is in the range of values given by the DNV standard (DNV, 2010) for such structures. This value is also representative of the drag induced onto the slender elements in the SIMO model.

The partial forces can be integrated to find the total drag force acting onto the spar and torus. This is performed numerically as follows:

$$F_{drag} = \sum_{i=1}^{n-1} \frac{\mathrm{d}F_i}{\mathrm{d}z_i} \cdot \mathrm{d}z_i + \frac{1}{2}\left(\frac{\mathrm{d}F_{i+1}}{\mathrm{d}z_i} - \frac{\mathrm{d}F_i}{\mathrm{d}z_i}\right) \cdot \cdot \mathrm{d}z_i \tag{6.43}$$

Assuming that the STC model rotates about the mean water level, the total drag moment can be computed as:

$$M_{drag} = \sum_{i=1}^{n-1} \left[\frac{\mathrm{d}F_i}{\mathrm{d}z_i} \cdot \mathrm{d}z_i + \frac{1}{2} \left(\frac{\mathrm{d}F_{i+1}}{\mathrm{d}z_i} - \frac{\mathrm{d}F_i}{\mathrm{d}z_i} \right) \cdot \cdot \mathrm{d}z_i \right] \cdot z_i \tag{6.44}$$

Therefore, the viscous drag force term in Eq. 6.26 is represented by:

$$B_{55} \left| \dot{\eta}_5 \right| \dot{\eta}_5 = M_{drag} \tag{6.45}$$

6.4 Modelling Mooring Lines

The STC prototype comprises a delta catenary mooring system, as shown in Fig. 4.1, in Chapter 4. The catenary shape and mass of the mooring lines provide nonlinear stiffness in the horizontal directions of the motions of the body while the delta lines provide yaw stiffness and damping to the STC so that large yaw motions are prevented (Wan, 2016).

In the model tests, the mooring system was represented by three rigid bars connected on the spar and three linear springs. The three linear springs provide horizontal stiffness while the rigid bars provide yaw stiffness. The mooring lines are modeled in SIMO as "fixed force elongations", which are essentially springs. A MATLAB code is written to model the mooring lines since these influence the stiffness of the system, which in turn influences the development of Mathieu instability.

When the pitch of the system changes, there is a change in length of the mooring lines which results in a force proportional to that change in length and that acts in the opposite direction, and hence, restores the system back to its original position. When the STC model is at a non-zero heave position, there is again a change in length of the mooring lines and the corresponding opposing force. However, when the system is then pitched at the non-zero heave position, the force that restores the system to its original position is different due to the non-zero heave. Thus, the stiffness of the system provided by the mooring lines changes due to the heave motion and it is important to quantify this effect and find out to which extent it influences the development of Mathieu instability.

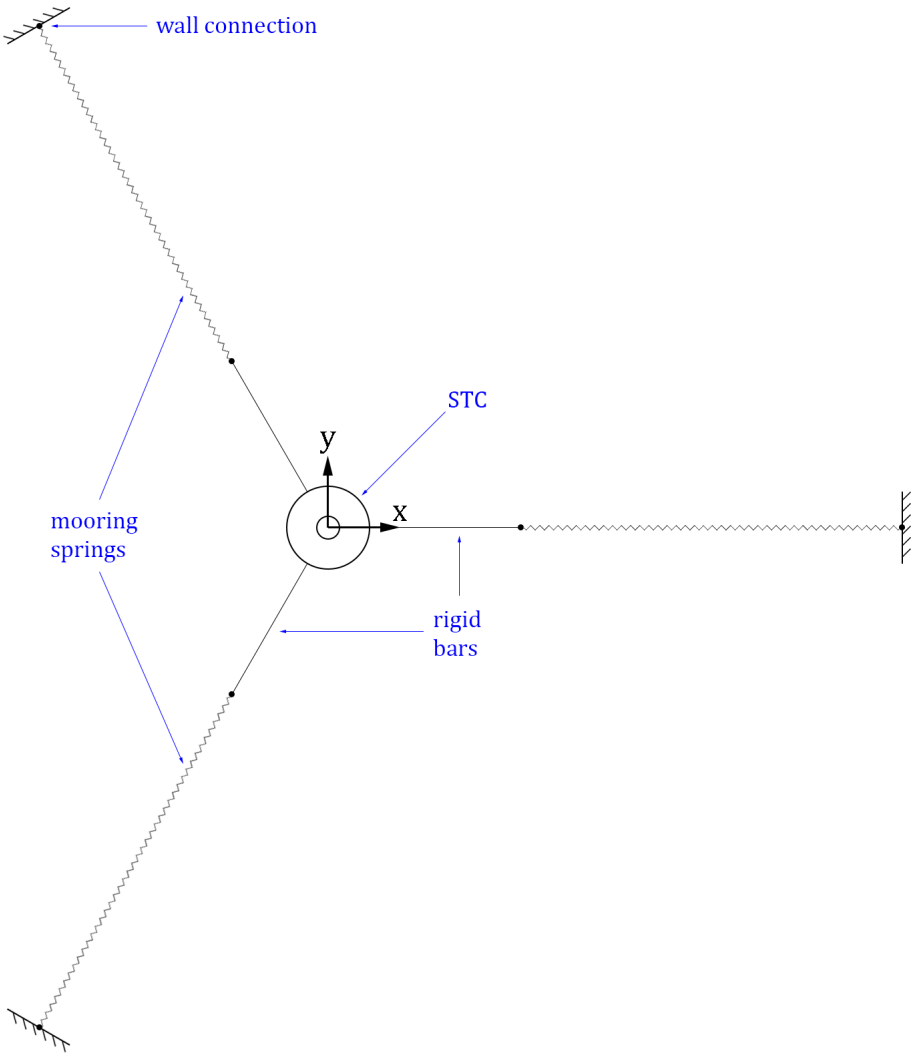

Figure 6.3: *Top view of mooring lines [Not to scale].*

The mooring system is made up of three rigid bars connected to the spar and three linear springs which connect the rigid bars to the side of the tank. A top view of the mooring system is shown in Fig. 6.3, where the z-axis points out of the plane of the page. The system has rotational symmetry of order three. At the equilibrium position, the mooring springs all have the same length. However, the stiffness of the spring which is collinear with the x-direction has a higher stiffness. There is an angle of 120° between the bars, which are of the same length. The attachments of the mooring springs to the wall and to the rigid bars are denoted by black dots.

When the system is positively pitched, one mooring spring is elongated while the two others are shortened. Fig. 6.4 shows the case when a positive pitch η_5 is applied. To simplify the diagram, the mooring lines that do not lie in the x-z plane are not shown. Moreover, heave and surge are not represented in the diagram but will be considered in the derivation of the stiffness. The colour red represents the original position and the colour blue represents the pitched position. The torus and the portion of the STC model that lies above the global axis origin is not shown. The vertical red line depicts the centre line of the spar up to the attachment of the rigid bar while the horizontal red line shows the distance between the centre of the spar and the attachment of the mooring line at the end of the rigid bar. The zigzag lines represent the mooring lines.

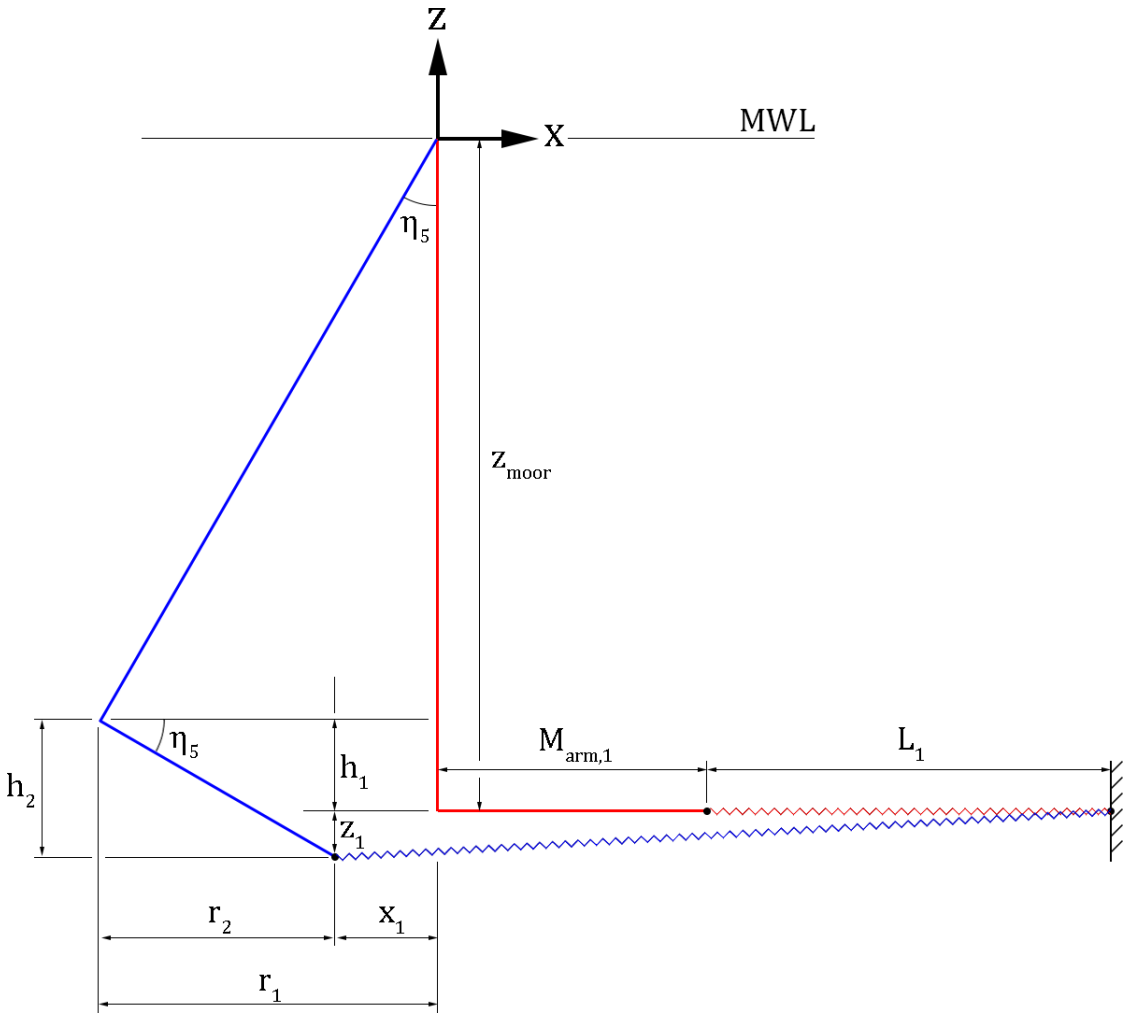

Figure 6.4: *Side view showing elongation of one mooring line [Not to scale].*

The motion of any point on a rigid body can be written as (Faltinsen, 1990):

$$\vec{s} = \eta_1\vec{i} + \eta_2\vec{j} + \eta_3\vec{k} + \vec{\omega} \times \vec{r} \tag{6.46}$$

where "x" denotes vector product and

$$\vec{\omega} = \eta_4\vec{i} + \eta_5\vec{j} + \eta_6 \tag{6.47}$$

$$\vec{r} = x\vec{i} + y\vec{j} + z\vec{k} \tag{6.48}$$

$\vec{i}, \vec{j}$ and $\vec{k}$ are unit vectors along the x-,y- and z-axis respectively. Expanding the terms results in:

$$\vec{s} = (\eta_1 + z\eta_5 - y\eta_6)\,\vec{i} + (\eta_2 - z\eta_4 + x\eta_6)\,\vec{j} + (\eta_3 + y\eta_4 - x\eta_5)\,\vec{k} \tag{6.49}$$

However, to derive the change in length of the mooring lines, the above method is not used to calculate the motion of points on the body. Instead, a trigonometric method of sines and cosines is used. These are not simplified to their small angle approximations and can be used for any given angle. Nevertheless, it is assumed that the maximum pitch angle is in the order of 10°, given that in the case of Mathieu instability, the maximum pitch angle observed in the model test was 7.3°.

When a positive pitch η_5 is applied, the mooring lines change in length. The coordinates of the point of intersection of the spar centre-line and the rigid bar change and its z-coordinate can be given by:

$$h_1 = z_{moor} \cdot (1 - \cos(\eta_5)) \tag{6.50}$$

where z_{moor} is the distance from the global axis origin to the intersection point.

The distance between the intersection point and the attachment of the mooring springs is identified as M_{arm}. The rigid bar moves with respect to the motion of the spar and the vertical change in distance can be given by:

$$h_2 = -M_{arm,1} \cdot \sin(\eta_5) \tag{6.51}$$

Therefore, the z-coordinates of the dot which connects the rigid bar to the mooring line can be expressed as:

$$z_1 = z_{moor} \cdot (1 - \cos(\eta_5)) - M_{arm,1} \cdot \sin(\eta_5) \tag{6.52}$$

If there is a heave motion η_3, the coordinates of that dot become:

$$z_1 = z_{moor} \cdot (1 - \cos(\eta_5)) - M_{arm,1} \cdot \sin(\eta_5) + \eta_3 \tag{6.53}$$

Apart from the variables h and r, the subscript "1" represents the mooring line that lies collinear with the x-direction. The subscript "2" represents the mooring line that lies outwards from the origin in the positive y-direction and the subscript "3" represents the mooring line that lies in the negative y-direction. Using the previous algebra, the z-coordinates of the other points of attachment of the bar to the mooring line can be given as:

$$z_2 = z_{moor} \cdot (1 - \cos(\eta_5)) + M_{arm,2} \cdot \cos(60°) \cdot \sin(\eta_5) + \eta_3 \tag{6.54}$$

$$z_3 = z_{moor} \cdot (1 - \cos(\eta_5)) + M_{arm,3} \cdot \cos(60°) \cdot \sin(\eta_5) + \eta_3 \tag{6.55}$$

The x-coordinate of the point of intersection of the centre-line of the spar and the rigid bar is given by:

$$r_1 = -z_{moor} \cdot \sin(\eta_5) \tag{6.56}$$

The distance r_2 as shown in Fig. 6.4 is:

$$r_2 = M_{arm,1} \cdot \cos(\eta_5) \tag{6.57}$$

Therefore, the x-coordinates of the dot which connects the rigid bar to the mooring line can be expressed as:

$$x_1 = M_{arm,1} \cdot \cos(\eta_5) - z_{moor} \cdot \sin(\eta_5) \tag{6.58}$$

In case of surge motion η_1, this becomes:

$$x_1 = M_{arm,1} \cdot \cos(\eta_5) - z_{moor} \cdot \sin(\eta_5) + \eta_1 \tag{6.59}$$

Similarly, the x-coordinates of the other points of attachment of the bar to the mooring line can be given as:

$$x_2 = -M_{arm,2} \cdot \cos(60°) \cdot \cos(\eta_5) - z_{moor} \cdot \sin(\eta_5) + \eta_1 \tag{6.60}$$

$$x_3 = -M_{arm,3} \cdot \cos(60°) \cdot \cos(\eta_5) - z_{moor} \cdot \sin(\eta_5) + \eta_1 \tag{6.61}$$

Given that the distance between the global axis origin and the side of the tank to which the mooring lines are connected is referred as L_{wall}, the new length of the first mooring line can be given as:

$$L_{new,1} = \sqrt{\left((L_{wall} - x_1)^2 + z_1^2\right)} \tag{6.62}$$

Accounting for the fact that the other two mooring lines are at an angle with respect to the x-direction, the new length of the other two mooring lines can be given as:

$$L_{new,2} = \sqrt{\left((-L_{wall} \cdot \cos(60) - x_2)^2 + (L_2 \cdot \sin(60))^2 + z_2^2\right)} \tag{6.63}$$

$$L_{new,3} = \sqrt{\left((-L_{wall} \cdot \cos(60) - x_3)^2 + (L_3 \cdot \sin(60))^2 + z_3^2\right)} \tag{6.64}$$

It can be seen that there are two terms in the new length of the first mooring line whereas there are three terms in the new length in the other mooring lines. This is because the first mooring line only lies in the xz-plane whereas the other two mooring lines are in three dimensions.

Once the new length of the mooring lines are known, it is possible to calculate their change in length. This is given as:

$$\Delta L_1 = L_{new,1} - L_1 \tag{6.65}$$

$$\Delta L_2 = L_2 - L_{new,2} \tag{6.66}$$

$$\Delta L_3 = L_3 - L_{new,3} \tag{6.67}$$

Given the change in length ΔL, the restoring force is calculated in the form:

$$F_{res} = k_{moor} \cdot \Delta L \tag{6.68}$$

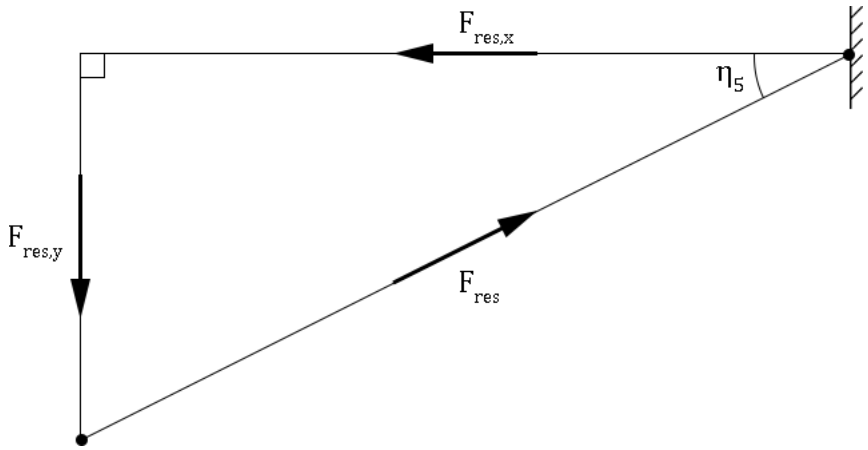

Figure 6.5: *Decomposition of the resultant forces in the mooring line.*

Using Fig. 6.5, the horizontal and vertical components of the resultant force in the mooring line are:

$$F_{res,x} = F_{res} \cos(\eta_5) = F_{res} \cdot \frac{L_{wall} - x}{L_{new}} \tag{6.69}$$

$$F_{res,z} = F_{res} \sin(\eta_5) = F_{res} \cdot \frac{z}{L_{new}} \tag{6.70}$$

Therefore, the horizontal components in all the mooring springs are given by:

$$F_{res,1x} = k_{moor,1} \cdot \Delta L_1 \cdot \frac{L_{wall} - x_1}{L_{new,1}} \tag{6.71}$$

$$F_{res,2x} = k_{moor,2} \cdot \Delta L_2 \cdot \frac{(L_{wall} \cdot \cos(60)) - x_2}{L_{new,2}} \tag{6.72}$$

$$F_{res,3x} = k_{moor,3} \cdot \Delta L_3 \cdot \frac{(L_{wall} \cdot \cos(60)) - x_3}{L_{new,3}} \tag{6.73}$$

The vertical components in all the mooring springs are given by:

$$F_{res,1z} = k_{moor,1} \cdot \Delta L_1 \cdot \frac{z_1}{L_{new,1}} \tag{6.74}$$

$$F_{res,2z} = -k_{moor,2} \cdot \Delta L_2 \cdot \frac{z_2}{L_{new,2}} \tag{6.75}$$

$$F_{res,3z} = -k_{moor,3} \cdot \Delta L_3 \cdot \frac{z_3}{L_{new,3}} \tag{6.76}$$

It is the possible to calculate the restoring pitch moments due to the vertical components of the mooring spring forces as follows:

$$M_{res,iz} = F_{res,iz} \cdot x_i \qquad \text{for } i = 1, 2, 3 \tag{6.77}$$

Assuming that the centre of rotation stays at the mean water level, the restoring pitch moments due to the horizontal components of the mooring spring forces are:

$$M_{res,ix} = F_{res,ix} \cdot (z_{moor} - z_i) \qquad \text{for } i = 1, 2, 3 \tag{6.78}$$

The total force provided by the mooring lines in the x-direction is given by:

$$F_{moor} = \sum_{i=1}^{3} F_{res,ix} \tag{6.79}$$

The total pitch restoring moment provided by the mooring lines is given by:

$$M_{moor} = \sum_{i=1}^{3} M_{res,ix} + \sum_{i=1}^{3} M_{res,iz} \tag{6.80}$$

6.5 Mooring Line Stiffness as a Function of Heave

In principle, the stiffness of the system provided by the mooring lines should not be dependent on the pitch, which means it should be a constant even though pitch changes. However, when this was analyzed, it was found that the stiffness was influenced by pitch, even more than by heave.

Using the trigonometric method as detailed in the previous section, an arbitrary pitch is applied to the system and the corresponding restoring moment can be calculated. Instead of calculating the stiffness by dividing the restoring moment by the pitch angle, the stiffness is calculated by finding the gradient of the curve of the restoring moment at different pitch.

For example, the stiffness at a pitch angle of $\eta_5 = 5°$ is calculated by dividing the change in restoring moment by the change in pitch angle over the range 4.99° and 5.01°. This means the small curvature of the restoring moment curve can be taken into account.

Based on the SIMO model provided by Dr. Ling Wan, the stiffness of the mooring line/spring which is collinear with the x-axis (referred to as mooring line 1) is set at 25 N/m and the stiffness of the remaining two mooring lines (referred to as mooring lines 2 and 3) is set at 29.5 N/m. The force exerted in the mooring lines is a linear function of the change in length of the mooring lines. However, this change in length is not a linear function of pitch due to the motion of the body in the xz-plane. The change in length due to varying pitch is plotted as shown in Fig. 6.6.

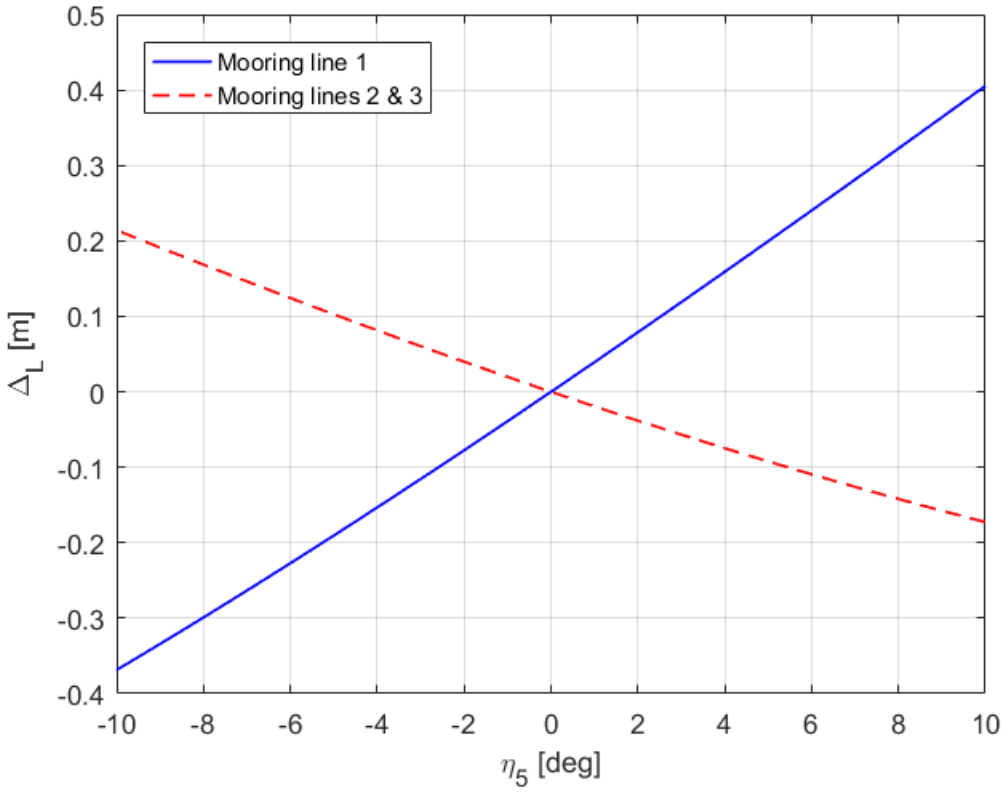

Figure 6.6: *Change in length of mooring lines in the model test as a function of pitch motion. No heave motion.*

A positive pitch causes the first mooring spring to elongate while the other two mooring spring to shorten. The curve is found to be almost linear. It should also be noted that a positive pitch does not result in the same change in length as a negative pitch because of the geometry of the structure and mooring lines. This is because the mooring lines are not connected directly to the centre-line of the spar but are instead connected to the rigid bars. Moreover, the connection point between the mooring lines and the rigid bar moves in an arc, as the structure is pitched, as opposed to moving in a straight line.

After the displacements are found, it is possible to calculate the force that is generated in the mooring lines. These forces are then separated into their x- and y-components and the restoring moments can then be calculated. It is assumed that the centre of rotation of the structure is always at the mean water level. The restoring moment as a function of pitch is shown in Fig.6.7. Once more the curve is found to be almost linear.

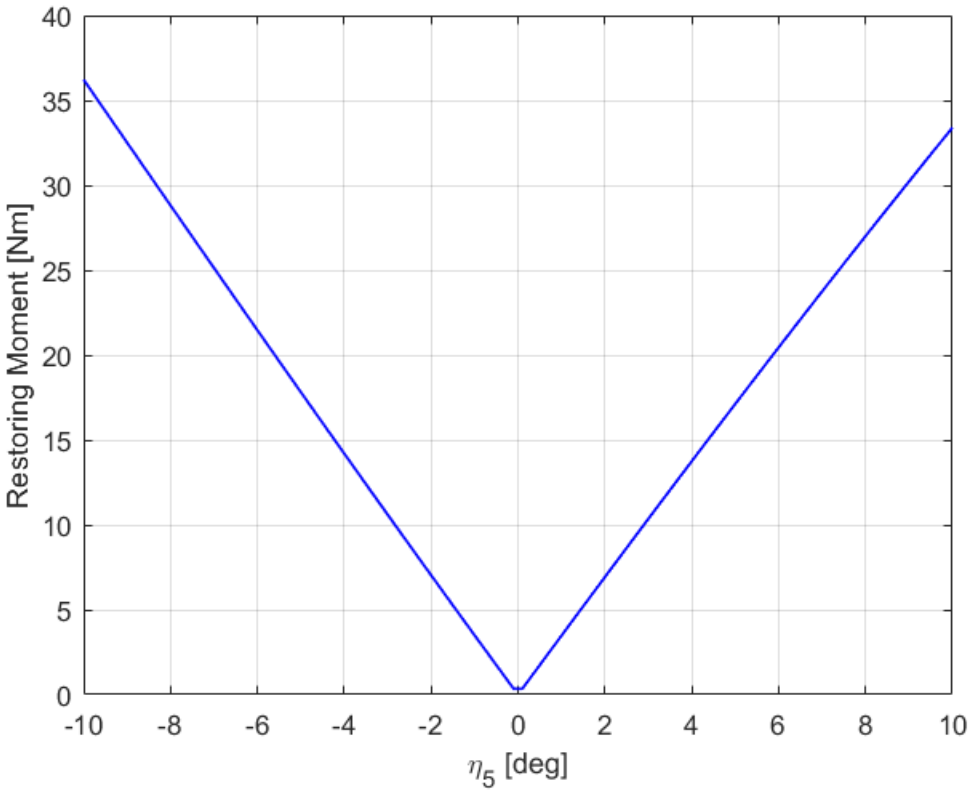

Figure 6.7: *Pitch restoring moment as a function of pitch motion. No heave motion.*

Finally, the stiffness of the system provided by the mooring lines can be calculated using the discussed method. The stiffness as a function of pitch is plotted in Fig. 6.8.

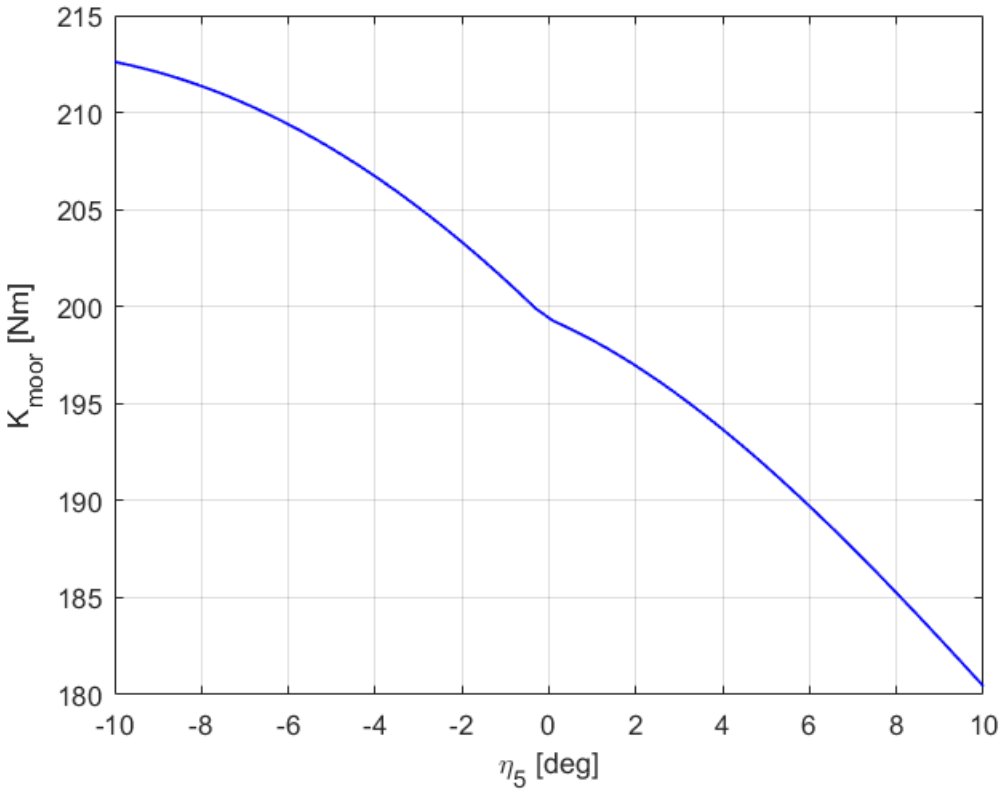

Figure 6.8: *Stiffness contribution of mooring lines as a function of pitch motion. No heave motion.*

It is found that the stiffness of the system does vary with pitch. This can be explained as follows: the stiffness of the mooring lines themselves remain constant at all times and the mooring force varies linearly with the change in length of the mooring lines. However, that change in length does not vary linearly with pitch which results in the restoring moment not varying linearly with pitch. These differences are small until the stiffness of the system due to mooring lines is calculated by dividing the change in restoring moment by the change in pitch. The pitch in radians is approximately in the range -0.17 to 0.17 (corresponding to -10 to 10 degrees) and dividing the restoring moment by a small number makes the differences more apparent at this stage in the calculations.

It was found that the stiffness of the system is about 199.5 Nm/rad with a variation of about ±7% over the pitch domain from -10 to 10 degrees depending on whether the pitch is positive or negative. If the maximum pitch is limited to 7.3 degrees, as found from the small scale model tests, the variation in stiffness is in the order of ±6% about the mean value.

Fig. 6.9 shows the stiffness of the system as a function of heave (model scale). An arbitrary pitch (-7.5°,-5°, -2.5°, 2.5°,5°,7.5°) is applied to the structure and the heave is then varied. The stiffness is again calculated by dividing the change in restoring moment by the change in pitch.

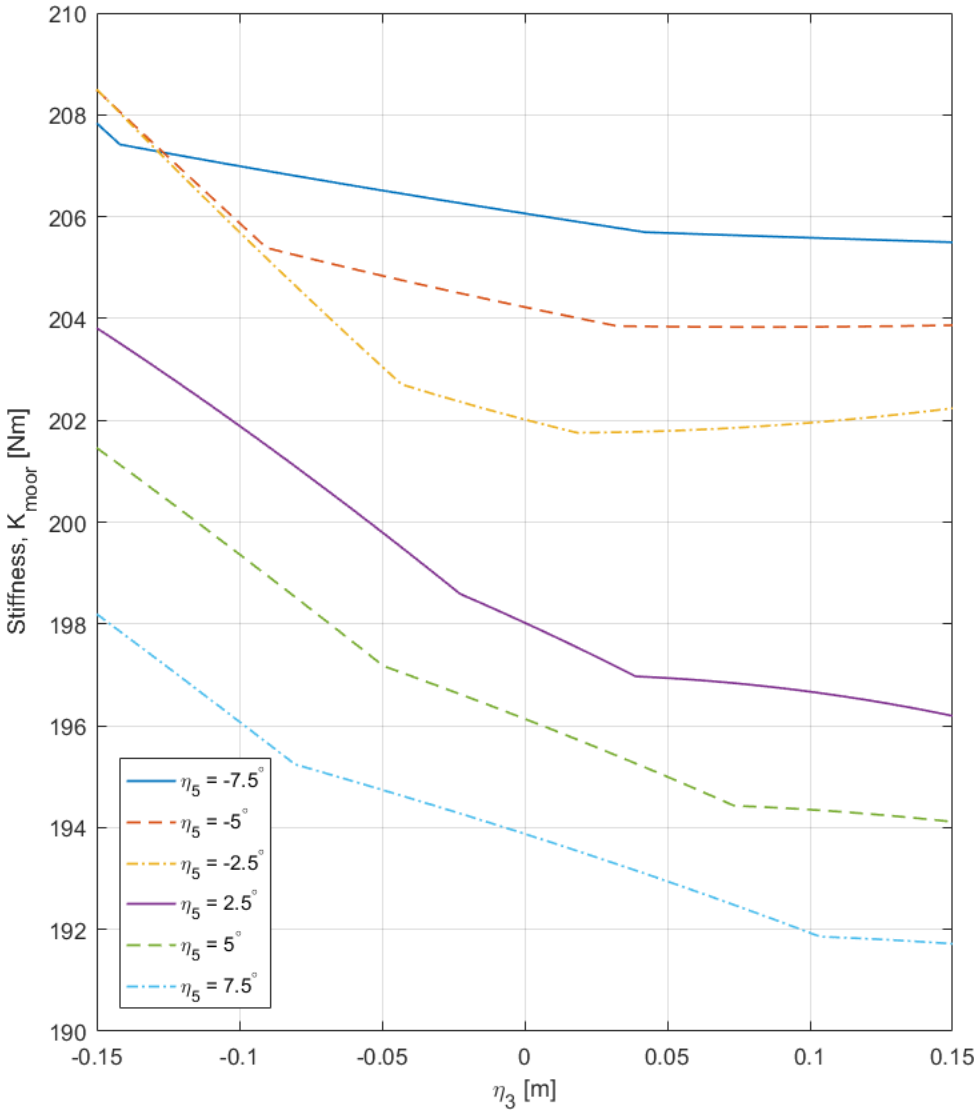

Figure 6.9: *Stiffness contribution of mooring lines as a function of heave motion.*

It can be found from Fig. 6.9 that the stiffness is different for different pitch angles, as previously observed. Moreover, the variation of stiffness with heave is slightly different depending on whether the pitch is positive or negative.

To get insight into the variation of stiffness, it is important to understand the relative contribution of heave and pitch to the stiffness of the system. The heave is varied over a range of (-0.15 to 0.15 metres) and the pitch is varied over a range of (-15 to 15 degrees). Then, a 3D-plot of the stiffness as a function of both heave and pitch is plotted, as shown in Fig. 6.10.

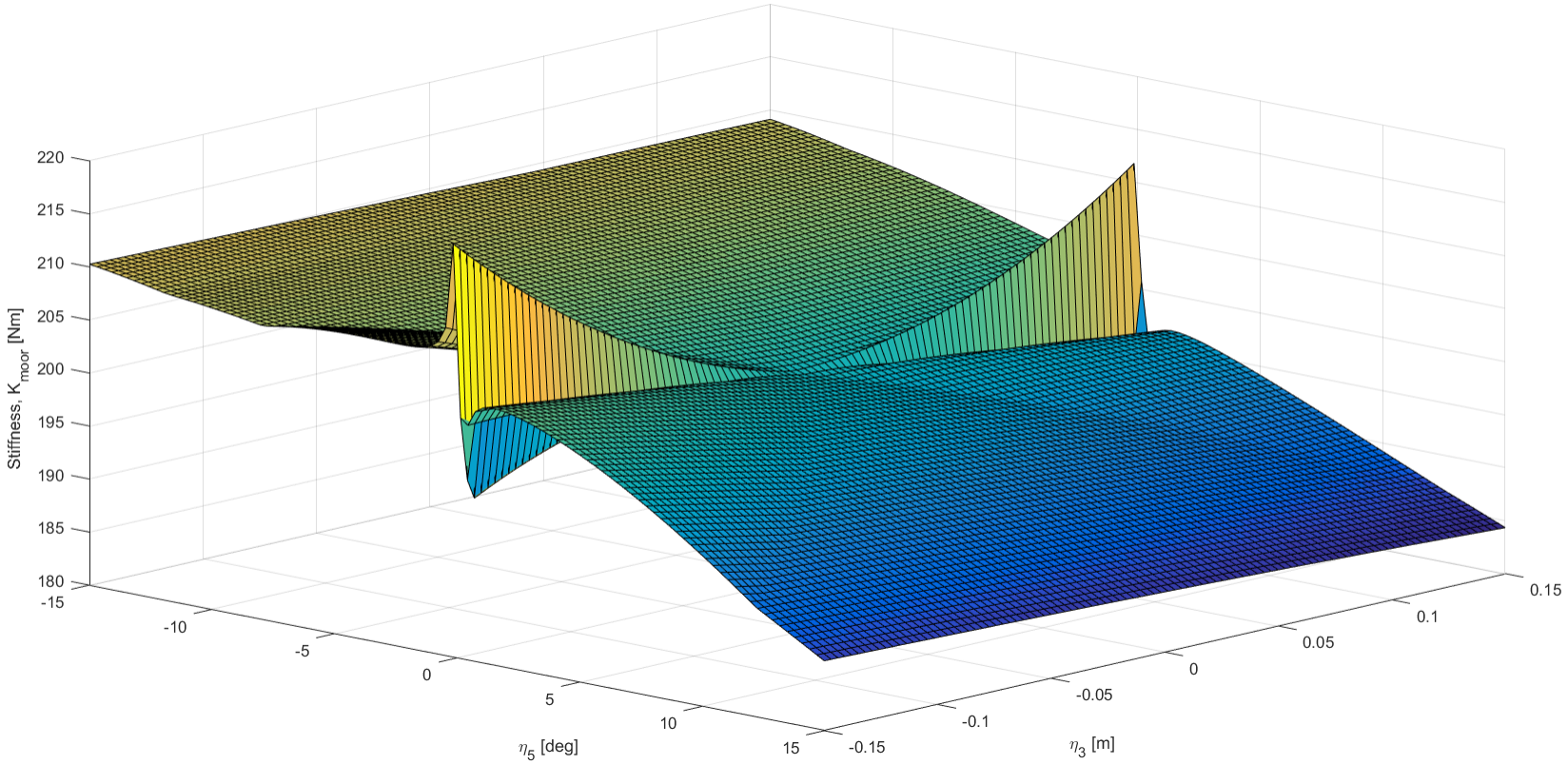

Figure 6.10: *Stiffness contribution of the mooring lines as a function of both heave and pitch (model scale).*

It can be found from Fig. 6.10 that the stiffness is influenced more by the change in pitch rather than the change in heave. The peaks close to zero pitch angles occur because the change in restoring moment is divided by the change in pitch angles, which have very small values.

It is equally important to know the relative contribution of hydrostatic forces and mooring lines to the total stiffness of the system. This is plotted as shown in Fig. 6.10. The dotted black line represents the variation of the stiffness provided by the hydrostatic forces with respect to heave motion, referred to as K_{hydro}.

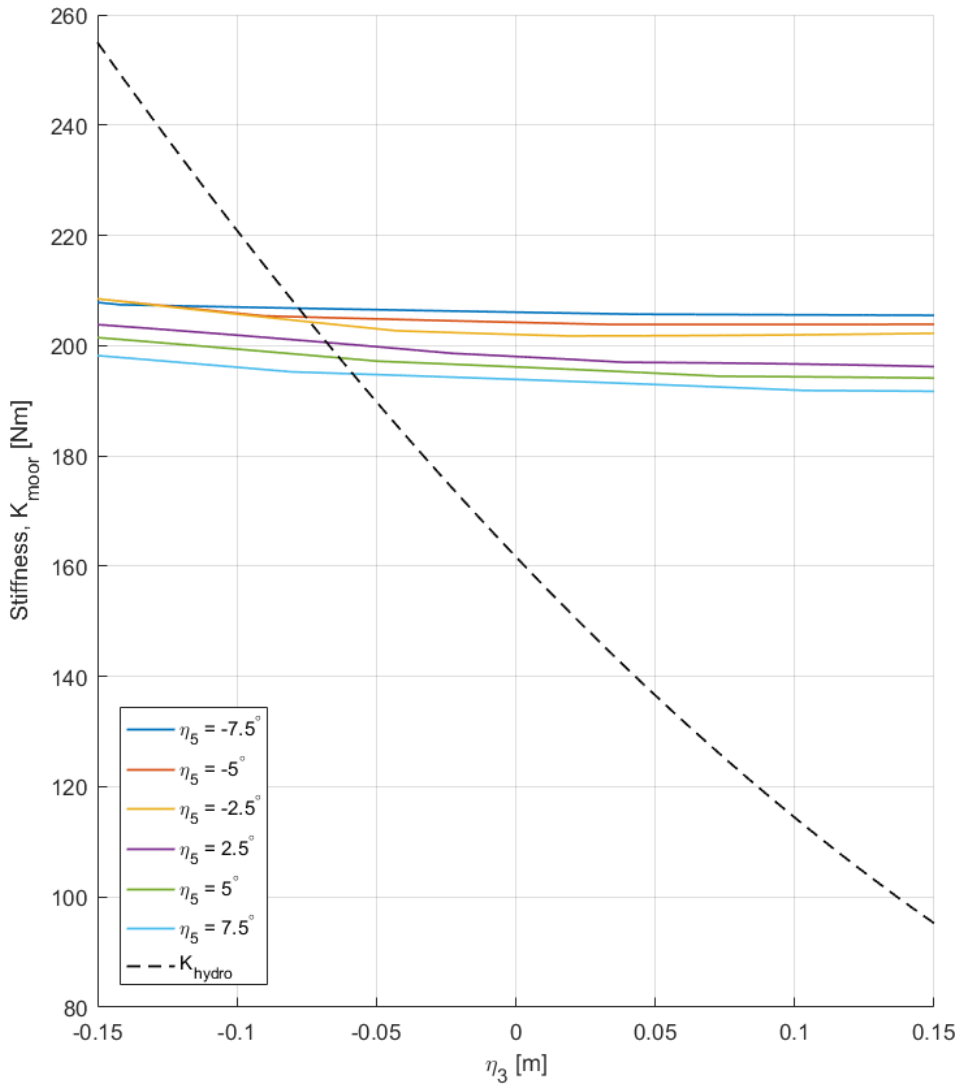

Figure 6.11: *Stiffness as a function of heave (model scale).*

It can be found from Fig. 6.11 that when there is no heave ($\eta_3 = 0m$), the stiff-

ness contributed by the mooring lines is in the order of 200 Nm whereas the stiffness contributed by the hydrostatic forces is in the order of 160 Nm. However, despite contribution by the hydrostatic forces being less than that of the mooring lines, the variation of stiffness due to the hydrostatic forces is far more that that of the mooring lines.

Quantitatively, the variation of stiffness as a function of heave from the respective contributions can be approximated as:

$$K_{hydro}\left(\eta_3\right) = 160 \pm 50\% \tag{6.81}$$

$$K_{moor}\left(\eta_3\right) = 200 \pm 2\% \tag{6.82}$$

From the 1-body STC model provided by Dr. Ling Wan, the hydrostatic stiffness is found to be $K_{hydro,0} = 161.71Nm$. The WADAM1.LIS, which corresponds to the analysis of the 1-body STC concept in HydroD, mentions a stiffness, including mooring lines, of 376.198 Nm. This implies that the stiffness provided only by the mooring lines is $K_{moor,0} = 214.49Nm$, which is about 7.5% higher than the value which was computed using the trigonometric method.

To summarize, the contributions to the stiffness of the system is given by

$$K_{55}\left(\eta_3\right) = K_{hydro}\left(\eta_3\right) + K_{moor}\left(\eta_3\right) \tag{6.83}$$

where the hydrostatic stiffness as a function of heave is found as (Koo et al., 2004):

$$K_{hydro}\left(\eta_3\right) = K_{hydro,0} - \frac{1}{2}\rho g\left(\nabla + 2A_w\overline{GM}\right)\eta_3\left(t\right) + \frac{1}{2}\rho g A_w\left(\eta_3\left(t\right)\right)^2 \tag{6.84}$$

and the stiffness as a function of heave contributed by the mooring lines, as estimated from the MATLAB, can be given by:

$$K_{moor}\left(\eta_3\right) = K_{moor,0} - 16 \cdot \eta_3\left(t\right) \tag{6.85}$$

Alternatively, the stiffness of the system as a function of heave can be calculated as:

$$K_{55}\left(\eta_3\right) = 376.198 + \Delta K_{hydro}\left(\eta_3\right) + \Delta K_{moor}\left(\eta_3\right) \tag{6.86}$$

It is straightforward to find $K_{hydro} = f(\eta_3)$. It was also intended to find $K_{moor} = f(\eta_3)$ but it is hard to neglect the influence of pitch and thus, the stiffness provided by the mooring lines is more accurately $K_{moor} = f(\eta_3, \eta_5)$. However, since the variation of K_{moor} as a function of pitch is still much lower than the variation of K_{hydro} as a function of heave, K_{moor} can be represented without significant loss in accuracy by Eq. 6.85.

Chapter 7

Numerical Results of the 1- and 2-DOF Systems

The STC concept is modelled in MATLAB, first as a 1-DOF system in pitch only and then as a 2-DOF system that accounts for the coupling in surge-pitch. This chapter focuses on the tests that were performed on the two MATLAB models and the results obtained. All the results are presented at model scale unless otherwise specified.

7.1 1-DOF Model

The 1-DOF system was modelled using Eq. 6.26. The equation is solved using constant terms and without the retardation function, that is, the frequency dependent added mass and damping are taken at a frequency equal to half the pitch natural frequency. These values are taken from the 1-body model in SIMO, which contains the frequency dependent added mass and damping as shown respectively in Fig. 7.1 and Fig. 7.2. Then, it is possible to run a number of tests on the 1-DOF system.

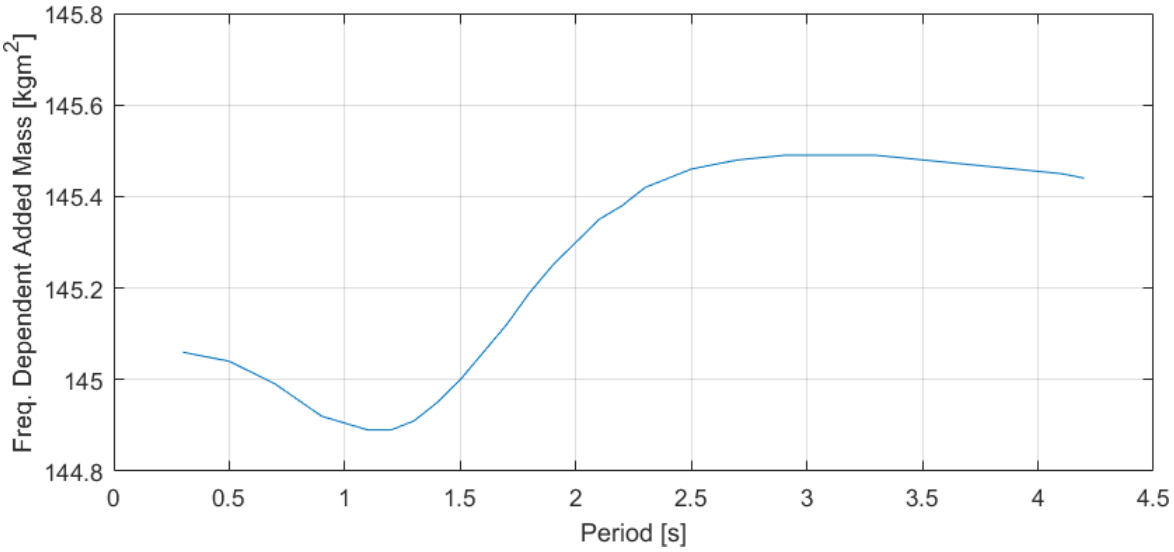

Figure 7.1: *Frequency dependent added mass in the pitch-pitch degree of freedom (model scale).*

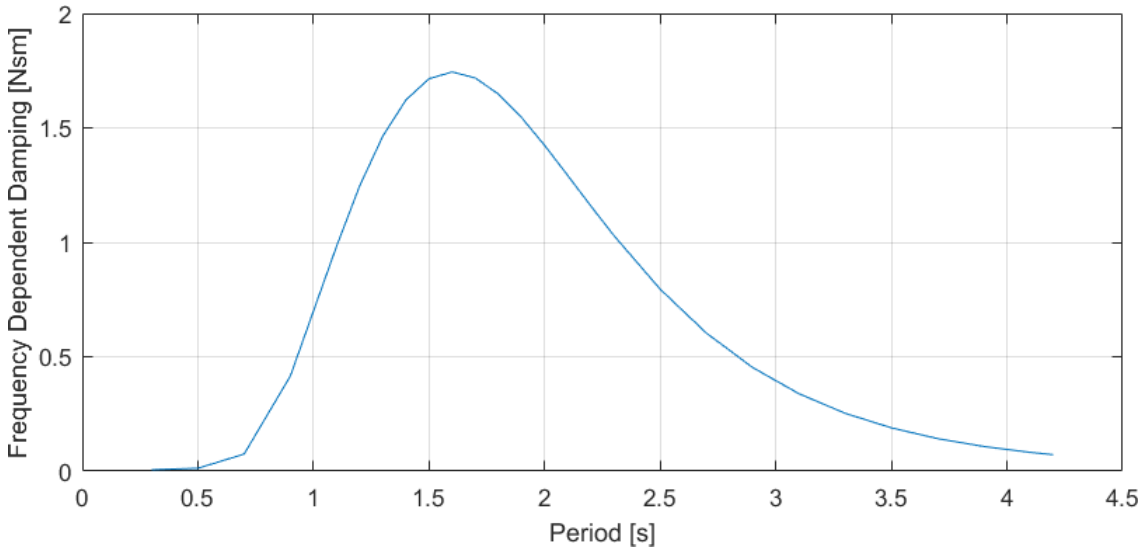

Figure 7.2: *Frequency dependent damping in the pitch-pitch degree of freedom (model scale).*

7.1.1 Decay Test

A decay test is performed to identify the natural period in pitch as well as the damping ratio. This implies solving the second order differential equation in MATLAB using an initial pitch value set at 8 degrees. The decay test is shown in Fig. 7.3.

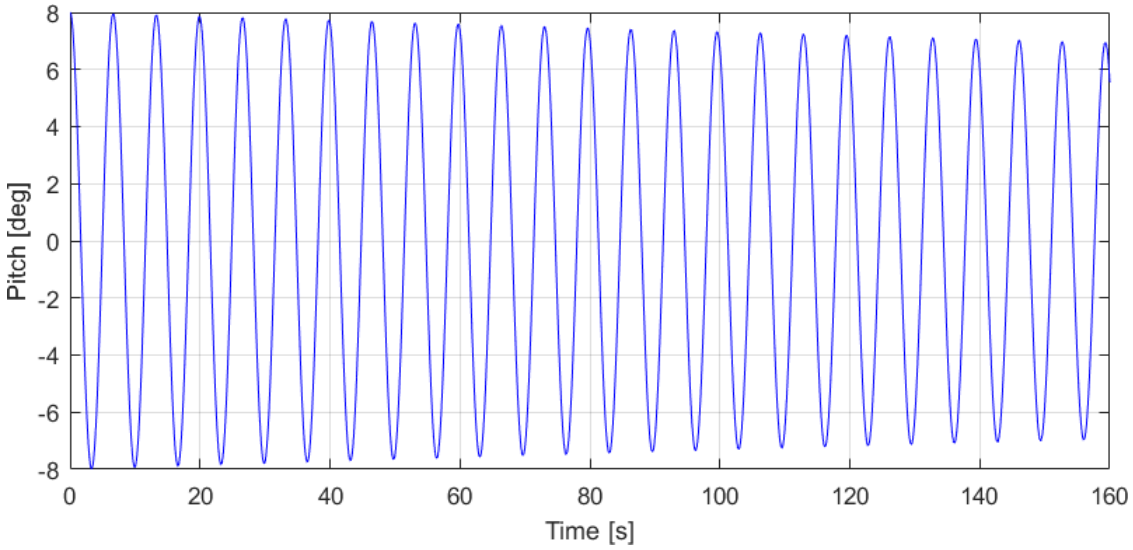

Figure 7.3: *Decay test of the 1-DOF system without viscous damping (model scale).*

The identified natural period in pitch is found to be 6.64 s (46.95 s in full scale). It should be noted that viscous damping is not considered so that its effects can be compared next. Only potential damping is considered and it can be seen from 7.3, that the decay is very slow due to the small potential damping level. Using 8 peaks, the damping ratio is found to be about 3%.

The natural pitch period can also be calculated, using the following equation, assuming the system is undamped. It is found from Eq. 7.1 that the natural pitch period is 6.64 s, which is exactly what was obtained from the decay test.

$$T = 2\pi\sqrt{\frac{(I_{55} + A_{55})}{K_{55}}} \tag{7.1}$$

Then, viscous damping, as was modelled in Section 6.3, is added to the system. A decay test is run and the result is shown in Fig. 7.4.

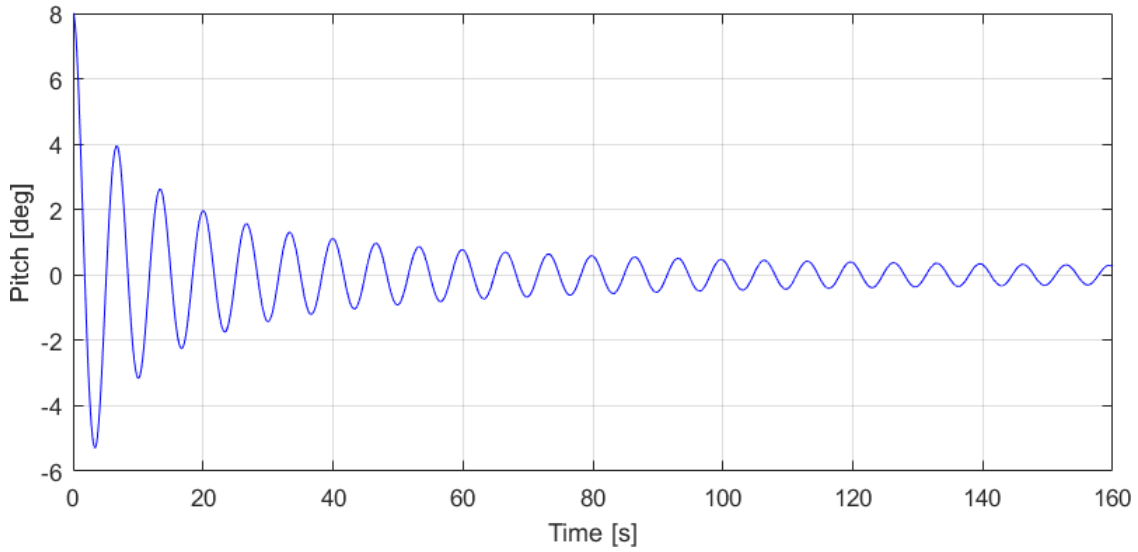

Figure 7.4: *Decay test of the 1-DOF system including viscous damping (model scale).*

Viscous damping is more significant when the pitch motion is large whereas potential damping is more important for small pitch motions. It can be seen from Fig. 7.4 that the decay is now faster, especially at the beginning when the pitch motion is large.

7.1.2 External Excitation

The 1-DOF system is forced to heave at a period equal to half the pitch natural period. No external excitation forces are included, that is, the right hand side of Eq. 6.26 is set to zero. A small initial pitch (0.1 degrees) is applied and a test is then performed, shown in Fig. 7.5 to identify how the system behaves when its stiffness changes due to the heave motion.

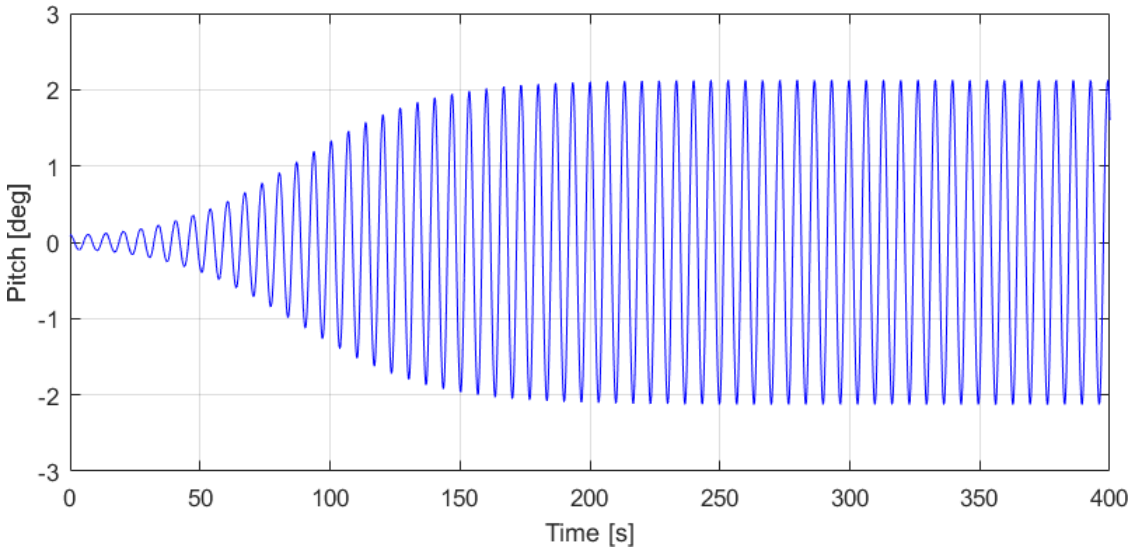

Figure 7.5: *Decay test of the 1-DOF system with enforced heave motion of amplitude 0.12m (model scale).*

It can be seen that the pitch slowly increases until it reaches a constant maximum value of about 2.2 degrees. If viscous damping were not included, the pitch motion would not be restrained and would increase to infinity. Viscous damping increases as the pitch motion increases and this limits the maximum pitch motion.

Moreover, Fig. 7.5 includes the change in hydrostatic stiffness as well as the change in the stiffness contributed by the mooring lines. If the hydrostatic stiffness would not be allowed to vary with the heave motion, the test would be similar to the decay tests previously performed as the stiffness parameter of the system is a constant.

If only the stiffness contributed by the mooring lines were allowed to vary with the heave motion, the result would still be similar to the decay tests as the stiffness change is not large enough to induce self-excitation. The only visible change in the result would be a very small decrease (in the order of a few percent) in the rate of decay.

Finally, together with the enforced heave motion, an external force in pitch, with a period equal to half the pitch natural period, is added to the 1-DOF system. The amplitude of the force as well as its phase difference are taken from the 1-body SIMO model. A small initial pitch (0.1 degrees) is applied to the system and the equation of motion is solved.

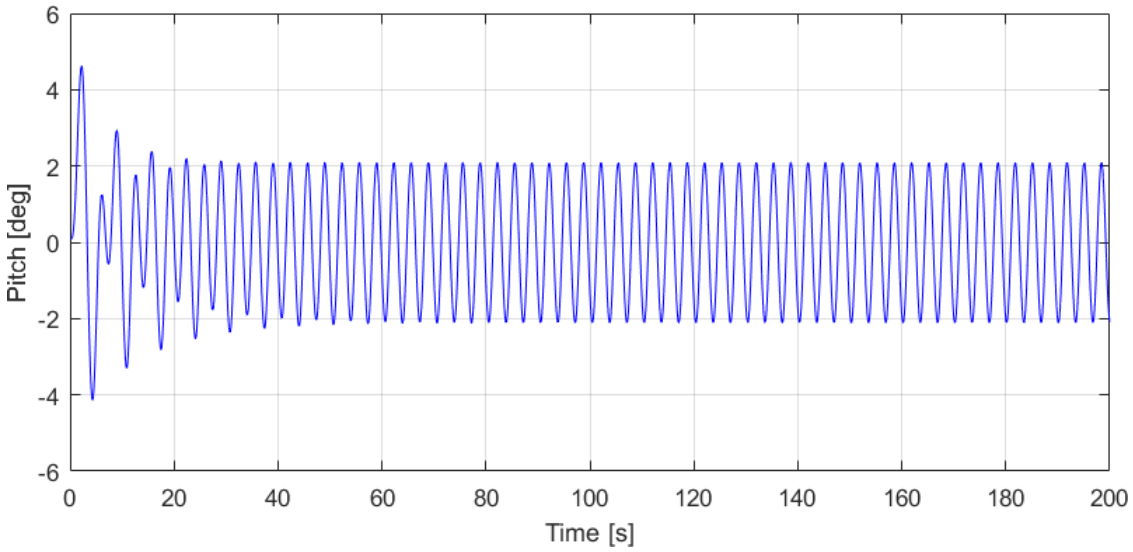

Figure 7.6: *Decay test of the 1-DOF system with enforced heave motion and external force excitation in pitch (model scale).*

Fig. 7.6 shows the result obtained when an external force excitation in pitch as well as a periodic heave motion is applied to the system. The initial transient shows a pitch motion with a period equal to the pitch natural period but period of the pitch motion changes over a few cycles to the period of the external force excitation. No Mathieu instability is observed.

It should be noted that in all the tests performed, the drag coefficient (C_D) is taken to be 1.2, similar to what was used by Dr. Ling Wan in his thesis work. If the C_D is increased the pitch motion changes more rapidly to the external force excitation frequency but Mathieu instability is still not observed. If the C_D is decreased to its lowest value as per the $DNV - RP - C205$ codes (DNV, 2010), the change of pitch period to the pitch natural period is slower, as shown in Fig. 7.7.

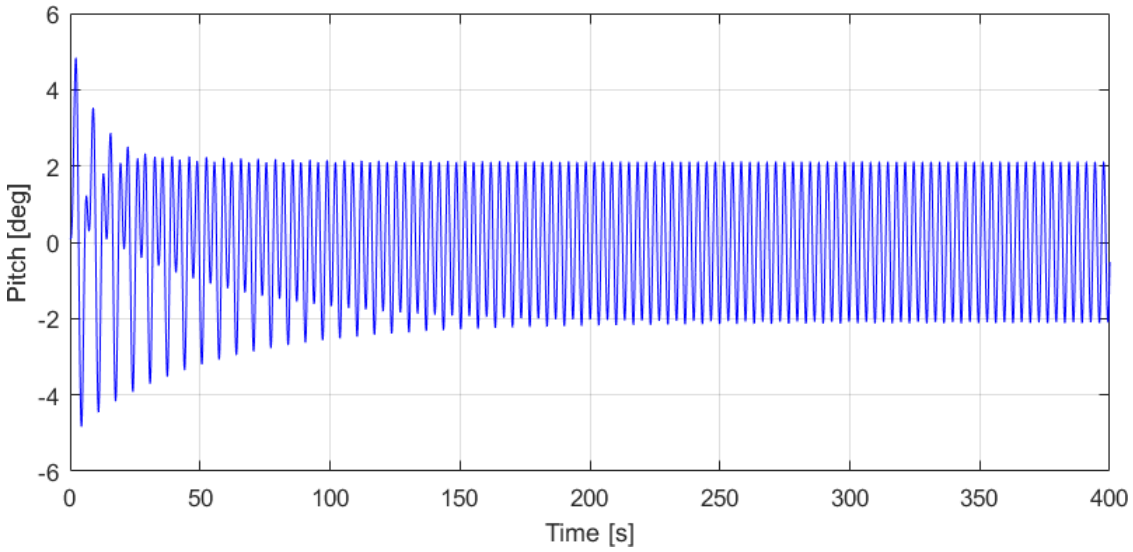

Figure 7.7: *Decay test of the 1-DOF system with enforced heave motion and external force excitation in pitch (model scale).* $C_D = 0.65$.

7.2 2-DOF Model

This section describes the tests and results obtained when the coupling in surge-pitch is taken into account using the approach explained in section 6.2. Moreover, the frequency dependent added mass and damping in the surge-surge, surge-pitch and pitch-surge degrees of freedom are all taken from the SIMO 1-body model.

7.2.1 Decay Test

A decay test is performed to identify the natural period in pitch as well as the damping ratio. An initial pitch of 8 degrees is applied and the differential equation is solved. The result without viscous damping is shown in Fig. 7.8.

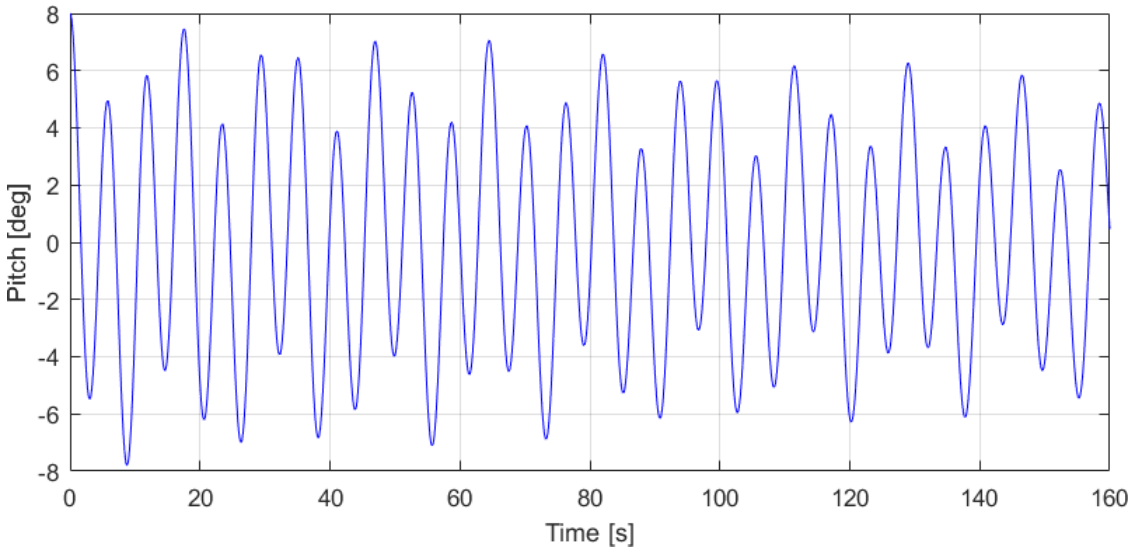

Figure 7.8: *Decay test of the 2-DOF system without viscous damping (model scale).*

The identified natural period in pitch is found to be 5.86 s (41.44 s in full scale). It can be seen that the decay is not monotonous because of the surge-pitch coupling. Moreover, it the decay is very slow because only potential damping is considered at this stage. The damping ratio was found to be approximately 2.8% but there was some variation due to the decay not being monotonous.

It is also possible to calculate the natural period in pitch using eigenvalue analysis. From the eigenvalue analysis, it is found that the pitch natural period is equal to 5.86 seconds (41.44 s in full scale), which is exactly what was obtained in the decay test.

Viscous damping is added, a decay test is run and the result is shown in Fig. 7.9.

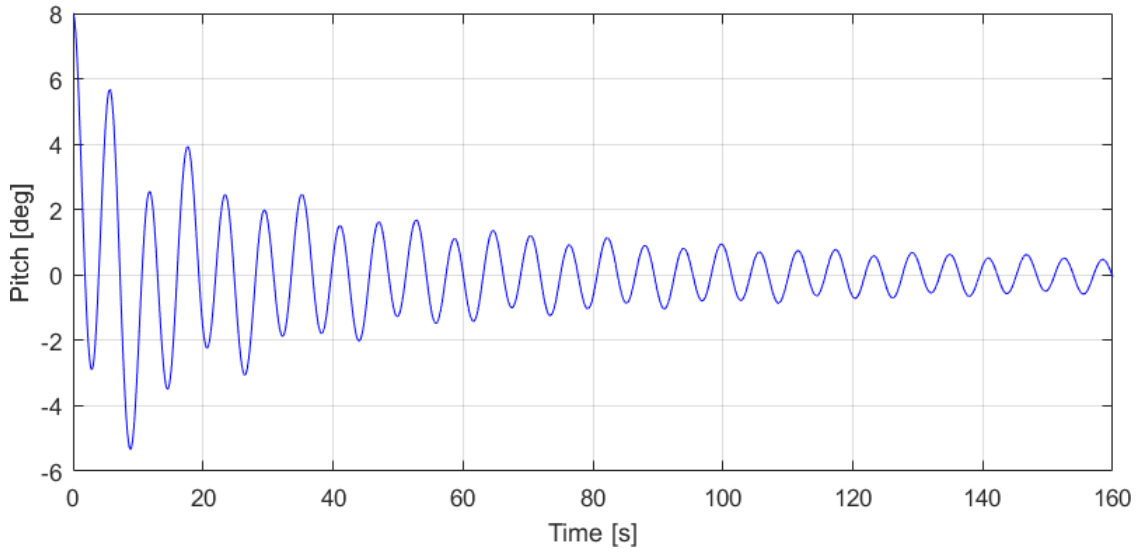

Figure 7.9: *Decay test of the 2-DOF system including viscous damping (model scale).*

When viscous damping is added, the decay is much faster especially at the beginning when the pitch motion is high. However, because of the surge-pitch coupling, the decay is not monotonous. An initial surge was also added to the system but it was difficult to obtain a monotonous decay in pitch.

7.2.2 External Excitation

The 2-DOF system is forced to heave at a period equal to half the pitch natural period. No external excitation forces are included. A small initial pitch (0.1 degrees) is applied and a test is then performed, shown in Fig. 7.10 to identify how the system behaves when its stiffness changes due to the heave motion.

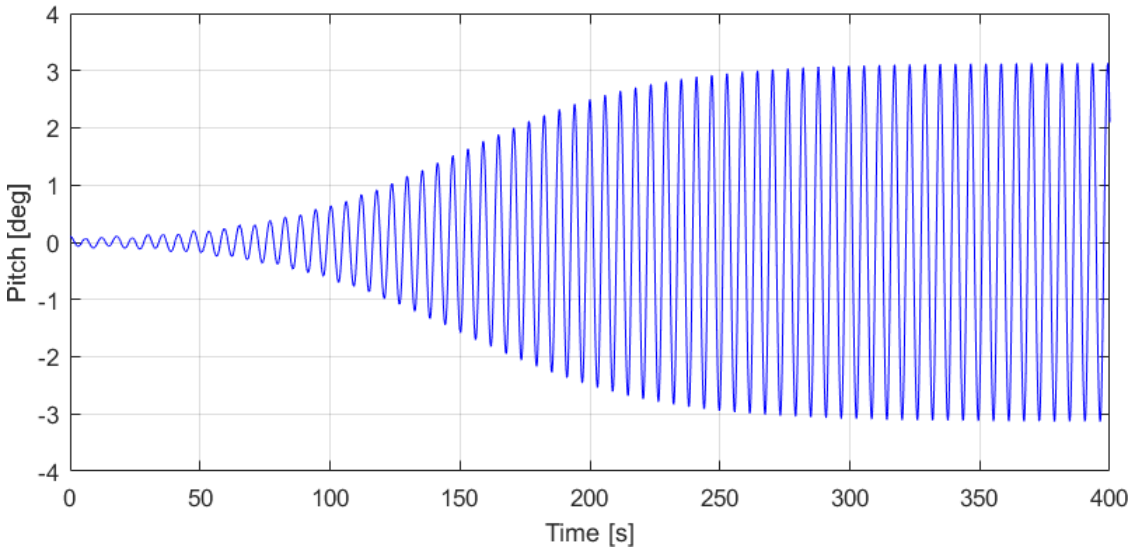

Figure 7.10: *Decay test of the 2-DOF system with enforced heave motion (model scale).*

It can be seen that the pitch slowly increases until it reaches a constant maximum value of about 3.2 degrees, which is higher than what was obtained in the 1-DOF model. Moreover, it takes longer for the 2-DOF model to reach its steady state phase as compared with the 1-DOF model. It should be noted that for both models, no self-excitation occurs when the hydrostatic stiffness is not allowed to vary with the heave motion.

Together with the enforced heave motion, external forces in surge and pitch, with a period equal to half the pitch natural period, is added to the 2-DOF system. The amplitude of these forces as well as their phase difference are taken from the 1-body SIMO model. A small initial pitch (0.1 degrees) is applied to the system and the equation of motion is then solved.

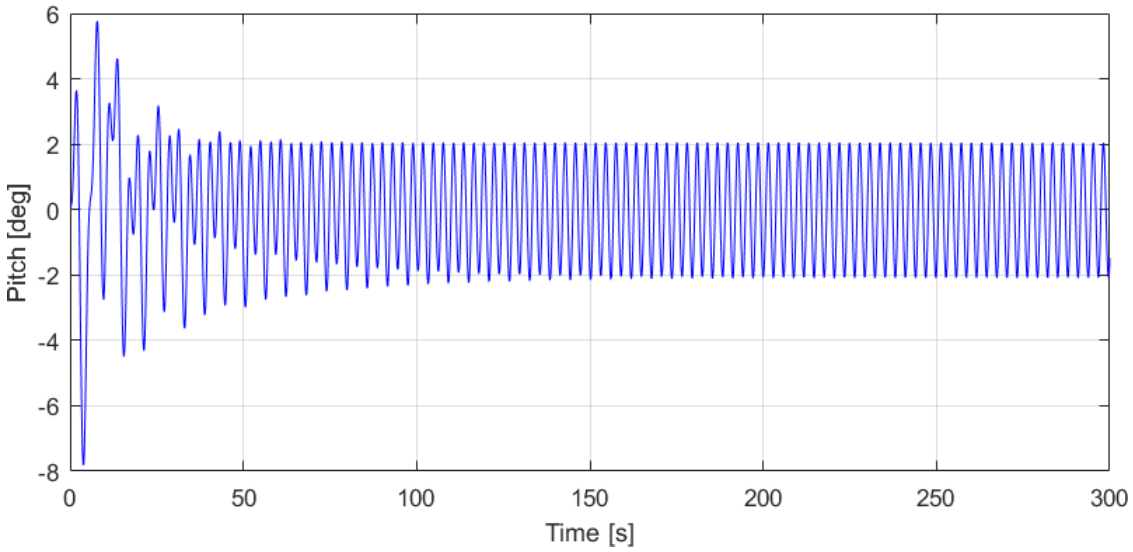

Figure 7.11: *Decay test of the 2-DOF system with enforced heave motion and external force excitation in pitch (model scale).*

Fig. 7.11 shows the result obtained when external force excitations in surge and pitch as well as a periodic heave motion are applied to the system. The initial transient shows a pitch motion with a period equal to the pitch natural period but period of the pitch motion changes to the period of the external force excitation. No Mathieu instability is observed.

The pitch natural period and the damping ratio for both MATLAB models are summarized in the following table :

Table 7.1: *Comparison of pitch natural period and damping ratio.*

Model	T_N (full scale)	T_N (model scale)	Damping Ratio
1-DOF	49.95 s	6.64 s	3%
2-DOF	41.44s	5.86 s	2.8%

Chapter 8

Comparisons of Experimental and Numerical Results of the 6-DOF System

The STC model was modelled as 1- and 2-DOF systems in MATLAB and these were tested in the previous Chapter. However, these systems were solved with the added mass and potential damping terms at one specific frequency and do not take into account the retardation function. In this Chapter, simulations are performed for 6-DOF 1-body SIMO model, referred to as the numerical model, in the time domain and the results are compared with the simplified MATLAB models and the experimental data.

8.1 Decay Test Comparison

Drag is introduced in the SIMO model in the following ways:

- Potential damping in heave and pitch. This is inherently implemented as the system is solved in the time domain using the retardation function.
- Linear damping in heave and pitch. This represents additional potential damping that can be added to tune the system.
- Quadratic damping in heave and pitch. This represents additional viscous damping that can be added to tune the system.
- Viscous elements in pitch. The body of the SIMO system is modelled using slender elements with a C_D of 1.2 so that the distributed drag force can be computed.

This is not modified in the tuning process.

Since there are no viscous elements in heave, additional damping needs to be added to tune the heave degree of freedom. Once the damping ratio in heave of the SIMO model matches that from the experimental data, further tests can then be performed.

Dr. Ling Wan identified a decay ratio of 7% in heave for the MWL mode of the STC concept Wan (2016). It should be noted that all the values of damping are linearized, that is the contribution from both potential and viscous damping are lumped into one value. A decay test in heave was performed on the SIMO model to identify the natural period in heave as well as the damping ratio. This is done by applying a specified force in the positive z-direction at the centre of gravity of the body.

Usually, the force would be applied as a ramp phase, a constant phase and it would then be released so that the body would be free to decay. However, it was found that some instability occurred in the constant phase, likely due to the mooring lines which have unequal stiffness, and the other degrees of freedom were excited. Therefore, only the ramp phase is applied and the force is then released.

It was found that the damping ratio in heave was in the order of 3%, which far from the 7% experimental value. In tuning his 2-body SIMO model, Dr Ling Wan added quadratic damping to heave and this value was added to the 1-body SIMO model. Linear damping was also added so that a decay level of 7% can be achieved.

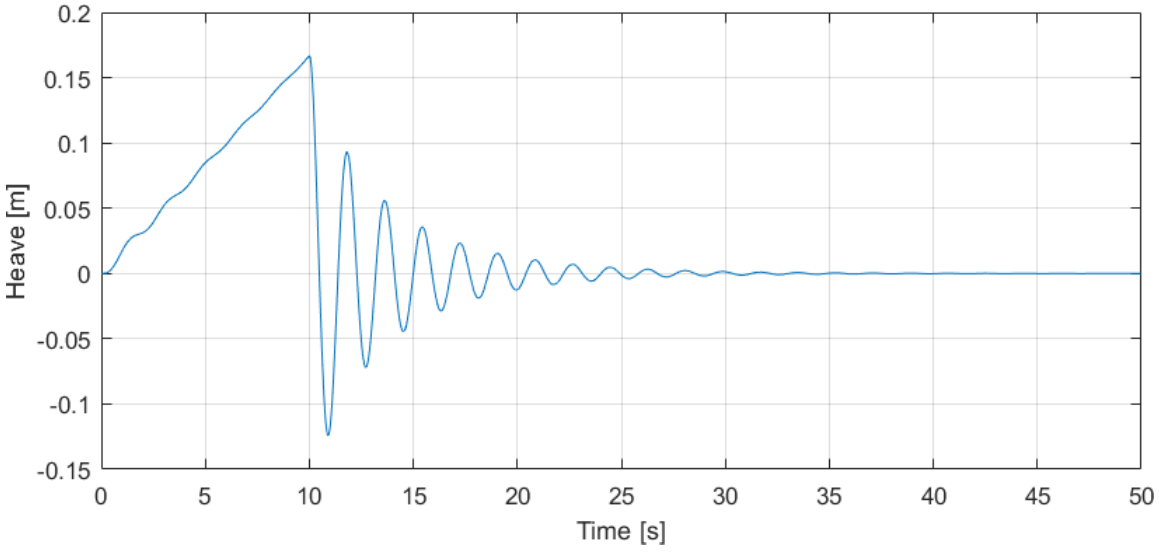

Figure 8.1: *Decay test of SIMO model with tuned heave damping coefficients (model scale).*

Fig. 8.1 shows the decay test with the tuned heave damping coefficients. Using 7 peaks, the damping ratio in heave is found to be 7%. The natural period of the heave motion is 1.8 s. The current tuned heave damping will be used throughout the remaining tests.

The damping in pitch was more difficult to tune because of the coupling in surge. Wan (2016) mentions a damping ratio of 4% in the pitch decay test but it was hard to estimate this number from the experimental data. Fig. 8.2 shows a comparison between the decay test from the experiment and a decay test in SIMO. It should be noted that the pitch damping is not yet tuned at this stage.

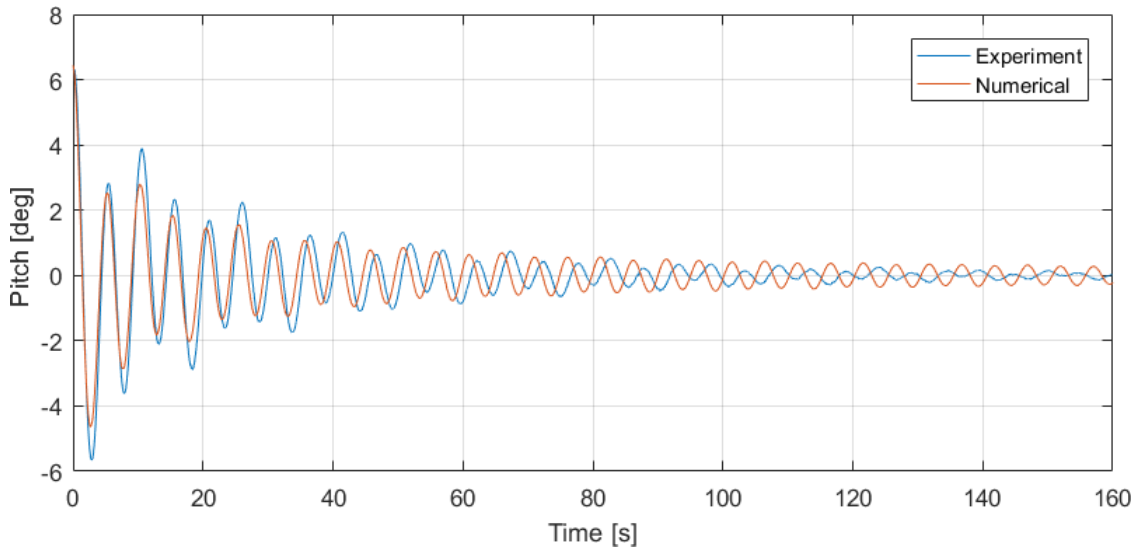

Figure 8.2: *Comparison of numerical and experimental pitch decay test with no tuned pitch damping (model scale).*

The two curves in Fig. 8.2 do not match because there is a small difference in the pitch natural period between the numerical and experimental model. From the experimental data, the pitch natural period is found to be 5.15 s (36.42 s in full scale) whereas the natural period identified from the numerical model is 5.07 s (35.85 s in full scale). However, the damping level for the numerical model is also found to be about 4%.

The problem with estimating the damping ratio is that the average damping ratio between a certain number of peaks is calculated. Viscous damping is dominant for large pitch motions while potential damping is dominant for small pitch motions. Therefore,

if the large peaks are selected, the resulting damping ratio will be higher than 4% whereas if more or smaller peaks are selected, the damping ratio will decrease.

8.2 Regular Wave Test Comparison

The beginning of the wave time series recorded by wave probe 3 (WP3) is shown in Fig. 8.3. Wave probe 3 is at a distance of 0.77 m before the STC model, that is the wave propagates in the direction of the STC model from wave probe 3.

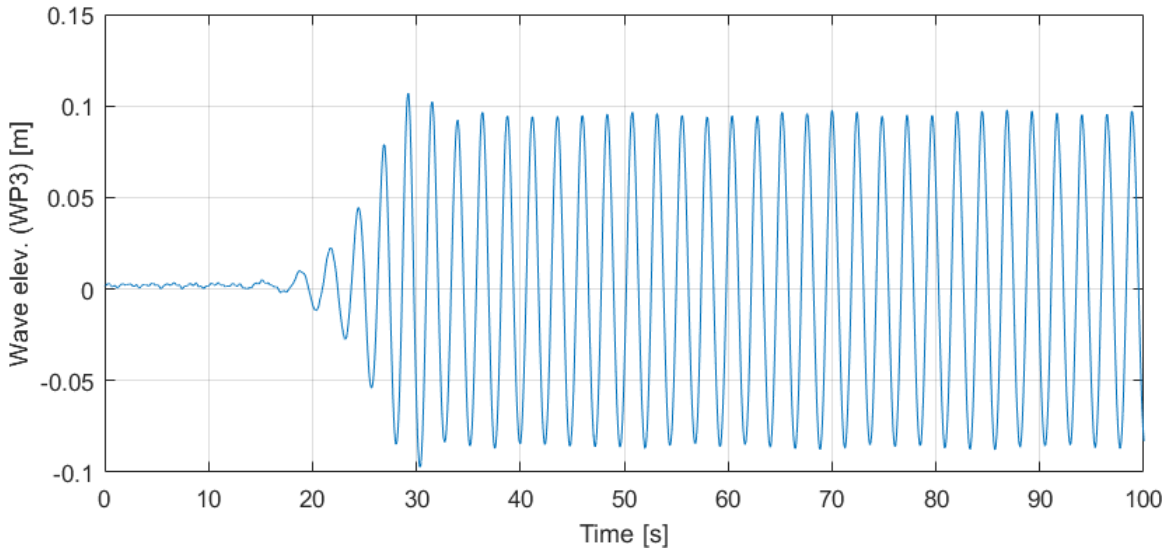

Figure 8.3: *Wave time series recorded by wave probe 3 (model scale).*

It can be seen that the initial cycles, up to about 35 s, consist of a number or irregular waves having different wave heights. Moreover, SIMO uses Fourier analysis to account for the distance between the wave probe and the STC model and this introduces a number of waves having different frequencies. This creates an initial transient in the pitch response and a lot of cycles are required to reach the steady state phase. Therefore, instead of importing the wave time series of the experiment into SIMO, a regular wave environment is applied to run the regular wave tests.

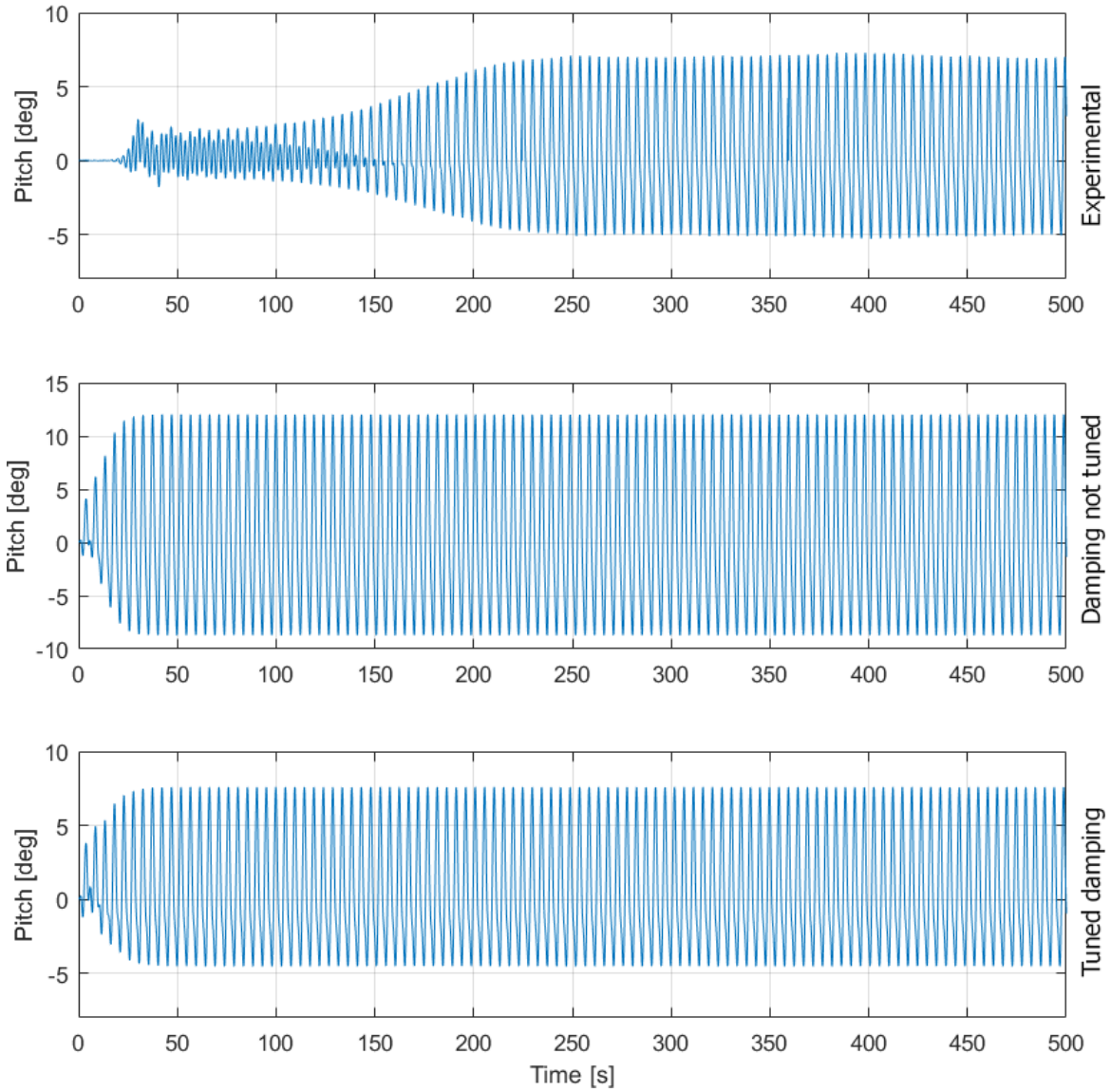

Figure 8.4: *Comparison of regular wave tests for the experimental and numerical models, with and without tuned damping (model scale).*

For the case where the pitch damping is not tuned (middle plot in Fig. 8.4), the maximum pitch was in the order of 12 degrees, which is almost twice as much as what was observed experimentally. Viscous damping is then added and tuned so that the pitch amplitude obtained numerically matches what was observed experimentally. This is shown in the bottom plot in Fig. 8.4. It should be noted that the mean pitch is smaller than that of the experimental model.

With the tuned damping in pitch, it is possible to run a decay test and compare the result with the model test, as shown in Fig. 8.5. The damping is found to be about 6.5% but as was previously explained, this was difficult to estimate.

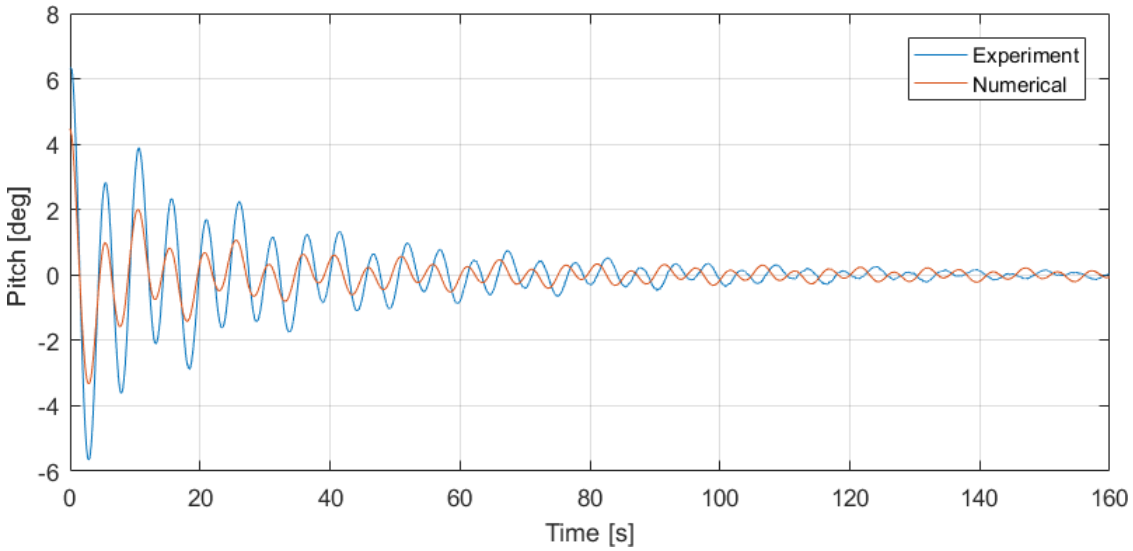

Figure 8.5: *Comparison of numerical and experimental pitch decay test with tuned pitch damping (model scale).*

The decay tests in SIMO were rendered monotonous by applying forces in surge in the negative x-direction. Then, decay tests from different initial pitch amplitudes were run to compare the change in damping ratio with pitch amplitude. An example of a decay test with an initial pitch of 10 degrees is shown in Fig. 8.6.

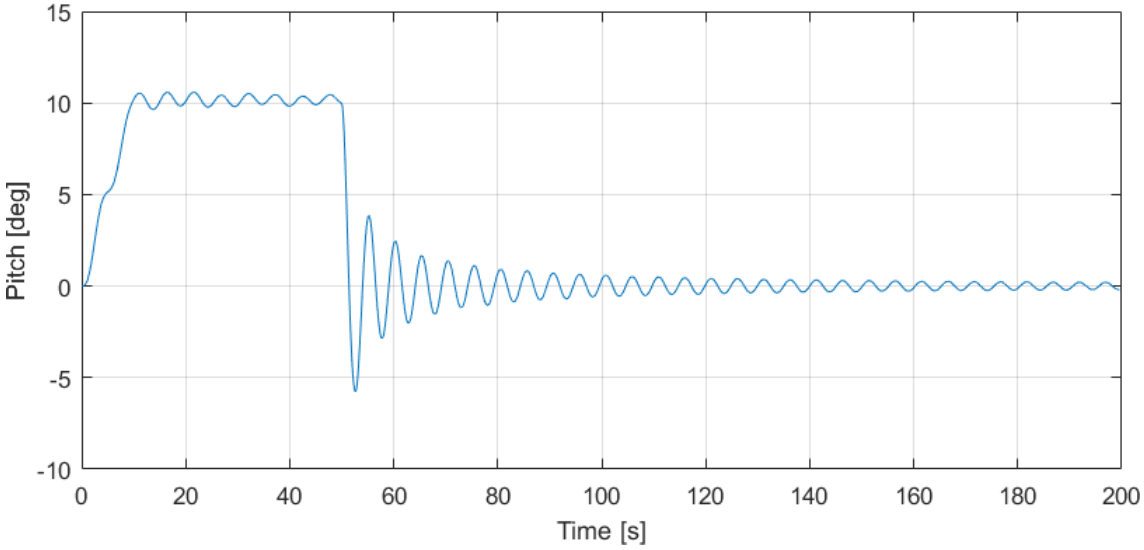

Figure 8.6: *Pitch decay test in SIMO (model scale).*

Viscous damping is more significant when the pitch amplitude is high and therefore, when calculating the damping ratio, only the peaks that are greater than 1 degree are considered. The following table shows the damping ratio obtained in the decay tests for different initial pitch amplitudes. It should be noted that a tuned pitch damping ratio of 6.5% is used for in the upcoming tests.

Table 8.1: *Damping ratio with different initial pitch amplitudes.*

Initial Pitch	7°	8°	9°	10°
Damping Ratio	5.99%	6.34%	6.66%	6.95%

Table 8.2 gives a comparison of the pitch natural period and damping ratio for the numerical models and the experimental one. It can be seen that the natural period for the SIMO model is very close to what was obtained experimentally. The natural period of the MATLAB 2-DOF model is closer to the experimental value when compared with the 1-DOF model. This suggests that the surge-pitch coupling is important and cannot be neglecting when modelling the structure. The original damping ratio of the SIMO model was about 4% but this was tuned to 6.5% as mentioned earlier.

Table 8.2: *Comparison of natural period and damping ratio.*

Parameter	Matlab 1-DOF	Matlab 2-DOF	SIMO 6-DOF	Experiment
$T_{N,5}$ (model scale)	6.64 s	5.86 s	5.07 s	5.18 s
$T_{N,5}$ (full scale)	46.95 s	41.44 s	35.85 s	36.6 s
Damping ratio	3%	2.8%	6.5%	4%

Fig. 8.7 and 8.8 show the comparison of the spectral analysis of the time series of the numerical and experimental models. Similar to the regular wave tests, the wave period is 2.40 s (17 s in full scale) and the wave height is 0.18 m (9 m in full scale). The wave time series from the experimental data was imported into SIMO. It can be seen that the spectral analysis for the numerical method is very similar to the experimental one. However, for the amplitude of the peaks of the surge spectrum for the numerical model is smaller than the experimental model.

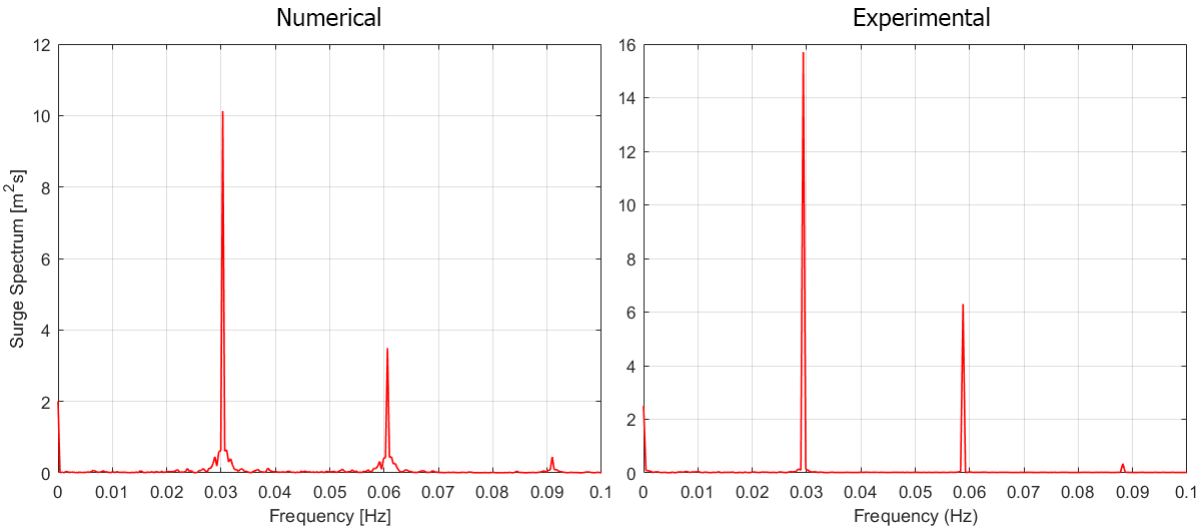

Figure 8.7: *Comparison of the spectral analysis of the surge motion of the numerical and experimental models (full scale).*

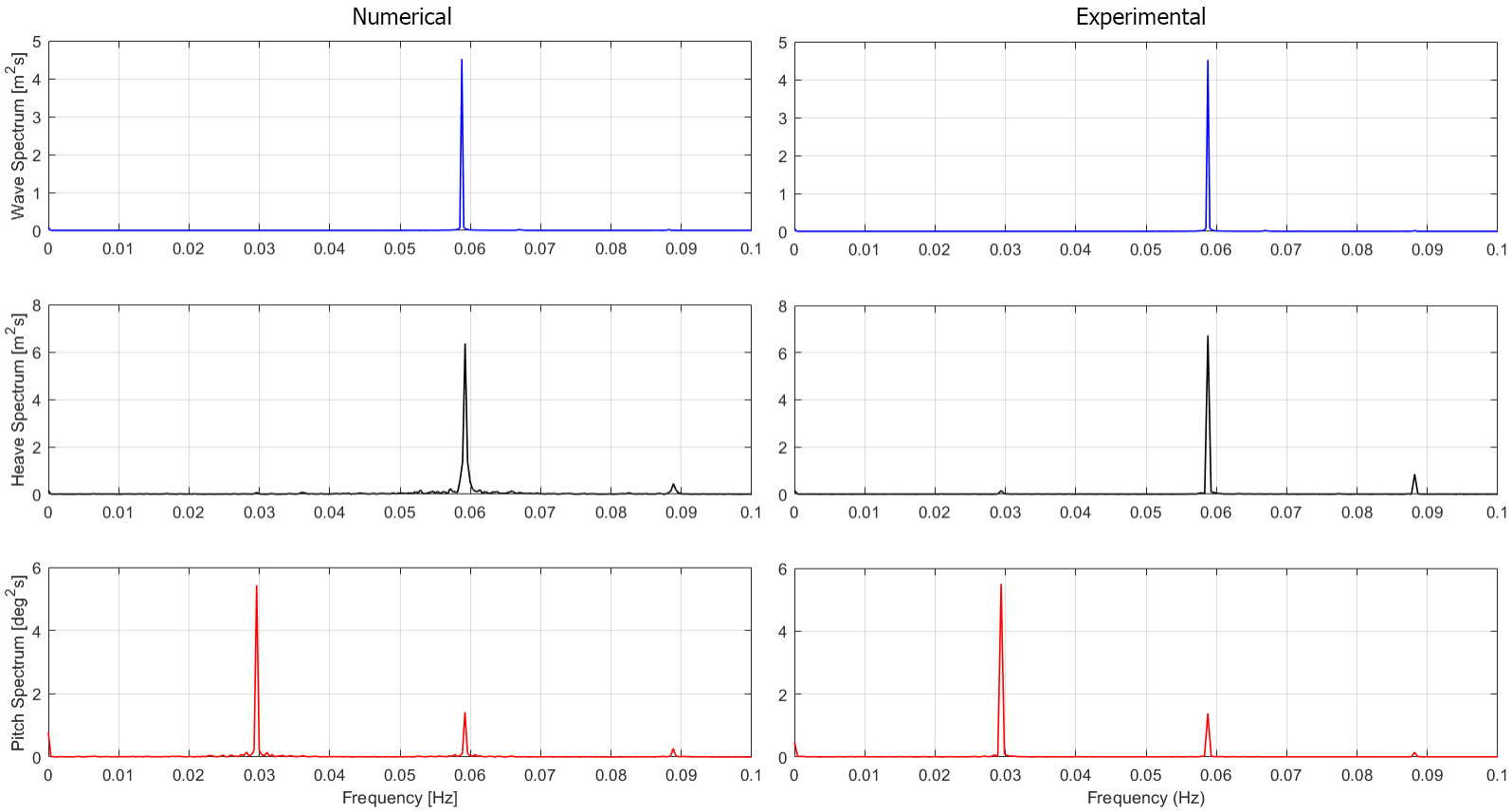

Figure 8.8: *Comparison of the spectral analysis of the numerical and experimental models (full scale).*

Fig. 8.9 shows the comparison of the phases of the time series of the numerical and experimental models. It should be noted that for both cases, a random section of the steady state of the time series was cut and fitted to a time scale such that the wave elevation is zero at time zero for ease of comparison.

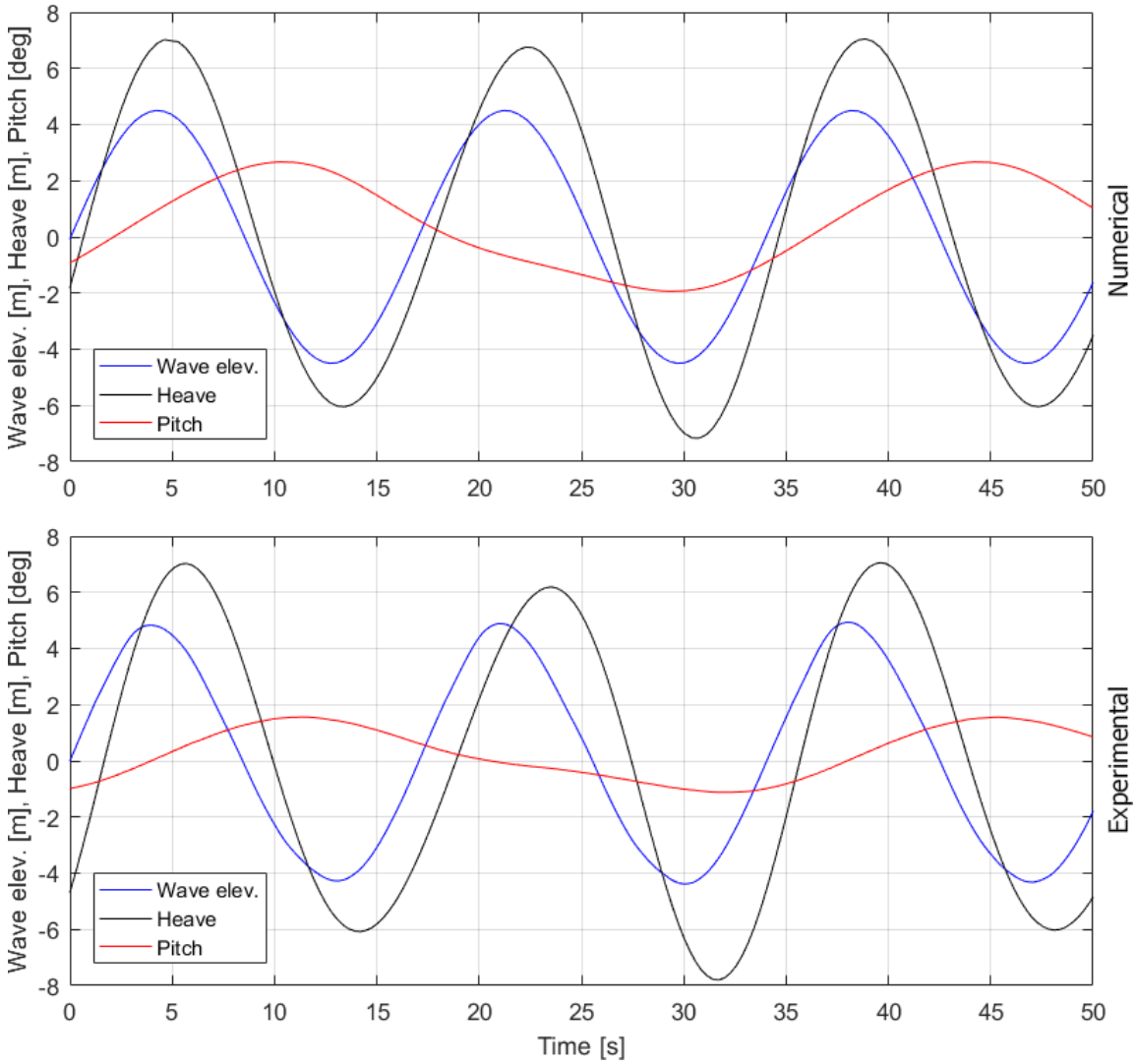

Figure 8.9: *Comparison of the phase difference of the numerical and experimental models (full scale).*

It was identified in Chapter 5 that in the experiment, the phase shift between the wave profile and the heave motion was -37.2° (time delay of 1.76 s) and the phase shift between the wave profile and the pitch motion was -157° (time delay of 7.42 s). In the numerical model, the phase shift between the wave profile and the heave motion is -7.5°

(time delay of 0.36 s) and the phase shift between the wave profile and the pitch motion is -120° (time delay of 5.66 s). However, the time delay between the heave and pitch motions for both cases is about 5.4s. The phase shifts are summarized in the following table:

Table 8.3: *Comparison of phase difference of the numerical and experimental models (full scale).*

Motion	Numerical	Experimental
Heave	-37.2°	-157°
Pitch	-7.5°	-120°

8.3 Sensitivity Analysis

Fig. 8.10 shows the RAO of the experimental model. For the small wave height (0.04m), the RAO for the whole range of wave periods is small, that is, in the order of 0.25. The RAO for the large wave height (0.18m) is approximately the same except when Mathieu instability occurs. When this happens, the RAO is in the order of 1.2. It should be noted that Mathieu instability only occurred for the large wave height.

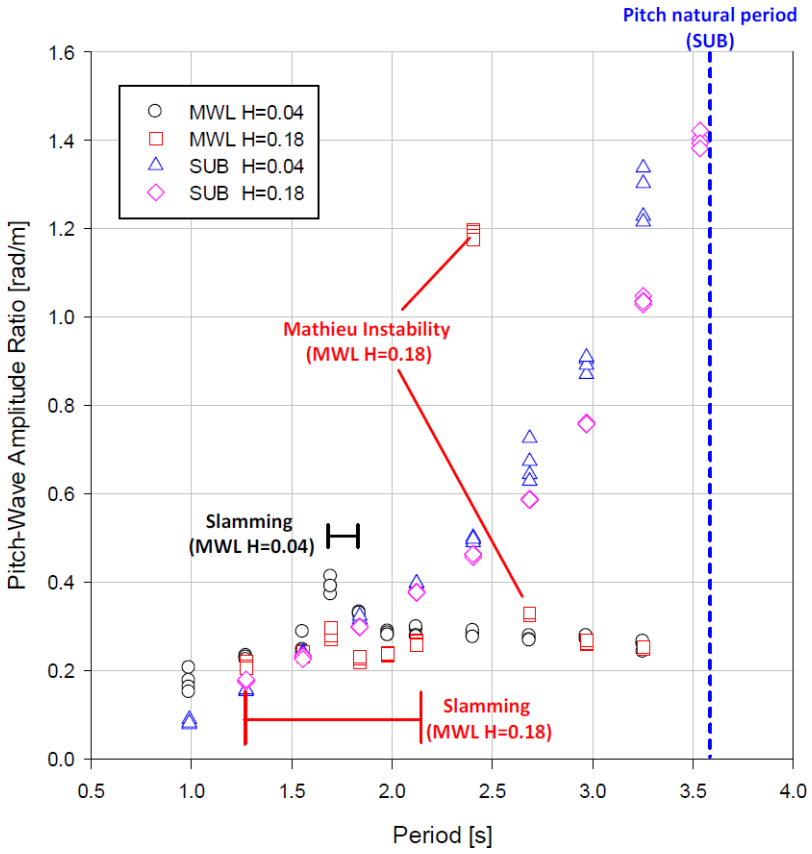

Figure 8.10: *RAO of experimental case (model scale).*

Fig. 8.11 shows the RAO of the SIMO model for the case where the hydrostatic stiffness is not made to vary. The RAO is calculated by dividing the pitch amplitude by the wave amplitude, that is, half the wave height. It can be seen that Mathieu instability for the larger wave height occurs at a wider range of wave periods and the RAO is higher when compared with the small wave height scenario. It is interesting to note that even for the case where the stiffness does not vary, the RAO for the small wave height, at a period equal to half the pitch natural period, is about three times the value of what was observed experimentally.

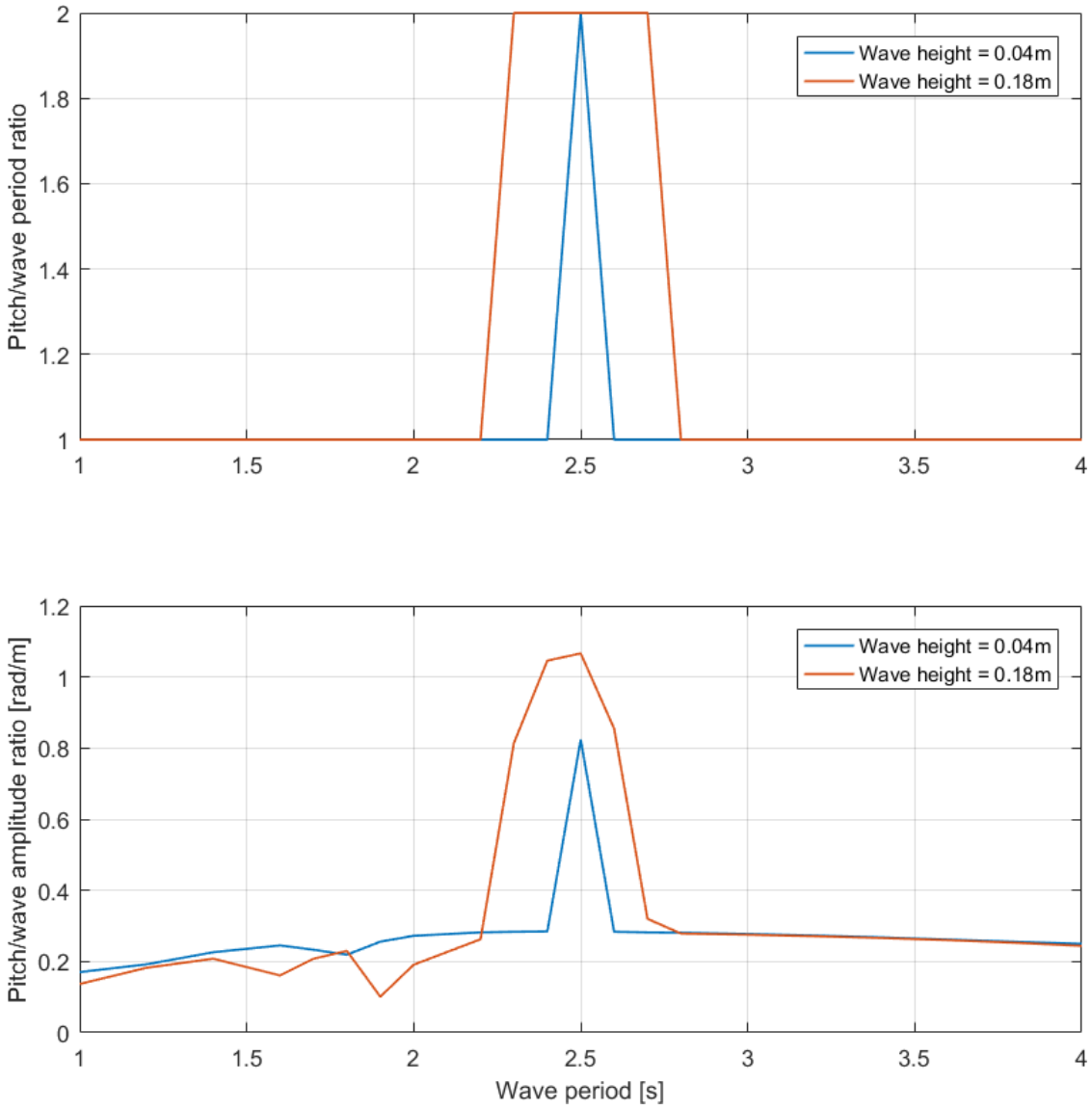

Figure 8.11: *Response of SIMO model without stiffness variation (model scale).*

Fig. 8.12 shows the RAO of the SIMO model for the case where the hydrostatic stiffness is made to vary as a function of the heave motion and the damping in pitch is not tuned. It can be seen that the RAO for both wave heights is almost twice as much as what was observed experimentally. This shows how viscous damping is significant when the pitch amplitude is large. Moreover, Mathieu instability occurs at a wider range of wave period as compared with the case where the hydrostatic stiffness is not made to vary.

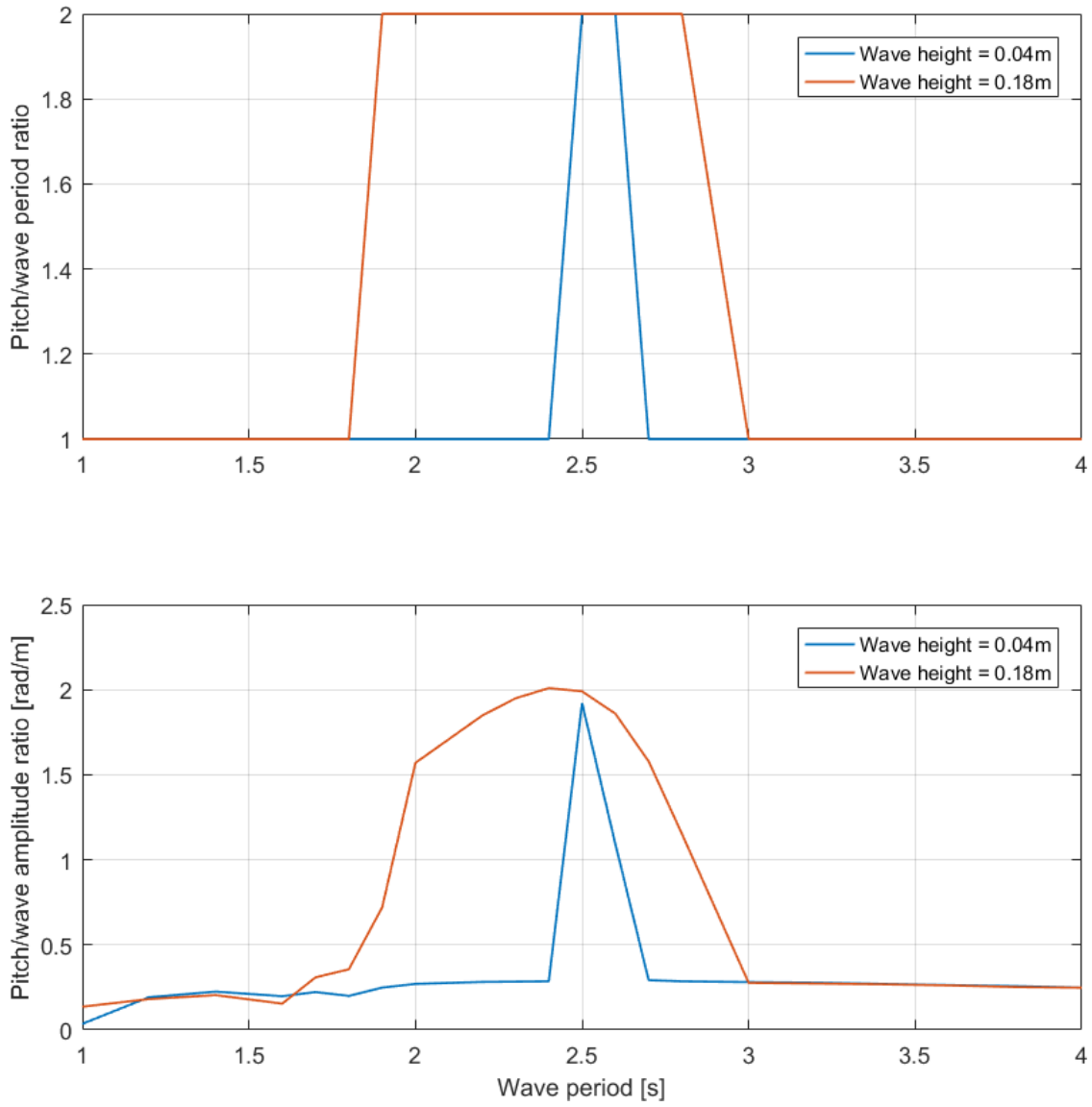

Figure 8.12: *Response of the SIMO model with stiffness variation (model scale). Pitch damping is not tuned.*

Fig. 8.13 shows the RAO of the SIMO model for the case where the hydrostatic stiffness is made to vary as a function of the heave motion and the damping in pitch is tuned. It can be seen that the amplitude of the peak of the large wave height case is now more comparable with what was obtained experimentally even though the range of wave period over which Mathieu instability occurs is much wider. The kink in the curves which occurs around the wave period of 1.8 s can be attributed to the occurring of heave resonance.

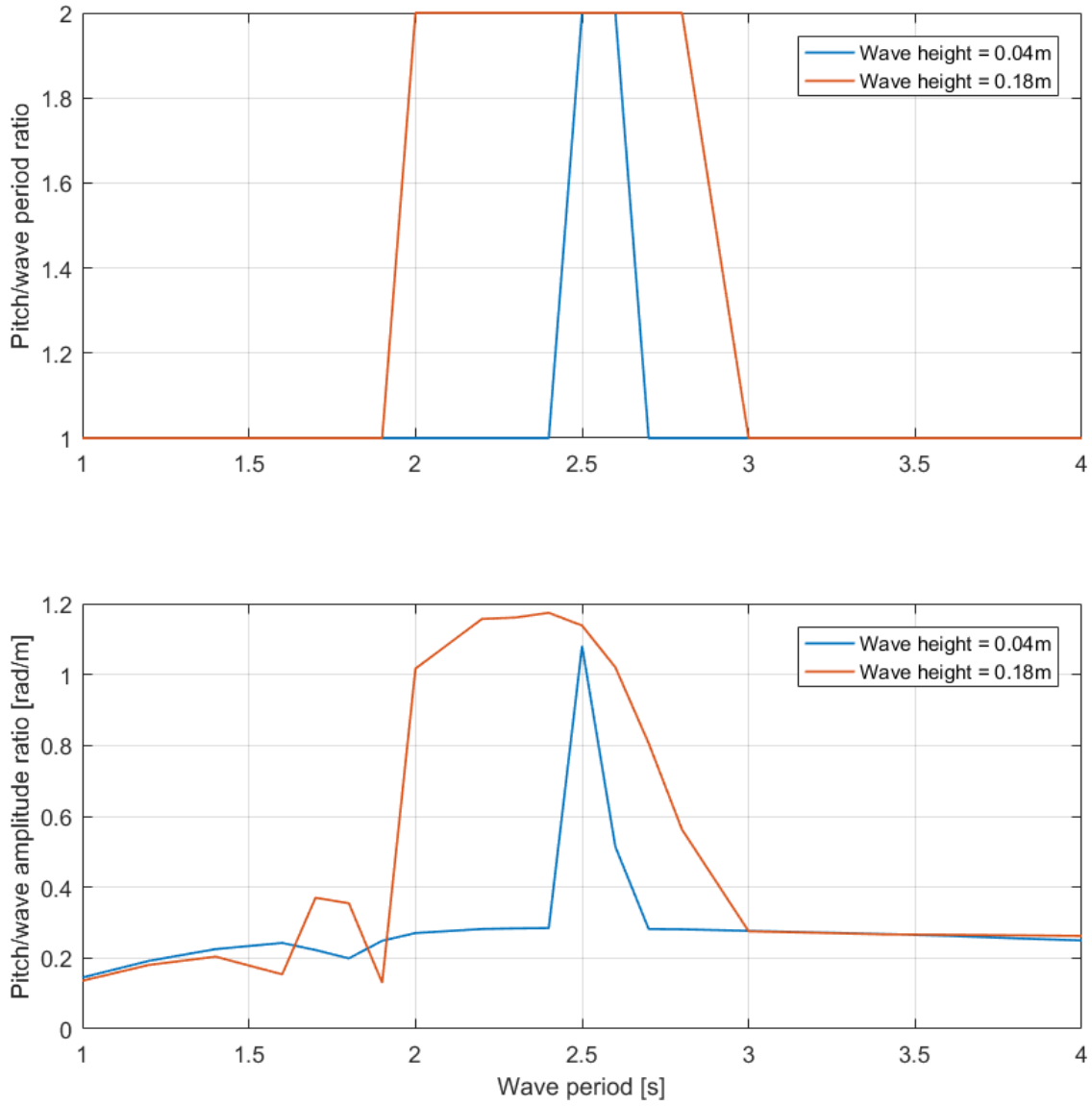

Figure 8.13: *Response of the SIMO model with stiffness variation (model scale). Pitch damping is tuned.*

The mooring lines are removed from the SIMO model and the stiffness provided by them is added to the hydrostatic matrix. Decay tests and eigenvalue analysis were performed to ensure the natural periods are similar to the case where the mooring lines are still present. Then, the 1-body model is subjected to a regular wave environment with wave height 0.04 metres and wave period 2.5 seconds, with the wave period equal to half the pitch natural period. The time series is shown in Fig. 8.14.

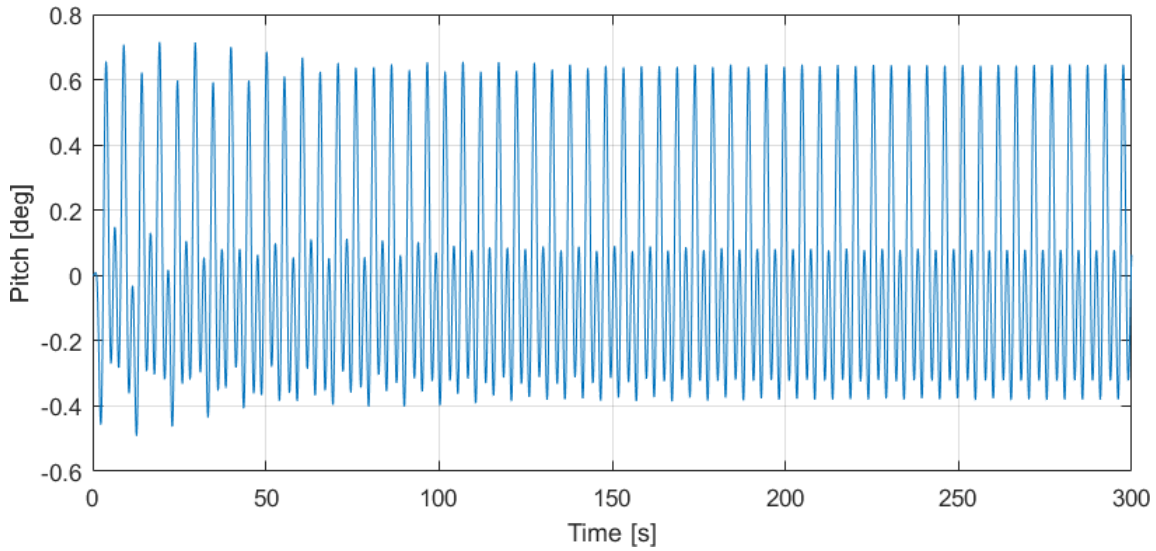

Figure 8.14: *Time series of the pitch motion without mooring lines (full scale).*

It can be seen from Fig. 8.14 that there are two frequencies in the response of the pitch motion, shown by a series of large and small peaks. A spectral analysis is performed on the steady state phase of the time series and is shown in Fig. 8.15. The peak at 0.2 Hz corresponds to the pitch natural period and the peak at 0.4 Hz corresponds to the wave period.

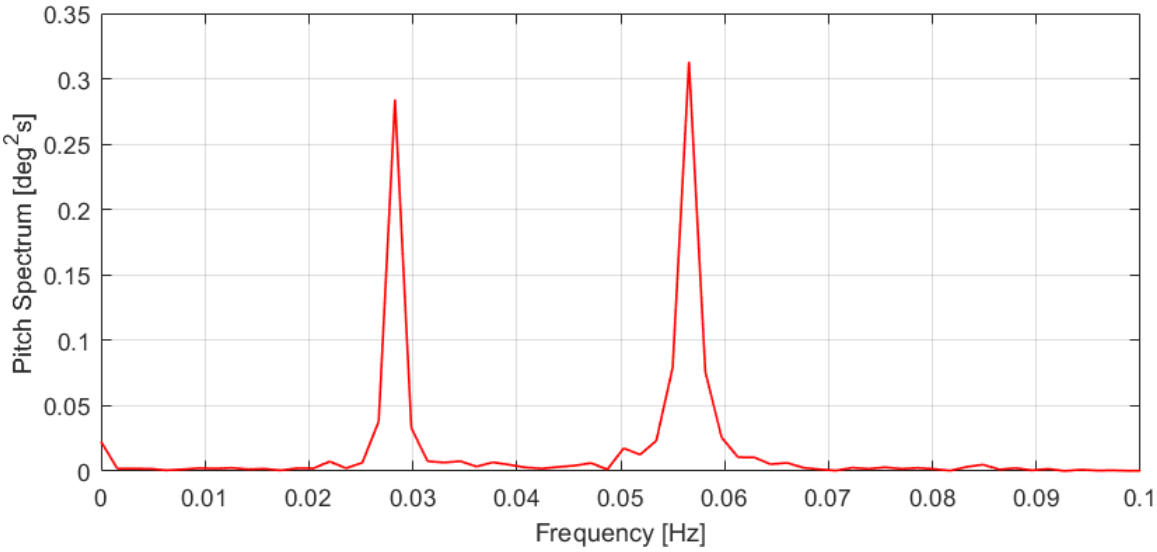

Figure 8.15: *Spectral analysis of the time series of the pitch motion without mooring lines (model scale).*

The equation of motion can be written as:

$$(I_{55} + A_{55})\,\ddot{\eta}_5 + B\dot{\eta}_5 + K\eta_5 = F_{ext} + F_{drag} + F_{cons} \tag{8.1}$$

The right hand side of the equation of motion consists of the external excitation force (F_{ext}), the drag force (F_{drag}) and a constant force (F_{cons}) which is the result of second order forces. The drag force can be expressed as:

$$F_{drag} \propto (v - \dot{x})\,|v - \dot{x}| \tag{8.2}$$

Mathieu instability was not observed in the experiment but occurred in the numerical model, even at the small wave height (0.02 m). This could be explained by the drag terms which is a function of the square of the velocity, and hence, the response occurs at two frequencies.

8.4 Irregular Waves

No Mathieu instability was observed experimentally for either small or large wave heights. However, the largest significant wave period used for the irregular waves was 15.5 s, which is not close to 18.3 s, which is half the pitch natural period.

The SIMO 1-body model is subjected to irregular waves to investigate its response. Two cases are used for the SIMO model: the first case takes the hydrostatic stiffness to be constant and the second case accounts for the varying hydrostatic stiffness as a function of the heave motion. Significant wave heights of 0.04 m and 0.18 m (full scale 2 m and 9 m) are considered and the wave period is set to 2.5 s (full scale 17.68 s). The spectral analysis of the wave elevation time series with significant wave height of 9 m and wave period of 17 s (0.059 Hz) in full scale is shown in Fig. 8.16.

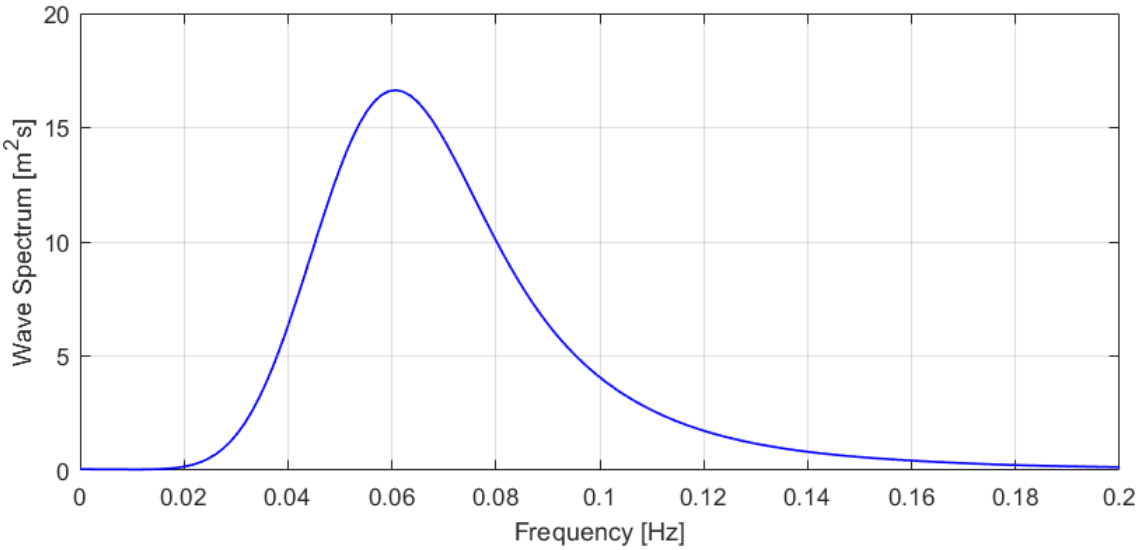

Figure 8.16: *Spectral analysis of the wave elevation with significant wave height 9 m and wave period 17 s (full scale).*

Fig. 8.17 shows the time series of the wave elevation and pitch motion with irregular waves of wave height 0.18 m (full scale 9 m) and wave period 2.5 s (full scale 17.68 s). Based on the largest peaks of the pitch motion and the closest peaks of the wave elevation, it can be seen that there is a phase difference between the wave elevation and the pitch motion. The large peaks of the pitch motion occur at a period equal to twice the wave period but it is difficult to conclude that this is due to Mathieu instability.

Second order forces such as mean drift influence the pitch response even though they were found to be small compared to the first order wave forces.

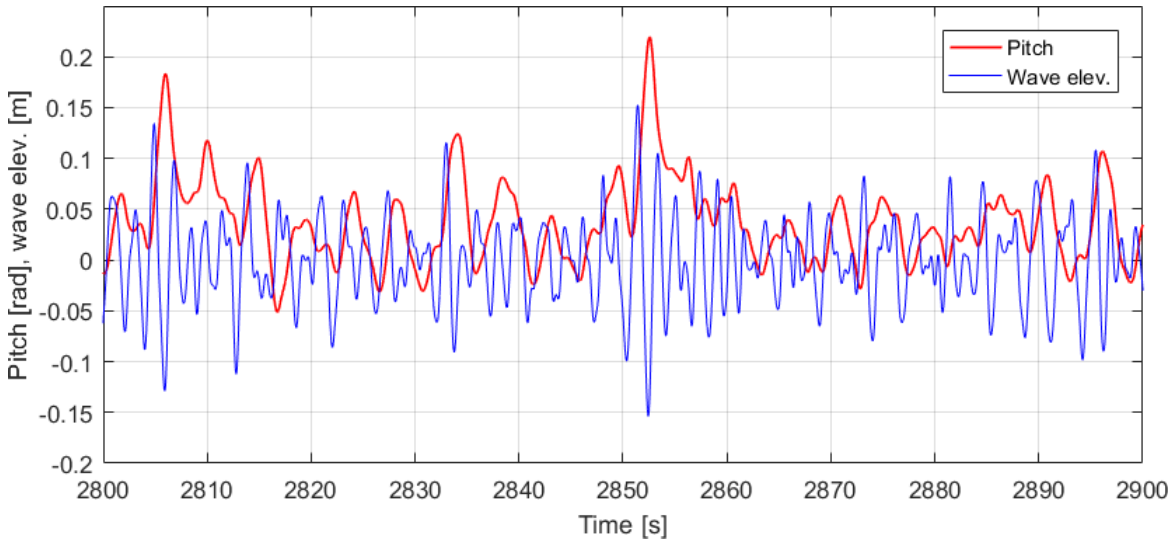

Figure 8.17: *Time series of the wave elevation and pitch motion with irregular waves of significant wave height 0.18 m and wave period 2.5 s (model scale).*

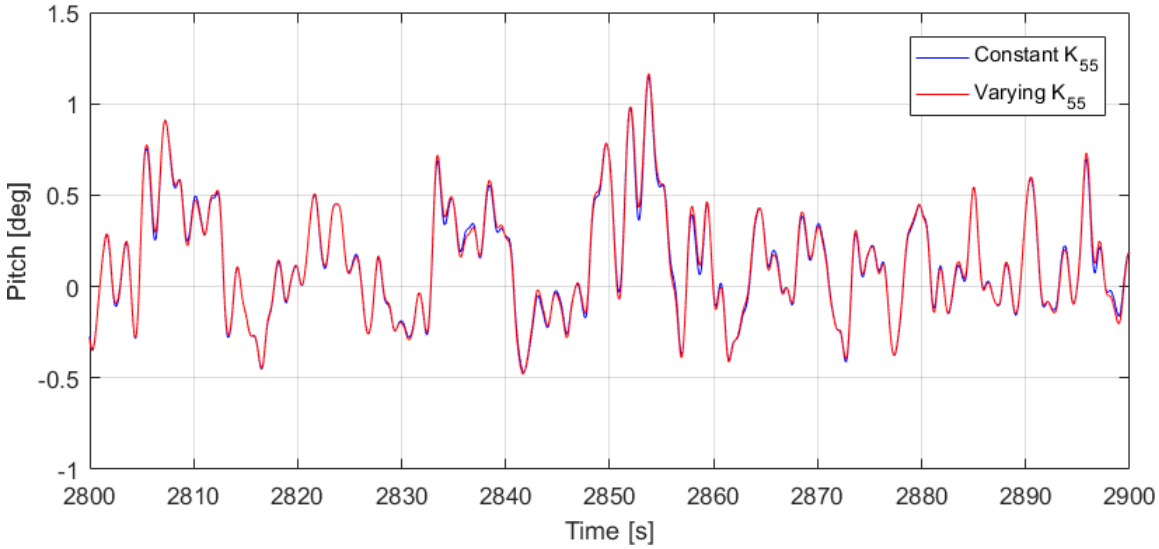

Figure 8.18: *Comparison of the time series with irregular waves of significant wave height 0.04 m and wave period 2.5 s (model scale).*

Fig. 8.18 shows the comparison of the time series with irregular waves of significant wave height 0.04 m (full scale 2 m) and wave period 2.5 s (full scale 17.68 s). Both

curves are approximately the same because the amplitude of the heave motion is small and therefore, there is no significant change in stiffness of the structure.

Fig. 8.18 shows the comparison of the time series with irregular waves of significant wave height 0.18 m (full scale 9 m) and wave period 2.5 s (full scale 17.68 s). There is a larger difference between the curves when compared with the case where the wave period is small, that is 0.04 m in model scale. The most notable difference is that for large wave heights, the amplitude of the peaks of the case where the stiffness is allowed to vary is larger than the case with constant stiffness.

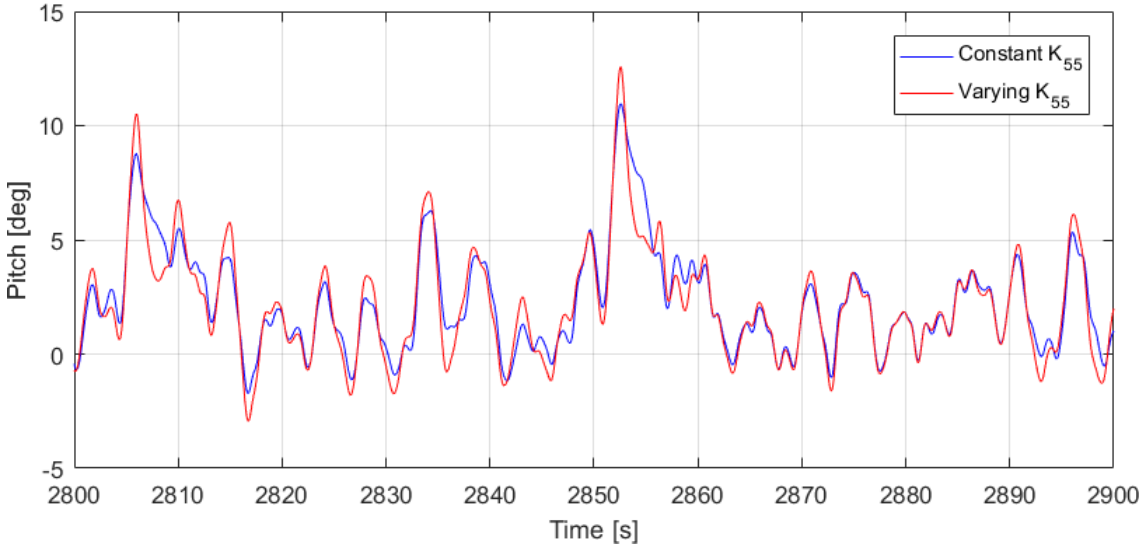

Figure 8.19: *Comparison of the time series with irregular waves of significant wave height 0.18 m and wave period 2.5 s (model scale).*

Fig. 8.20 shows the comparison of the spectral analysis with irregular waves of significant wave height 2 m and wave period 17.68 s in full scale. The first peak around 0.09 Hz corresponds to the surge natural period, the second peak around 0.028 Hz corresponds to the pitch natural period and the third peak around 0.057 Hz corresponds to the significant wave period. As expected, the case where the stiffness is allowed to vary has a larger peak at the pitch natural period. This peak is about 46% larger than in the case where the stiffness is constant.

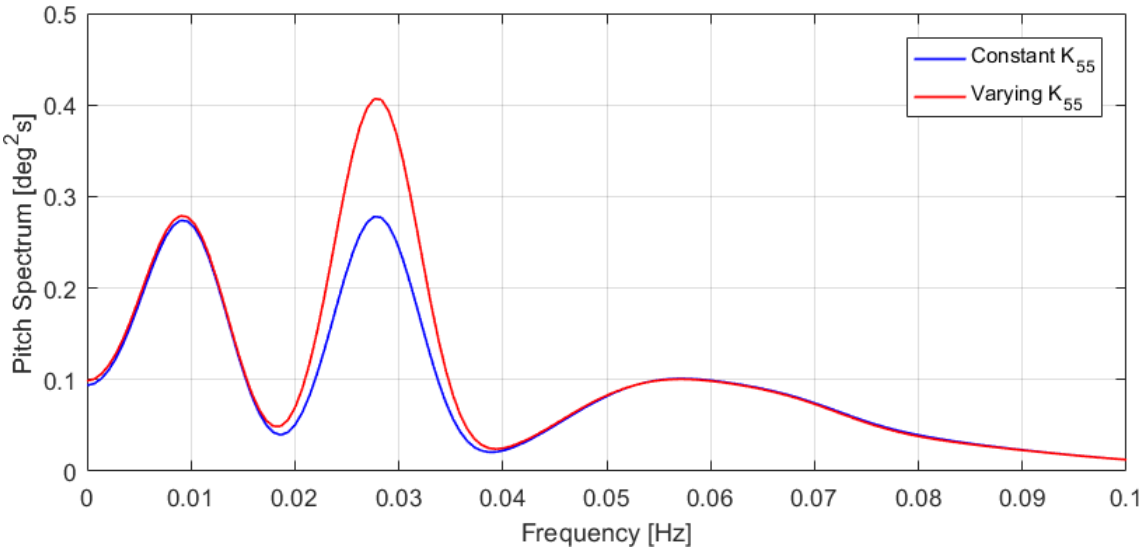

Figure 8.20: *Comparison of the spectral analysis with irregular waves of significant wave height 2 m and wave period 17.68 s (full scale).*

Fig. 8.21 shows the comparison of the spectral analysis with irregular waves of significant wave height 9 m and wave period 17.68 s in full scale. The first peak around 0.09 Hz corresponds to the surge natural period, the second peak 0.028 Hz corresponds to the pitch natural period and the third peak around 0.057 Hz, which is rather small and flat, corresponds to the significant wave period. The case where the stiffness varies has a peak that is about 16% smaller at 0.0048 Hz and a peak that is about 89% larger at 0.057 Hz.

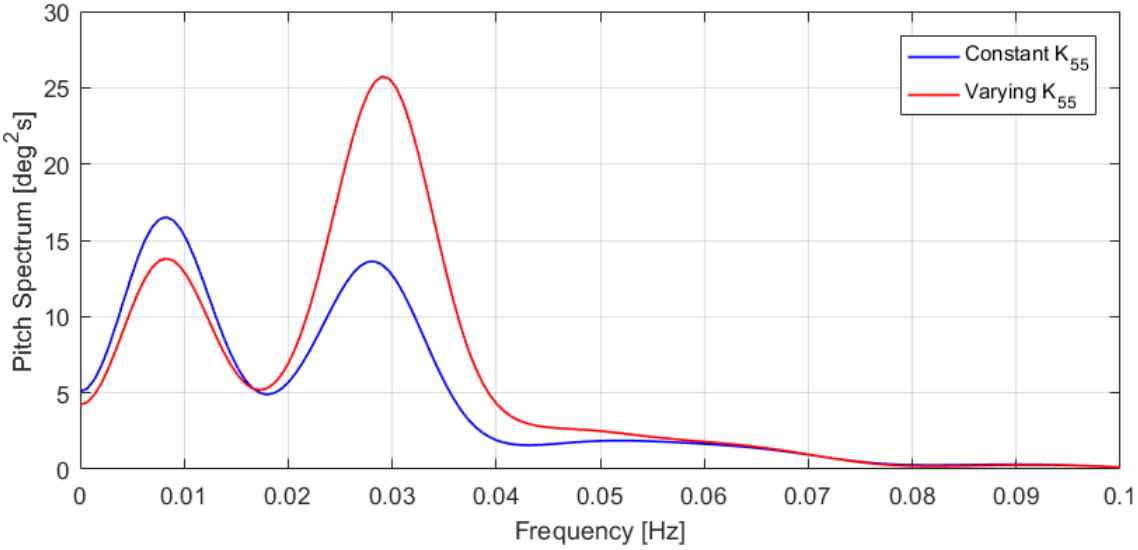

Figure 8.21: *Comparison of the spectral analysis with irregular waves of significant wave height 9 m and wave period 17.68 s (full scale).*

Experimental test data of the STC for irregular waves with a 100-year return period was provided by Dr. Ling Wan. The spectral analysis of the wave elevation time series is shown in Fig. 8.22 and it can be seen that there is still a lot of energy at very low frequencies.

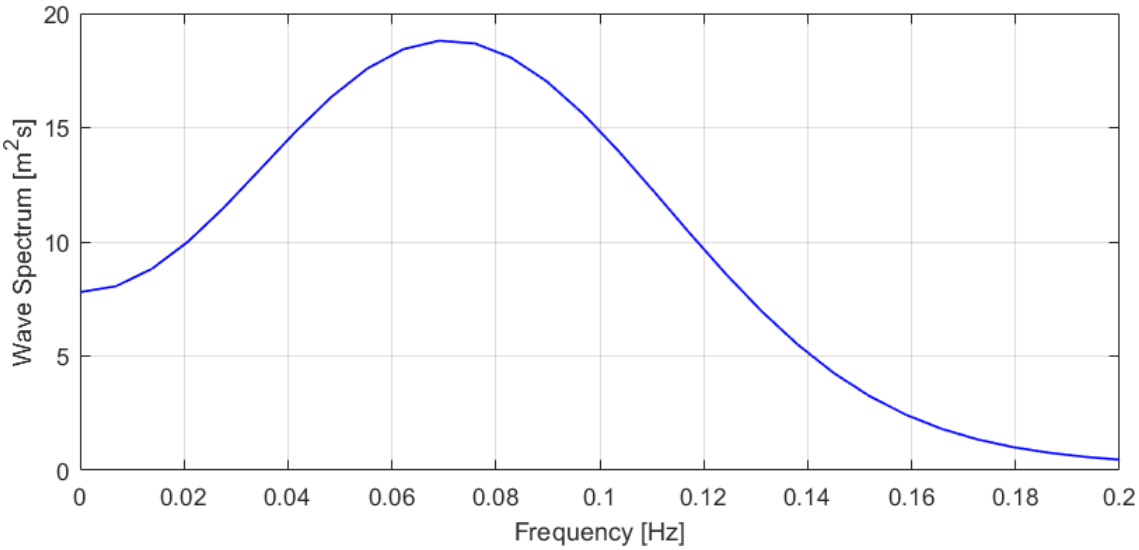

Figure 8.22: *Spectral analysis of the wave elevation time series with a 100-year return period (full scale).*

The wave elevation time series is imported into SIMO and the pitch response is investigated. Fig. 8.23 shows the comparison of the spectral analysis of the pitch motion of the experimental and numerical models. The large peak for the experimental case occurs at about twice the wave natural period. The peak for the numerical model where the hydrostatic stiffness varies is larger at twice the wave natural period that that of the case where the hydrostatic stiffness is constant at the frequency of 0.028 Hz. The peaks around 0.009 Hz correspond to the surge natural frequency. There is a lot of energy at the low frequencies because the wave time series is broad-banded and there is a large mean pitch value. Moreover, the waves are almost twice as large as the regular case waves and there is a much large heave response. Slamming occurs and this nonlinear phenomenon cannot be accurately modelled in SIMO and therefore, the results may not be realistic.

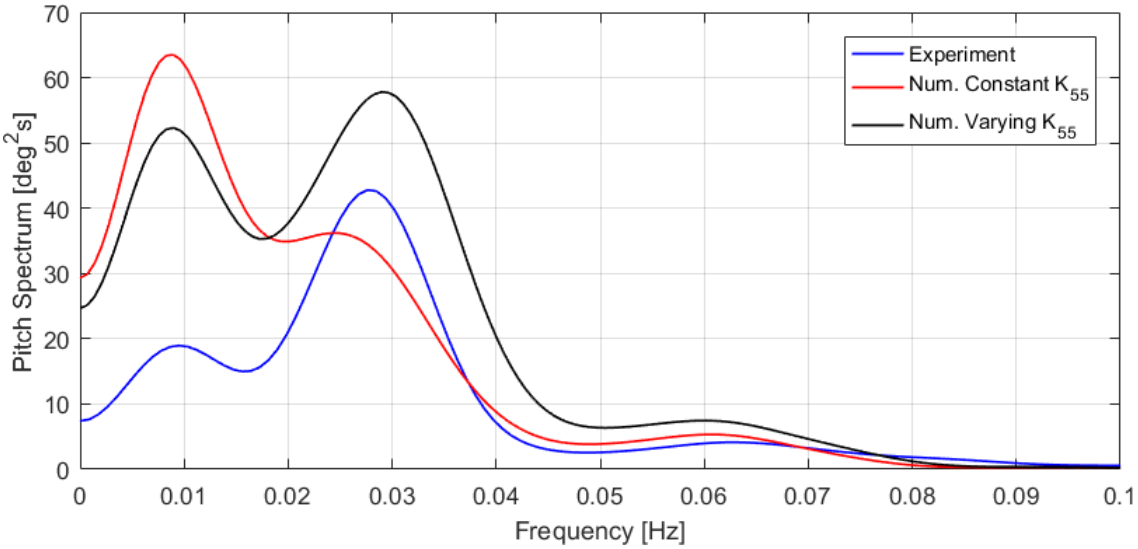

Figure 8.23: *Comparison of the spectral analysis of the pitch motion of the experimental and numerical models (full scale).*

Fig. 8.24 shows the comparison of the time series of the pitch motion of the two numerical models. As found previously, the peaks for the case where the hydrostatic stiffness varies are larger than that were the hydrostatic stiffness is constant even though the general pitch motion for both cases are not exactly the same. The time series for the experimental case was not included in Fig. 8.24 because of the difference in phase shift between the experimental and numerical models.

It should be noted that the amplitudes for the pitch motions of the numerical cases were much larger than what was observed experimentally. The largest pitch motion was 11.4° for the experimental case, 20.9° for the numerical case where the hydrostatic stiffness is constant and 23.1° for the case where the hydrostatic stiffness varies. This suggests that the damping for the numerical models need to be re-calibrated so that the amplitudes of the pitch motion can match those of the experimental model. The mean pitch value was 2.6° for the experimental case, 4.5° for the case where the hydrostatic stiffness is constant and 4.1° for the case where the hydrostatic stiffness varies.

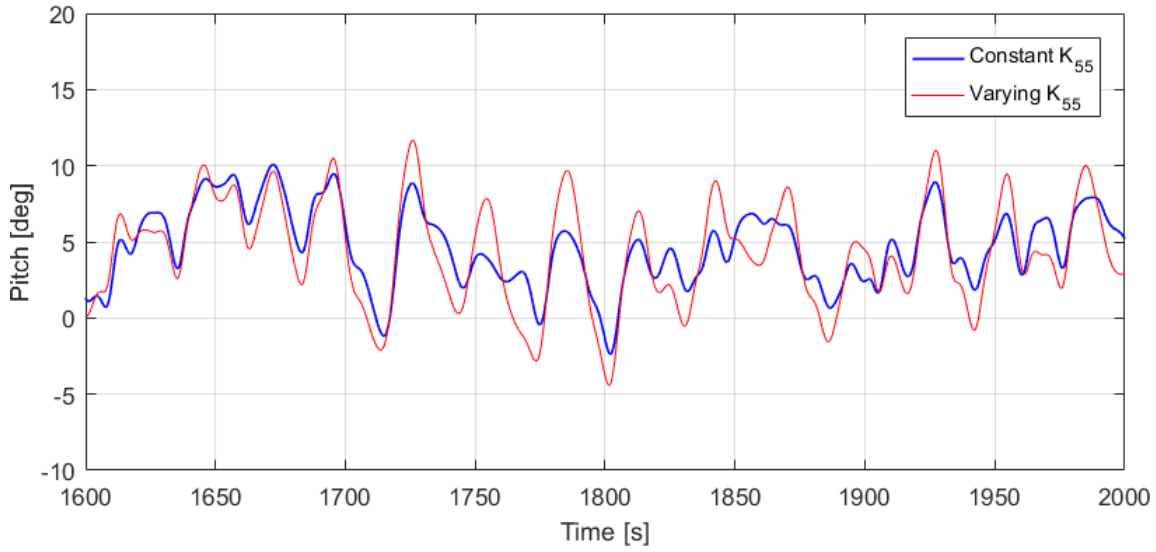

Figure 8.24: *Comparison of the time series of the pitch motion of the numerical models (full scale).*

Chapter 9

Conclusion and Recommendation

The purpose of this study is to numerically predict unstable motions for regular and irregular wave conditions and to compare the results with the experimental observations. The master thesis starts with a literature study on Mathieu instability to understand the mechanism behind this phenomenon. Mathieu instability occurs when the time period of the wave excitation is equal to half of the natural period of the pitch motion and thus, pitch resonance develops. This occurs because the heave motion influences the restoring term of the pitch motion which then varies in time. In the occurrence of Mathieu instability, the period of the pitch motion progressively changes from the period of the wave to twice the wave period. The pitch amplitude also increases until it reaches a steady-state value.

Different types of Mathieu instability were investigated and instability in heave-pitch was prioritized due to its relevance to the STC concept. Parametric roll of a ship was also examined to gain insight into instability due to coupled motions and the effects due to damping were inspected. A description of the experimental study of the STC concept was given and the ways the concept was modelled and tested were also described. Finally, the experimental test results were analyzed to determine in which cases Mathieu instability occurred and the characteristics of this phenomenon. Mathieu instability of STC concept in waves may induce significant loads in the structural components (such as wind turbine blades, nacelle or the interface between the spar and the torus) and it needs to be further investigated.

Two numerical models in MATLAB, a 1-DOF model in pitch only and a 2-DOF model which accounts for the coupling in surge and pitch, were developed. It was found

that the coupling in surge-pitch is important and cannot be neglected in modelling as it influences not only the natural period but also the response of the system to external excitation. Both models exhibited instability when the stiffness varied periodically at half the pitch natural period but Mathieu instability was not observed when an external force was applied. The MATLAB models use constant terms for the added mass and potential damping and the retardation function is not considered. Moreover, the external force is assumed to occur only at a specific frequency.

The SIMO 6-DOF model was tuned and tested and the results were similar to what was observed experimentally. However, the mean pitch and mean surge values in the case of Mathieu instability were different. The amplitude of the surge motion was also different in that case. It was not possible to use the experimental wave time series in SIMO because of the distance between the wave probe measurements and the structure. SIMO uses Fourier analysis to re-create the beginning of the wave time series due to the phase difference and this leads to an incorrect initial transient. Therefore, the development of Mathieu instability, that is the change of pitch period from the wave period to twice the wave period, could not be accurately investigated.

Damping plays an important role in the development of Mathieu instability and this needs to be more precisely examined. It was difficult to obtain the damping ratio from the pitch decay tests of the experiment due to the coupling in surge. Moreover, since the viscous damping is more significant when the pitch motion is large, it would be desirable to calculate the damping ratio for large pitch motions in the decay tests. The decay tests could also be calculated for different initial pitch angles to compare the relative contribution of the potential damping and the viscous damping.

In the SIMO model, Mathieu instability was obtained even for small wave heights, even for the case where the stiffness is assumed to be constant. In the experiment, no Mathieu instability was observed for small wave heights and the spectral analysis showed that the energy of the pitch motion was only at the wave period. One of the problems is that the experimental pitch natural period is 36.6 s and half this value is 18.3 s. However, the wave period used in the experimental tests is 17 s, which is not exactly equal to half the pitch natural period. The pitch natural period in the SIMO model is 36.85 s and the wave period used in SIMO was exactly half the pitch natural period. It is recommended to carry out more experimental tests with the wave period exactly at the pitch natural period. A sensitivity analysis with wave heights and wave

periods close the the Mathieu instability region could be carried out experimentally to validate the numerical model. It is important to also tune the numerical model so that its natural period matches exactly the experimental one.

Numerical tests using irregular waves were briefly investigated. However, since there is no data and occurrence of Mathieu instability experimentally, it was difficult to draw conclusions from the tests. It is recommended to perform various irregular wave tests with different wave heights and with a significant wave period which is exactly half the pitch natural period. Moreover, since the wave period at half the pitch natural period is in the order of 18 s, which is a large value, it would relevant to calculate the probability of occurrence of that particular sea state and to distinguish which sea state can be treated as survival mode for the STC.

The mooring lines contributed more stiffness than the hydrostatic forces and these need to be modelled more accurately so that the drag and inertial forces can be better represented. It was difficult to plot the Mathieu stability diagram but it would be interesting to investigate the stability regions for different wave conditions in future work. This report focused on the instability for the MWL mode but the SUB mode could be investigated as well. The STC in the SUB mode has different natural periods and how the instability regions would be shifted should be examined. Large inertial forces occur during Mathieu instability due to the large pitch motions and the influence of such accelerations on the integrity of the components inside the nacelle such as the gearbox should be explored. The addition of tuned mass dampers and concepts ideas about how to shift the natural periods outside the Mathieu instability region could be investigated in future work.

Bibliography

Arapogianni, A. (2011). Economics of wind energy. *European Wind Energy Association.*

Budal, K. and Falnes, J. (1975). A resonant point absorber of ocean-wave power. *Nature, 256 (5517), 478-479.*

Butterfield, S., Musial, W., Jonkman, J., and Sclavounos, P. (2007). Engineering challenges for floating offshore wind turbines. *National Renewable Energy Laboratory.*

Castro-Santos, L., Martins, E., and Soares, C. G. (2016). Cost assessment methodology for combined wind and wave floating offshore renewable energy systems. *Renewable Energy, Volume 97, pages 866-880.*

Chakrabarti, S. K. (2005). Handbook of offshore engineering (2-volume set). *Elsevier Science.*

Cruz, J. (2008). Ocean wave energy: Current status and future perspectives. *Springer Series in Green Energy and Technology.*

DNV (2010). Environmental conditions and environmental loads. *DNV-RP-C205.*

Europe, O. E. (2013). Ocean energy: Cost of energy and cost reduction opportunities. *SI Ocean.*

Europe, O. E. (2014). Wave and tidal energy market deployment strategy for europe. *SI Ocean.*

EWEA (2013). Deep water: The next step for offshore wind energy. *European Wind Energy Association.*

EWEA (2015). The european offshore wind industry - key trends and statistics 2015. *European Wind Energy Association.*

EWEA (2016). Wind in power - 2015 european statistics. *European Wind Energy Association.*

Falcao, A. F. d. O. (2010). Wave energy utilization: A review of the technologies. *Renewable and Sustainable Energy Reviews, Volume 14.*

Falkovich, G. (2011). Fluid mechanics: A short course for physicists. *Cambridge University Press.*

Faltinsen, O. (1990). Sea loads on ships and offshore structures. *Cambridge University Press.*

France, W., Levadou, M., Treakle, T., Paulling, J. R., Michel, K., and Moore, C. (2003). An investigation of head-sea parametric rolling and its influence on container lashing systems. *Marine Technology, Vol. 40.*

Haslum, H. and Faltinsen, O. (1999). Alternative shape of spar platforms for use in hostile areas. *Proceedings of the 31st Offshore Technology Conference, Houston, OTC 10953.*

IRENA (2014). Wave energy - technology brief. *International Renewable Energy Agency.*

ISSC (2015). Offshore renewable energy. *The 19th International Ship and Offshore Structures Congress (ISSC) Report.*

Jonkman, J., Butterfield, S., Musial, W., and Scott, G. (2009). Definition of a 5-mw reference wind turbine for offshore system development, technical report/tp-500-38060. *National Renewable Energy Laboratory.*

Koo, B., Kim, M., and Randall, R. (2004). Mathieu instability of a spar platform with mooring and risers. *Ocean Engineering Program, Civil Engineering Department, Texas A&M University.*

LAZARD (2014). Lazard's levelized cost of energy - version 8.0.

Li, L., Gao, Z., and Moan, T. (2013). Joint environmental data at five european offshore sites for design of combined wind and wave energy devices. *Proceedings*

of the 32nd International Conference on Ocean, Offshore and Arctic Engineering, Nantes, France.

Li, Y. and Yu, Y.-H. (2012). A synthesis of numerical methods for modeling wave energy converter-point absorbers. *National Renewable Energy Laboratory.*

Lu, J., Umeda, N., and Ma, K. (2011). Predicting parametric rolling in irregular head seas with added resistance taken into account. *Journal of Marine Science and Technology, Volume 16.*

Maki, A., Umeda, N., Shiotani, S., and Kobayashi, E. (2011). Parametric rolling prediction in irregular seas using combination of deterministic ship dynamics and probabilistic wave theory. *Journal of Marine Science and Technology, Volume 16.*

Mao, H. and Yang, H. (2015). Parametric pitch instability investigation of deep draft semi-submersible platform in irregular waves. *International Journal of Naval Architecture and Ocean Engineering, Volume 8.*

MARINTEK (2014). http://www.sintef.no/home/marintek/laboratories/the-ship-model-tank/.

Marintek (2016). Simulated workbench for marine operations.

Mathworks (2016). Matlab r2016b documentation.

Mouwen, F. (2008). Presentation on wavebob to engineers ireland. *Engineers Ireland.*

Newman, J. (1977). Marine hydrodynamics. *The MIT Press, Massachusetts Institute of Technology, Cambridge, Massachusetts 02142.*

Paulling, J. and R.M., R. (1959). On unstable ship motions resulting from nonlinear coupling. *Journal of Ship Research, Vol. 3.*

Ran, Z., Kim, M., Niedzwecki, J., and Johnson, R. (1995). Response of a spar platform in random waves and currents (experiment vs. theory). *International Journal of Offshore and Polar Engineering.*

Rho, J., Choi, H., Lee, W., Shin, H., and Park, I. (2002). Heave and pitch motion of a spar platform with damping plate. *Proceedings of the 12th International Offshore and Polar Engineering Conference, Kitakyshu, vol. 1, pp. 198201.*

Rho, J. B., Choi, H. S., Shin, H. S., and Park, I. K. (2005). A study on mathieu-type instability of conventional spar platform in regular waves. *International Journal of Offshore and Polar Engineering (ISSN 1053-5381)*.

Shin, Y., Belenky, V., Paulling, J., Weems, K., and Lin, W. (2004). Criteria for parametric roll of large containerships in longitudinal seas. *SNAME Annual Meeting, Washington, D.C.*

UN (1999). The world at six billion. *United Nations*.

Wan, L. (2016). Experimental and numerical study of a combined offshore wind and wave energy converter concept. *Doctoral theses at NTNU 2016:205*.

Wan, L., Gao, Z., and Moan, T. (2014). Model test of the stc concept in survival mode. *Proceedings of the ASME 33rd International Conference on Ocean, Offshore and Arctic Engineering, OMAE2014-23213*.

Wan, L., Gao, Z., and Moan, T. (2015). Experimental and numerical study of hydrodynamic responses of a combined offshore wind and wave energy converter concept in survival modes. *Coastal Engineering, 104, 151-169*.

www.eia.gov (2016). Annual energy outlook 2016. *U.S. Energy Information Administration*.

Yang, H. and Xu, P. (2015). Effect of hull geometry on parametric resonances of spar in irregular waves. *Ocean Engineering, Volume 99*.

Zhang, L., Zou, J., and Huang, E. (2002). Mathieu instability evaluation for ddcv/spar and tlp tendon design. *Proceedings of the 11th Offshore Symposium, Society of Naval Architect and Marine Engineer (SNAME), Houston*.